

LOW-COST AND HIGH-THROUGHPUT OPTOFLUIDIC ADD-ON DEVICE  
FOR LIGHT SHEET IMAGING OF LARVAL AND ADULT *C. ELEGANS*

FARAZ RAHIMPOURESFAHANI

A THESIS SUBMITTED TO THE FACULTY OF GRADUATE STUDIES IN  
PARTIAL FULFILLMENT OF THE REQUIREMENTS FOR THE DEGREE OF  
MASTER OF SCIENCE

GRADUATE PROGRAM IN MECHANICAL ENGINEERING  
YORK UNIVERSITY  
TORONTO, ONTARIO

December 2023

© Faraz Rahimpouresfahani, 2023

## Abstract

Model organisms play a crucial role in scientific research by serving as representative systems that allow researchers to investigate fundamental biological processes and complex diseases. In this study, these organisms, such as *C. elegans*, provide a simplified and controlled environment for experiments, enabling scientists to study biological phenomena with greater precision. The information derived from model organisms often has broad implications for understanding more complex organisms, including humans. Additionally, model organisms offer advantages in terms of genetic tractability, short generation times, and cost-effectiveness, making them valuable tools for high-throughput studies and large-scale experiments. The insights gained from studying model organisms contribute significantly to advancements in various fields, from genetics and developmental biology to drug discovery and disease modelling, ultimately enhancing our understanding of fundamental biological principles and informing potential therapeutic interventions.

Typically, model organisms are subjected to high-content imaging through techniques like confocal and light sheet imaging. However, the utilization of commercial high-content microscopy can prove prohibitively expensive for numerous laboratories, restricting widespread access to high-resolution images of model organisms across various research facilities. Even laboratories equipped with such microscopes often find themselves constrained by the necessity to employ traditional manual sample mounting procedures. This not only consumes valuable time but also imposes limitations on sample size and throughput. The expansion of these aspects could substantially enhance statistical analyses following experiments, underscoring the potential benefits of streamlining and optimizing sample preparation protocols.

There have been a few attempts in order to develop low-cost and accessible high-content imaging platforms. Recent advancements at the interface of microfluidics technology and light sheet fluorescence microscopy have opened the door for high-throughput and high-content investigation of *C. elegans* disease models. This thesis addresses research gaps in the realm of *C. elegans* light sheet imaging platforms, with a particular focus on optimizing a low-cost add-on device with a high throughput. While our initial low-cost work successfully imaged entire worms, it encountered limitations in continuous imaging, adaptability to various developmental stages, and consistency

for quantitative fluorescent expression studies. The primary objective of this thesis is to enhance the previously reported platform, achieving continuous and consistent imaging. Several validation studies are conducted to showcase the optimized platform's performance.

The results section provides a comprehensive account of the characterization and modification process, successfully enabling continuous imaging of the young adult (YA) population of worms. Notably, the platform's application is expanded to encompass earlier developmental stages, specifically the L3 stage, accompanied by comprehensive qualitative and quantitative studies on both stages. The optimized platform proves highly effective in conducting in-depth investigations on protein aggregation and neurodegeneration studies in *C. elegans*, in addition to demonstrating its high throughput and resolution capabilities during initial panneural strain imaging. This highlights the platform's versatility and cost-effective utility in advancing neurobiological research.

Furthermore, having established the continuous platform's functionality in quantitative worm population studies, we employ it to investigate a novel transgenic Parkinson's Disease (PD) model with alpha-synuclein ( $\alpha$ -Syn) accumulation readout. The platform facilitates high throughput quantitative analysis of the Dopaminergic (DA) neurons in a worm population. By integrating a fully automated analysis workflow and recognizing the specific needs of scientists in the drug discovery industry for preclinical testing, our platform has the potential to serve as an efficient and low-cost testing device in the drug testing pipeline.

In order to demonstrate the efficacy of our low-cost high throughput light sheet platform's sensitivity in detecting fluorescence disparities between populations of worms subjected to toxins, we utilized the platform to observe the nerve ring region of both control and exposed groups at larval and young adult stages. This observation was conducted on worms treated with 6-OHDA and Manganese Chloride, and the outcomes have been documented and reported.

In our upcoming research, a close collaboration with a molecular docking specialist is vital for advancing the study of neuroprotective drugs in Parkinson's disease model worms through the development of a specialized high-throughput screening assay. This collaborative effort,

integrating molecular docking expertise, holds the potential to discover new treatment possibilities and contribute to therapeutic interventions for Parkinson's disease.

## **Acknowledgments**

I would like to express my sincere gratitude and appreciation to Professor Tabatabaei and Professor Rezai for their support and guidance throughout my research. I thank the Eurac research for the *C. elegans* strain. The author would also appreciate Mehran Behrouzi, Dr. Youssef and Daphne-Eleni Archonta's help.

# Table of Content

<b>Abstract.....</b>	<b>ii</b>
<b>Acknowledgments .....</b>	<b>v</b>
<b>Table of Content.....</b>	<b>vi</b>
<b>Abbreviations .....</b>	<b>viii</b>
<b>List of Tables .....</b>	<b>ix</b>
<b>List of Equations .....</b>	<b>x</b>
<b>List of Figures.....</b>	<b>xi</b>
<b>1 Chapter One: Introduction .....</b>	<b>1</b>
1.1 <i>Research Motivation and Overview</i> .....	1
1.2 <i>Thesis Organization</i> .....	3
<b>2 Chapter Two: Literature Review .....</b>	<b>5</b>
2.1 <i>C. elegans as a Model Organism</i> .....	5
2.2 <i>Example of C. elegans used for PD Studies</i> .....	8
2.3 <i>C. elegans Assays</i> .....	9
2.3.1 <i>Liquid Media Methods</i> .....	10
2.3.2 <i>Solid Media Methods</i> .....	10
2.3.3 <i>Microfluidic Methods</i> .....	11
2.4 <i>Fluorescence Imaging of C. elegans</i> .....	18
2.5 <i>Light Sheet Microscopy</i> .....	22
2.5.1 <i>Fundamentals of Light Sheet Imaging</i> .....	23
2.5.2 <i>Light Sheet Generation</i> .....	24
2.5.3 <i>Sample Manipulation</i> .....	27
2.5.4 <i>Shadowing Artifacts</i> .....	27
2.5.5 <i>Light Sheet Microscopy Applications</i> .....	28
2.5.6 <i>Advantages and Limitations of Light Sheet Microscopy</i> .....	30

2.5.7	<i>C. elegans</i> Light Sheet Microscopy .....	30
2.5.8	High throughput Light Sheet Imaging of <i>C. elegans</i> .....	35
2.5.9	Compact Light Sheet Microscopy .....	39
2.6	<i>Research Gaps</i> .....	40
2.7	<i>Thesis Objectives</i> .....	42
<b>3</b>	<b>Chapter Three: Methodologies.....</b>	<b>43</b>
3.1	<i>Experimental Setup</i> .....	43
3.1.1	Optofluidic Add-on Device.....	45
3.2	<i>Worm Preparation</i> .....	48
3.3	<i>Imaging Procedure</i> .....	49
3.4	<i>Chemical Exposure</i> .....	51
3.5	<i>Post-Processing</i> .....	51
3.6	<i>Statistical Analysis</i> .....	52
<b>4</b>	<b>Chapter Four: Results and Discussion.....</b>	<b>54</b>
4.1	<i>External Components Modification</i> .....	54
4.1.1	Internal Design Iterations.....	60
4.1.2	Experimental Conditions .....	62
4.2	<i>Continuous pan-neural light sheet imaging of C. elegans at different developmental stages</i> .....	64
4.2.1	Protein Aggregation Analysis of Larval and Young Adult PD Model Transgenic <i>C. elegans</i> .....	68
4.2.2	Throughput of the optofluidic light sheet add-on device .....	71
4.2.3	High-Throughput Light Sheet Imaging Application in Chemical Screening .....	74
4.2.3.1	6-OHDA Induced Toxicity.....	74
4.2.3.2	Manganese Induced Toxicity .....	76
<b>5</b>	<b>Chapter Five: Thesis Summary and Future Work.....</b>	<b>82</b>
5.1	<i>Thesis Summary</i> .....	82
5.2	<i>Limitations and Recommendations for Future Work</i> .....	83
<b>6</b>	<b>Bibliography .....</b>	<b>85</b>

## **Abbreviations**

6-hydroxydopamine (6-OHDA)

Alpha Synuclein ( $\alpha$ -Syn)

Alzheimer's Disease (AD)

*Caenorhabditis elegans* (*C. elegans*)

Confocal Microscopy (CM)

*Danio rerio* (*D. rerio*)

Dopaminergic (DA)

*Drosophila melanogaster* (*D. melanogaster*)

Green Fluorescence Protein (GFP)

Huntington's Disease (HD)

Light-Sheet Fluorescence Microscopy (LSFM)

Manganese (Mn)

Manganese Chloride ( $MnCl_2$ )

Mean Fluorescence Intensity (MFI)

Mean Intensity of the Nerve Ring (MINR)

Numerical Aperture (NA)

Parkinson's Disease (PD)

Polydimethylsiloxane (PDMS)

Selective Plane Illumination Microscopy (SPIM)

Wide-Field (WF)

Yellow Fluorescent Protein (YFP)

Young Adult (YA)

## List of Tables

Table 4-1 Frame rate, functional (obtained) throughput and hypothetical maximum throughput of the proposed optofluidic device for YA and L3 <i>C. elegans</i> light sheet imaging.....	72
Table 4-2. Overview of Imaging Studies Utilizing <i>C. elegans</i> Light Sheet Microscopy This table provides an overview of imaging studies that employed <i>C. elegans</i> light sheet microscopy, including details on the imaging objectives, worm strain and age, resolution, and performance.	73

## List of Equations

Equation 2-1	$2w_0 = 2\lambda NA_{illumination}$ .....	25
Equation 2-2	$Z_r = \pi w_0^2 \lambda$ .....	25
Equation 2-3	$R_{lateral} = \lambda_{emission} 2NA_{detection}$ .....	26

## List of Figures

- Figure 2-1 Drug discovery process schematic illustrating various stages of finding therapeutics, including preclinical studies with *C. elegans* as a middle ground between the cellular and animal assays. There are other steps before and after preclinical studies, such as research and development, clinical trials, and approval procedures. (Adapted from “The Drug Discovery Process” by BioRender.com (2023). Retrieved from <https://app.biorender.com/biorender-templates>)..... 6
- Figure 2-2 The life cycle of *C. elegans* at a temperature of 22°C is depicted, with the time of fertilization represented by 0 min. The duration of each developmental stage is indicated by blue numbers along the arrows, with the first cleavage typically occurring approximately 40 min post-fertilization. Eggs are laid outside the body at around 150 min post-fertilization during the gastrula stage. The animal’s length at each stage is denoted in micrometres (µm) next to the corresponding stage name [16]. ..... 7
- Figure 2-3 Images of PD model *C. elegans* heads. A) 6-day-old A53T PD model *C. elegans* expression. Creative Commons CC-BY license. B) 6-day adult showing intense and merged YFP-labelled granules in the head region. Permission acquired from CNS & neurological disorders drug targets. C) Representative fluorescent image of the head of 3-day-old ERS100. The dotted square line in Panel C highlights the area used for quantifying phenotype A, which refers to aSyn: Venus inclusions. Additionally, the solid square line emphasizes the region used for quantifying phenotype B, relating to cephalic (CEP) dendrite blebbing. Creative Commons CC-BY license. 9
- Figure 2-4 Assays can be conducted using either solid or liquid media, with the former being the predominant method employing agar-based media. The latter, which employs S-media, is commonly utilized for evaluating the impact of chemicals on various factors [38]. This image is used under a Creative Commons Attribution 4.0 International (CCBY) License. .... 11
- Figure 2-5 The phenotypic analysis and behaviour of microfluidics studies schematics and designs A) An array of 16 chambers was designed, with branching distribution channels delivering *E. coli* suspension from the inlet to the outlet. B) A single circular chamber with an adjoining clamp was designed, specifying dimensions. Images used with permission from the Royal Society of Chemistry. C) The microfluidic structure used in CD cultivation consists of a nutrient reservoir (1), a cultivation chamber (2), and a waste reservoir (3). Image is used with permission from

Elsevier. D) The behaviour chip is depicted at the top, while the image at the bottom showcases the trapping of individual worms. An inset displays a fluorescence image of an AVA interneuron expressing G-CaMP. The image is used with permission from Springer Nature. E) The image shows the device filled with dye, revealing a pattern of 48 circular chambers interconnected by a serpentine channel. Black arrows indicate flow direction. F) Components of each chamber are labelled as follows: a (serpentine channel), b (single worm loading channel), c (stopper), d (circular chamber), e (diverging channels), and f (chamber outlet). White arrows indicate flow direction. Images used with permission from the Royal Society of Chemistry..... 14

Figure 2-6 Schematic and actual platforms for *C. elegans* manipulation A) The diagram illustrates the worm sorting device illustrating various layers. B) (Top) Replacement of epi-illumination with a generated light-sheet in the host microscope. (Bottom) The working principle of the optofluidic device involves focusing a collimated input beam using the integrated PDMS lens, resulting in the generation of a light-sheet inside the microfluidic channel. Copyright 2021 Society of Photo-Optical Instrumentation Engineers (SPIE). C) The photograph shows the gasket system that holds a 96-well vivoChip in place. This image is used with permission from Mary Ann Liebert, Inc.. 18

Figure 2-7 Schematic figure of epi-WF and confocal laser scanning microscopy A) Epi-WF microscopy setup, illustrating the excitation light path (blue arrow) and emitted fluorescence detection (green arrow). The excitation light illuminates the entire field of view, while the emitted fluorescence is captured by the objective lens and directed to the detector. B) The setup of confocal laser scanning microscopy showcases the laser excitation beam (blue arrow) focused on a single point within the specimen. The emitted fluorescence (green arrow) is selectively collected by a pinhole before reaching the detector, enabling optical sectioning and improved resolution compared to WF microscopy. (Made by BioRender.com)..... 20

Figure 2-8 Representative fluorescence images of  $\alpha$ -syn accumulation in the head region are depicted to demonstrate the YFP expression pattern in the muscles of OW13 worms subjected to rpn-1 RNA interference treatment [47]. Images are used under a Creative Commons Attribution 4.0 International (CCBY) License. .... 21

Figure 2-9 The expression of  $\alpha$ -synuclein-YFP in the head region of aging transgenic *C. elegans* is illustrated using confocal laser scanning images [30]. This image is used under a Creative Commons Attribution License. Copyright © 2008 [van Ham *et al.*]. .... 22

Figure 2-10 The fundamental configuration of a light-sheet microscope (LSFM) involves the independent arrangement of the illumination or excitation path and the detection or emission path. Within this setup, a thin sheet of light is generated to specifically illuminate and excite the region of interest within the sample, aligning precisely with the focal plane of the detection objective [55].  
..... 23

Figure 2-11 The diagram illustrates the optical arrangement of the illumination unit. A) In its simplest form, a single cylindrical lens is employed to focus a collimated beam onto the sample, creating a light sheet. The thickness of the light sheet is adjustable using a slit, which also allows for control of the numerical aperture (NA) of the illumination lens. B) To achieve a diffraction-limited light sheet in selective plane illumination microscopy (SPIM), an improved setup is employed. This configuration, illustrated with optical components and ray traces in planes perpendicular to the light sheet, includes an adjustable gimbal-mounted mirror that enables precise alignment of the light sheet with the detection unit's focal plane (not depicted). A relay telescope formed by lenses L1 and L2 facilitates the generation of the light sheet by combining a cylindrical lens with an objective (obj). The diagram also indicates the position of the back focal plane (BFP) [56]. This image is used under a Creative Commons CC BY License..... 24

Figure 2-12 Gaussian beam characteristics A) Schematic of SPIM illumination and detection arm with axial ( $2w_0$ ) and lateral resolution ( $Z_r$ ) displayed. [54] B) A thin light sheet provides uniform illumination, but this is limited to a small field of view. On the other hand, a wider field of view can only be achieved by using a thicker light sheet. This trade-off between light sheet thickness and field of view is illustrated, highlighting the relationship between the two aspects[57]. Image used with permission from Elsevier..... 26

Figure 2-13 Available approaches for scientists to use light sheet microscopy. A) Developing the light sheet from scratch. diSPIM offers manuals and the components to be purchased for scientists to build their own light sheet microscope. Or they can build their own customized platforms. CC Attribution-Share Alike 4.0 International B) Collaborating with the existing light sheet facilities to use their platforms. (Created with BioRender.com using an image from Kennedy Institute of Rheumatology © 2023 University of Oxford) C) The most convenient yet expensive approach is to purchase a commercialized product from well know microscope manufacturers such as Bruker

(MuVi-SPIM) © Copyright Bruker 2023, LaVision (Ultramicroscope 2) Copyright © 2023 Miltenyi Biotec and/or its affiliates, and 3i (Lattice) ©2023 Intelligent Imaging Innovations.... 29

Figure 2-14 iSPIM setup schematic and neural imaging of larvae development A) A Z translation stage is directly bolted onto the illumination pillar of an inverted microscope, onto which two water-immersion objectives are mounted. B) Several maximum-intensity projections have been chosen from a typical embryo to emphasize various stages of its development[7]. Images are used under a Creative Commons License ..... 31

Figure 2-15 A schematic of the assembled diSPIM system is presented. 0.8 NA water-immersion objectives, labelled as A and B, are positioned at right angles on a z-axis translation stage, securely attached to an inverted microscope's illumination pillar. Along with additional optical components, these objectives generate a thin sheet of light that illuminates the sample. Objective A (or B) is used for excitation, while the fluorescence produced is collected through objective B (or A) positioned perpendicular to it. The collected fluorescence is then directed toward camera B (or A) using dichroic mirrors, emission filters, and lenses. B) Using diSPIM, tagged histones were imaged in a *C. elegans* embryo. A live *C. elegans* embryo is shown with nuclear histones in a selection of maximum-intensity projections from a 14-hour imaging experiment [65]. Images used with permission from Springer Nature..... 32

Figure 2-16 Experimental setup and the representative image acquired A) Schematic of the experimental system B) Using the suggested technique, a 3D visualization of a *C. elegans* embryo at a three-stage development has been captured by SPIM [66]. © 2015 Optica Publishing Group. .... 33

Figure 2-17 Experimental setup schematic and representative volumetric images of *C. elegans* A) presents a three-dimensional illustration of the LSM system and its constituent parts, The path of the laser beam is depicted in red, which is directed via a flexible mirror and focused onto the sample using a cylindrical lens that generates a laser light sheet. The sample is immersed in an index-matching fluid bath and positioned in 3D space through an x, y, z-axis movable stage, allowing imaging with a CCD camera and tube lens attachment that is orthogonal to the light sheet (B) Basic two-dimensional scheme of the system's fundamental components. C) Representative images of an organism expressing muscle-specific GFP collected at various angles (0°, 20°, and 45°). (pmyo-3GFP). The photos show that there are muscular structures in the ventral-left (VL), ventral-right (VR), and dorsal-left (DL) areas. The scale bars that are shown in the images are 100

$\mu\text{m}$  [6]. Images are used under a Creative Commons Attribution 4.0 International (CCBY) License. .... 34

Figure 2-18 Schematic of the experimental setup and representative of collected images A) The diagram depicting the light-sheet microscope is exhibited. B) A cross-sectional view is provided to showcase the worms that express TBB-4::EGFP and PH::GFP. C) A maximum projection of 115 slices, each measuring  $0.75 \mu\text{m}$ , is utilized to demonstrate the head region of *C. elegans* expressing TBB-4::EGFP from anterior to posterior [67]. Images are used under a Creative Commons Attribution 4.0 International (CCBY) License. .... 35

Figure 2-19 The first generation of high throughput experimental setup, along with the intricately acquired volumetric image. A) A diagram is presented depicting an open-top Selective Plane Illumination Microscopy (SPIM) setup, where two objectives are positioned below the sample stage. Additionally, a three-dimensional representation of the microscope is included below the two-dimensional drawing. B) The data displayed represents a z-projection [5]. © 2015 Optica Publishing Group. .... 36

Figure 2-20 Next generation of high throughput light sheet platforms experimental setup schematics. A) A diagram illustrates the flow imaging system utilized in the study. The system employs light-sheet illumination, orthogonal detection, and a microfluidic imaging platform. A magnified image is provided as an inset, showcasing the light sheet entering the microfluidic channel. B) A schematic diagram portrays the intersection of the light sheet with the channel. The 2D cross-sectional images in raw and ML reconstructed form are presented in two rows. The PSF employed for the ML reconstruction is displayed in the upper left corner of the image. [12] Images were used with permission from AIP Publishing. .... 37

Figure 2-21 Overview of a high-speed fluorescence microscopy system, called Line Excitation Array Detection (LEAD), used as a 3D whole-animal flow cytometer. A) The system includes a schematic of the imaging system, which employs a longitudinal TeO<sub>2</sub> acousto-optic deflector (AOD) with a chirped frequency to scan a laser excitation beam across an angled plane on the sample. The excited plane is then imaged onto a photomultiplier tube (PMT) array, which captures a full frame of each scan cycle. In addition, a microfluidic device is employed to deliver populations of hundreds of *C. elegans*. Two light sheets generated by a HeNe laser and two photodiodes (PDs) are used to detect the velocity of the animals as they move through the imaging

region. B) The volumetric image is composed of 631 x-y frames, each 66 x 14 pixels in size and captured every 1.25 microseconds. The image includes a scale bar of 50 micrometres [70]. Images are used under a Creative Commons Attribution 4.0 International (CCBY) License. .... 38

Figure 2-22 Low-cost and compact LFSM platforms A) VHLSFM (Volumetric High-Speed Light-Sheet Fluorescence Microscopy) system, with various components and add-ons that enable high-speed imaging and volumetric data acquisition. A schematic is presented, depicting the VHLSFM system. The VHG (Volume Holographic Grating) setup consists of an objective lens (MO1), relay lens (L), and cylindrical lens (CL). B) Images of oocytes inside *C. elegans* are shown, acquired using the VHLSFM (right) and a WF microscope (left) [10]. © 2020 Optica Publishing Group. C) Schematic of an add-on device, which is composed of multiple compact mechanical components and optical elements. D) Volumetric images of muscular activities of behaving *C. elegans* larva [9]. Images were used with permission from John Wiley and Sons. F) The experimental configuration comprised a low-cost laser diode and an iris, both situated in a free-space setup, which together generated the input excitation beam for the optofluidic device. The optofluidic add-on device, located on top of the inverted WF fluorescent microscope, is depicted in the inset of (a) [13]. This image is used under a Creative Commons CC BY License..... 40

Figure 3-1 ..... 44

Figure 3-1 Experimental setup. A) The front view of the experimental setup contains the image acquisition add-on, flow delivery package and the optofluidic chip. B) Side view of the experimental setup, including a free-space and low-cost laser source and an iris that was used to generate the input excitation beam of the optofluidic device. The optofluidic add-on device is placed on the inverted WD fluorescent microscope. The generated light sheet replaced the epillumination of the host microscope. The emitted fluorescent was collected by the native objective lens of the microscope and recorded using an sCMOS camera..... 45

Figure 3-2 Schematics of the mechanical and optical design of the optofluidic chip. A) Schematic of excitation (blue) and emission (green) beams with respect to host microscope objective lens, high frame rate camera and the optofluidic chip. The front view of the actual light sheet at the bend in the darkfield is displayed within the inset of Figure (A). (Created with BioRender.com) B) Schematic of the front view of the chip’s design displaying the inlet and outlet with respect to the PDMS-integrated micro lens. C) Zoom view of the bend illustrating dimensions of microchannels

for L3 and YA stages and radius of the micro lens in addition to the light sheet thickness and beam diameter..... 46

Figure 3-3 Fabrication process of optofluidic devices. (1) Design pattern transferred to PDMS layer by curing on silicon mould and peeling off. (2) A patterned PDMS layer is bonded to a flat PDMS layer via oxygen plasma treatment to seal microfluidic channels. (3) The device was cut close to the light-sheet plane to collect emission fluorescence from the side facet. (4) Additional step to create an optically flat facet: PDMS spin-coated on a glass slide, a device placed on top, and peeled off once cured (5-7) [73]..... 47

Figure 3-4 Flow chart illustrating the post-processing steps. A) Region of Interest (ROI) cropping, restricting the analysis to a 100×100 square area containing neural fluorescence expressions. B) Background subtraction performed using the built-in rolling ball algorithm in ImageJ. C) Extraction of fluorescence-bearing frames from the large dataset by applying MATLAB thresholding techniques. D) Dimensionality reduction of each frame from 2D to 1D using the Mean Fluorescence Intensity (MFI) approach. E) Conversion of the separated frames into signal format utilizing the MFIs. F) Utilization of MATLAB's signal processing toolbox to analyze fluorescence expressions, identify peak locations and determine peak values..... 52

Figure 4-1 Schematic representation of challenges encountered during the process of loading worms into the imaging device. The current method of introducing worms through disconnected tubing leads to issues such as worm dripping and loss, contamination risk, and air bubble formation, potentially affecting imaging quality and data analysis. The Inset image displays the actual glass fixture... 55

Figure 4-2 Schematic and real 3D printed fixture for alignment optimization A) Solidworks model displaying the inverted fluorescence microscope in the laboratory, featuring the attachment of two fixtures on the side and top of the microscope. B) A more detailed set of fixtures illuminates the optomechanical components and the laser on the side fixture, while the top fixture aids in precise alignment of the sample concerning the laser and the detection objective. C) Real image showcasing the implementation of the fixtures on the inverted microscope. The mounting of fixtures on the original transition stage facilitates smooth sample movement along the X and Y axes during the alignment process. .... 56

Figure 4-3 Images of the mounted platform before and after external and internal modifications. A) The previous chip configuration features the platinum-cured silicone tubing, securely mounted on the

3D printed fixture. B) The previous chip, positioned on the older glass fixture, is intended for attachment to the microscope stage using tape. C) The previous chip showcasing the Tygon tubing, mounted on the 3D printed fixture, providing the capability to load worms from the upper hand. D) The internally modified chip, significantly reduced in size, is equipped with the Tygon tubing inlet and outlet, enhancing overall compactness and functionality. .... 58

Figure 4-4 Approaches to address the challenges faced during the laser alignment and loading of worms into the imaging device. A) Schematic of the designed fixture to hold the optofluidic device on top of the host objective with respect to the laser beam. B) The actual fixture is mounted on the inverted microscope. C) Worm loading T-junction setup. D) The centrifugal tube with a hole at the bottom was introduced as the worm reservoir that prevents the sinking of worms but lacked control over the flow of specimens, leading to the exploration of alternative solutions such as pressure pumps. .... 60

Figure 4-5 Internal design iterations A) The initial design showcases the incorporation of an inverse tapered area within the channel to accommodate the NA of the detection lens. B) Adjusted bend angle in the microchannel design, effectively guiding the worms in the desired direction while maintaining resolution. C) An additional microchannel above the light sheet was introduced, designed to alleviate back pressure by collecting and reducing the buildup of pressure above the bend within the main channel. D) Successful integration of a newly acquired pressure pump into the design, enabling the functioning of the adjusted bend design in the microchannel..... 61

Figure 4-6 Number of frames acquired from each worm at different flow rates of 3, 5, and 9  $\mu\text{l}/\text{min}$  for  $n=10$  worms for each flow rate. Cross-sectional light sheet images of the NW1229 nerve ring at each flow rate are represented above the corresponding chart. .... 63

Figure 4-7 Qualitative analysis of the fluorescent expression of NW1229 worms at two developmental stages. A) Montage of cross-sectional images of fluorescence expression of the nerve ring of worms at YA (Left) for  $n=112$  worms and L3 (Right) stages for  $n=101$  worms. B) Representative cross-sectional images of fluorescence expression of nerve rings in L3 worms in O and U shapes indicated by white arrows. C) Comprehensive stack of images with  $\sim 1000$  acquired frames of NW1229 strain with representative slices showing the nervous system in detail. .... 65

Figure 4-8 Shaded error bar graphs of normalized fluorescence expression in nerve ring (Peak) for YA and L3 NW1229 A) Shaded error bar graph representing the normalized fluorescence expression

of YA NW1229 from head to tail. The analysis is based on a sample size of  $n=10$ , with error bars indicating the variability in fluorescence levels. Inset Image: A representative inset image of the nerve ring (peak) showcasing the fluorescence expression pattern for YA NW1229. B) Shaded error bar graph illustrating the normalized fluorescence expression of L3 NW1229 along the head-to-tail axis. The data is derived from  $n=10$  replicates, and the error bars indicate the degree of variation. Inset Image: A representative inset image of the nerve ring (peak) displaying the fluorescence expression pattern for L3 NW1229. Scale bars in both images are 15 microns..... 66

Figure 4-9 Quantitative analysis of the mean fluorescence intensity in the pan neuronal NW1229 nerve rings. A) Histograms illustrate the increase in both the spatial extent and intensity of expression due to aging. The number of pixels, serving as a representative measure of the area, consistently demonstrates an upward trend. Simultaneously, the maximum intensity value exhibits a corresponding rise, reflecting the heightened magnitude of expression. The Inset view displays the zoom view of the first 30 pixel intensity values. B) Violin plots depicting the distribution of data for L3 (left) and YA (middle) groups. The dashed lines at the top and bottom of each violin represent the first and last quarters of the data, respectively, while the middle line denotes the median. The dashed lines that cross the right y-axis correspond to the mean value for each group. The mean value of L3 is set as the origin (0), and the difference in means between L3 and YA is illustrated by a 95% confidence interval (CI) bar extending to the mean of YA. .... 67

Figure 4-10 Quantitative analysis of the mean fluorescence intensity in the pan neuronal NW1229 nerve rings. A) Histograms illustrate the increase in both the spatial extent and intensity of expression due to aging. The number of pixels, serving as a representative measure of the area, consistently demonstrates an upward trend. Simultaneously, the maximum intensity value exhibits a corresponding rise, reflecting the heightened magnitude of expression. The Inset view displays the zoom view of the first 25 pixel intensity values. B) Violin plots depicting the distribution of data for L3 (left) and YA (middle) groups. The dashed lines at the top and bottom of each violin represent the first and last quarters of the data, respectively, while the middle line denotes the median. The dashed lines that cross the right y-axis correspond to the mean value for each group. The mean value of L3 is set as the origin (0), and the difference in means between L3 and YA is illustrated by a 95% confidence interval (CI) bar extending to the mean of YA. .... 68

Figure 4-11 Shaded error bar graphs of normalized fluorescence expression in nerve ring (Peak) for YA and L3 ERS100 A) Shaded error bar graph representing the normalized fluorescence expression of YA ERS100 from head to tail. The examination relies on a sample size comprising of n=10, with error bars indicating the variability in fluorescence levels. Inset Image: A representative inset image of the nerve ring (peak) showcasing the fluorescence expression pattern for YA ERS100. B) Shaded error bar graph illustrating the normalized fluorescence expression of L3 ERS100 along the head-to-tail axis. The data is derived from n=10 replicates, and the error bars represent the extent of variability. Inset Image: A representative inset image of the nerve ring (peak) displaying the fluorescence expression pattern for L3 ERS100. Scale bars in both images are 15 microns. 70

Figure 4-12 Quantitative analysis of the mean fluorescence intensity in the PD model ERS100 nerve rings. A) Histograms illustrate the increase in both the spatial extent and intensity of expression due to aging. The number of pixels, serving as a representative measure of the area, consistently demonstrates an upward trend. Simultaneously, the maximum intensity value exhibits a corresponding rise, reflecting the heightened magnitude of expression. The Inset view displays the zoom view of the first 50 pixel's intensity value. B) Violin plots depicting the distribution of data for L3 (left) and YA (middle) groups. The dashed lines at the top and bottom of each violin represent the first and last quarters of the data, respectively, while the middle line denotes the median. The dashed lines that cross the right y-axis correspond to the mean value for each group. The mean value of L3 is set as the origin (0), and the difference in means between L3 and YA is illustrated by a 95% confidence interval (CI) bar extending to the mean of YA. .... 70

Figure 4-13 Cross-sectional images illustrating the fluorescence appearance within the nerve ring of the worms. The upper section (YA) depicts A) fluorescence expression in control worms (n=63) and B) fluorescence expression in exposed worms (n=85). The lower section (L3) illustrates C) fluorescence expression in control worms (n=72) and fluorescence expression in exposed worms (n=95). All scale bars indicate 50  $\mu$ m. .... 75

Figure 4-14 A quantitative assessment was conducted on the normalized mean intensity within the nerve ring of pan neural worms. Scatter dot plots are employed to visually represent the data distribution for the following scenarios: A) control (left) and exposed (middle) groups at the L3 stage, and B) control (left) and exposed (middle) groups at the YA stage. The dashed lines intersecting the right y-axis correspond to the respective mean values for each group. Notably, the mean value of the

control group serves as the reference point (origin, 0), while the distinction in means between the control and exposed groups is graphically depicted by a 95% confidence interval (CI) bar..... 76

Figure 4-15 Qualitative analysis of L3 (Top of the panel) and YA (Bottom of the panel) for control and exposed worms to 5 and 10 mM *MnCl2*. A) Fluorescence expression in L3 control worms (n=271) B) fluorescence expression in 5 mM exposed worms (n=257) and C) fluorescence expression in 10 mM exposed worms (n=115) D) Fluorescence expression in YA control worms (n=215) B) fluorescence expression in 5 mM exposed worms (n=460) and C) fluorescence expression in 10 mM exposed worms (n=219)..... 77

Figure 4-16 Quantitative analysis of L1 and YA control and exposed worms to 5 and 10 mM *MnCl2*. A) Mortality rate of L1 worms for control (n=31) and exposed to 5 mM (n=160) and 10 mM (n=237) groups normalized using max scaling to the control group. B) Mortality rate of YA worms for control (n=21) and exposed to 5 mM (n=41) and 10 mM (n=83) groups normalized using max scaling to the control group. C) Representative image of a healthy *C. elegans*. D) Representative images of exposed worms. E) Representative of a dead nematode. .... 79

Figure 4-17 Quantitative analysis of the normalized mean intensity of the nerve rings for control and exposed groups at L3 and YA. A) Normalized mean intensity of the nerve rings for control (n=271), 5 mM (n=257) and 10 mM (n=115) exposed worms at L3. B) Normalized mean intensity of the nerve rings for control (n=215), 5 mM (n=460) and 10 mM (n=219) exposed worms at YA. .... 80

# 1 Chapter One: Introduction

## 1.1 Research Motivation and Overview

*Caenorhabditis elegans* or *C. elegans* is a miniature, transparent roundworm used extensively as a model organism in scientific research [1]. Its simple body structure, short lifespan, and fully mapped nervous system make it an ideal subject for studying genetics, developmental biology, and neurobiology. The well-characterized genome of *C. elegans* allows researchers to investigate various biological processes, such as cell division, aging, and response to environmental factors [2]. Moreover, the worm's transparency allows for detailed observation of individual cells and tissues, facilitating an understanding of fundamental biological mechanisms. Another key value offered by *C. elegans* is its short lifespan, making *C. elegans* a simple and low-cost disease model between cell and animal assays. Owing to these attributes, *C. elegans* has significantly contributed to our knowledge of biology in the past decades and provided valuable insights into human biology, development, and diseases [3].

A key element for the success of the investigations on *C. elegans*, however, is the ability to image and quantify fluorescent expressions of populations of *C. elegans* at high speed, with high resolution, with minimal photodamage to the animals, and preferably at low cost. Confocal fluorescence microscopy offers unprecedented image resolution but is relatively slow, high-cost, and prone to photo-damaging [4]. Conventional light sheet microscopy, on the other hand, offers high image resolution with minimal photodamage but requires complex and costly instrumentation, which makes it less accessible to researchers. Aside from the expenses and intricacy associated with these platforms, they require mounting and immobilizing samples, leading to a substantial decrease in their overall throughput. The handling and immobilization of *C. elegans* worms pose significant challenges when interrogating large quantities of worms with confocal or light sheet microscopy techniques [5]–[8]. This becomes a critical obstacle for studies that require rapid imaging of *C. elegans* populations to facilitate comprehensive statistical analysis.

To overcome the mounting and immobilization limitations, microfluidic-based solutions have been proposed for the automated and rapid loading of *C. elegans* in light sheet imaging platforms [9]–[11]. These platforms enable faster and more convenient sample loading while simultaneously allowing for continuous imaging of *C. elegans* without interfering with other functions. Another

appealing feature of microfluidic solutions is their ability to regulate the flow of *C. elegans* through the imaging plane of microscopy systems to minimize non-uniform motion artifacts [12]. That is, given the specimen's characteristics (e.g., shape, size, mass, and fluorophore's emission properties) and sensor/camera's specifications (e.g., quantum efficiency, sensitivity, and frame rate), flow speed can be controlled to achieve continuous high-resolution imaging of *C. elegans*. However, the key drawback of any sophisticated platform is its cost, preventing its widespread adoption by end users.

To address the key limitations of integrated microscopy and microfluidic devices (called optofluidic devices), some studies have focused on making the light sheet platforms more affordable and compact. In a recent study of our group, we reported on developing a low-cost light sheet add-on microfluidic device that can be operated with conventional microscopes to solve the technical complexity and cost of conventional light sheet systems while making the imaging system accessible to researchers [13]. While in this preliminary work, we showed the ability to image an entire worm, the system suffered from key limitations such as the inability to continuously image worms' populations, lack of adaptability to image worms at different developmental stages, and lack of imaging consistency to enable quantitative fluorescent expression studies.

This thesis describes optimizing our preliminary technology to overcome its limitations. The optimized system utilizes a microfluidic chip designed for continuous light-sheet imaging of *C. elegans*, a high frame rate sCMOS camera, and a pressure-based flow delivery sub-system. The performance of the optimized system is validated via continuous flow-based imaging of populations of NW1229 (expressing fluorescent pan-neuronally) and ERS100 (expressing Alpha-Synuclein ( $\alpha$ -Syn) accumulation in their DA) *C. elegans* strains at L3 and young adult (YA) developmental stages. Qualitative and quantitative analysis of results demonstrates the effectiveness and versatility of the optimized, low-cost imaging platform in capturing the developmental dynamics and detecting protein expressions of PD model *C. elegans* with high temporal resolution.

After successfully developing a platform capable of rapid imaging and comprehensive sample analysis, we present our platform's potential applications in chemical screening. In this

investigation, we employed the platform to image a population of control and exposed worms to 6-hydroxydopamine (6-OHDA) and Manganese Chloride ( $MnCl_2$ ), in order to observe and analyze neurodegeneration in both larval and young adult (YA) populations.

## 1.2 Thesis Organization

Chapter 1: Motivation – This chapter provides an in-depth exploration of the motivations behind this study, highlighting the significance and relevance of the research topic.

Chapter 2: Literature Review – In this chapter, a comprehensive review of related studies on *C. elegans*, microfluidic assays, light sheet microscopy, and high-throughput imaging is presented. By examining the interconnections between these elements, the research gaps are identified, leading to the formulation of the thesis objectives.

Chapter 3: Instrumentation, Design, and Fabrication – Chapter 3 focuses on the detailed description of the instruments, microfluidic device designs, fabrication methods, and experimental procedures employed in the study. Additionally, information pertaining to the specific transgenic strains of *C. elegans* and their maintenance is provided. This chapter also elucidates the iterations and modifications made to our original optofluidic device, [13] providing a comprehensive understanding of the developmental process.

Chapter 4: Results – Chapter 4 of this report presents a detailed account of the modification process applied to the previous design and components, enabling continuous imaging of the YA population of worms. Notably, the chapter highlights the significant expansion of the platform's application to include earlier stages of development, specifically the L3 stage. Within this context, the chapter provides comprehensive reports on the qualitative and quantitative studies conducted on both developmental stages. Beyond its initial application to image the pan-neural strain and demonstrate the platform's high throughput and resolution capabilities, the optimized platform was successfully employed for comprehensive investigations concerning protein aggregation and neurodegeneration studies in *C. elegans*.

Chapter 5: Conclusion and Future Recommendations – The final chapter summarizes the key findings of the study and presents insightful conclusions. Additionally, based on the research outcomes, recommendations for future investigations and areas of further research are provided.

## 2 Chapter Two: Literature Review

### 2.1 *C. elegans* as a Model Organism

Selecting a model organism that mimics human biology in the best possible way for disease studies and drug discovery is a balancing act of trade-offs. Figure 2-1 depicts the steps involved in the drug discovery process. While humans are undoubtedly the greatest at simulating human disease, there are practical and ethical constraints to starting drug discovery directly with human models. Therefore, a key step of the process is the preclinical studies where lead compounds must be tested on target proteins *in-vitro* (cell cultures) and *in-vivo* (animals) in order to test for toxicity and select the best compound candidates for clinical trials. Cell culture studies are very common at the early stages of preclinical studies, but they do not mimic the complexity of animal models and humans, hence trending to be improved by other complementary biomimetic models like 3D scaffolds and organs-on-chips. At later stages of preclinical studies, mammals, most notably mice, are highly effective for modelling and researching human disease. However, mice have limitations in terms of both disease replication and the capacity to study diseases quickly [14]. Small model organisms (e.g., *D. melanogaster*, *C. elegans*, and *D. rerio*) are of interest to preclinical studies because they serve as lower-cost and less time-consuming middle grounds between cell assays and animal trials.

# The Drug Discovery Process

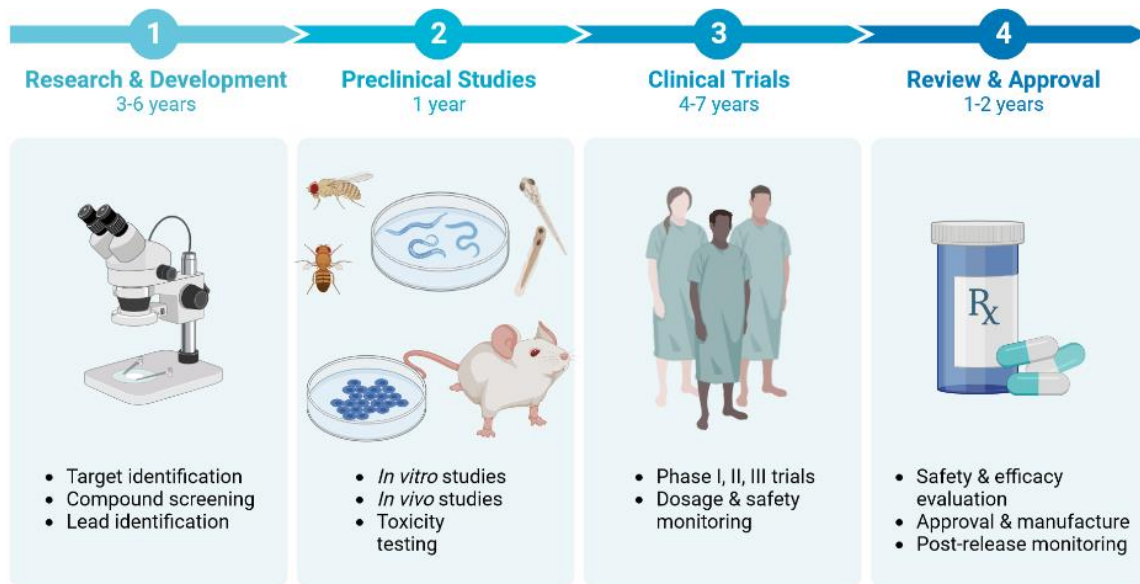


Figure 2-1 Drug discovery process schematic illustrating various stages of finding therapeutics, including preclinical studies with *C. elegans* as a middle ground between the cellular and animal assays. There are other steps before and after preclinical studies, such as research and development, clinical trials, and approval procedures. (Adapted from “The Drug Discovery Process” by BioRender.com (2023). Retrieved from <https://app.biorender.com/biorender-templates>)

*C. elegans* is a great candidate for human disease modelling because the animal’s neural network has been mapped [15], and each neuron can be traced to its origin. Furthermore, the simplicity of culturing, maintaining, and self-fertilizing the worms, plus the fast life cycle, simplifies the researcher’s tasks and enhances efficiency. The life cycle of *C. elegans* at a temperature of 22°C is graphically illustrated in Figure 2-2, depicting a 60-hour period for the development of an adult worm. Each developmental stage’s duration is indicated by numeric values in blue along the arrows, while the length of the organism at each stage is denoted in micrometres ( $\mu\text{m}$ ) adjacent to the corresponding stage name [16]. But one of the most helpful features of these animals is their transparency; its transparent body is conducive to calcium imaging [17], optogenetics [18], and other fluorescence-based techniques, allowing for observation of both single neurons and the entire nervous system.

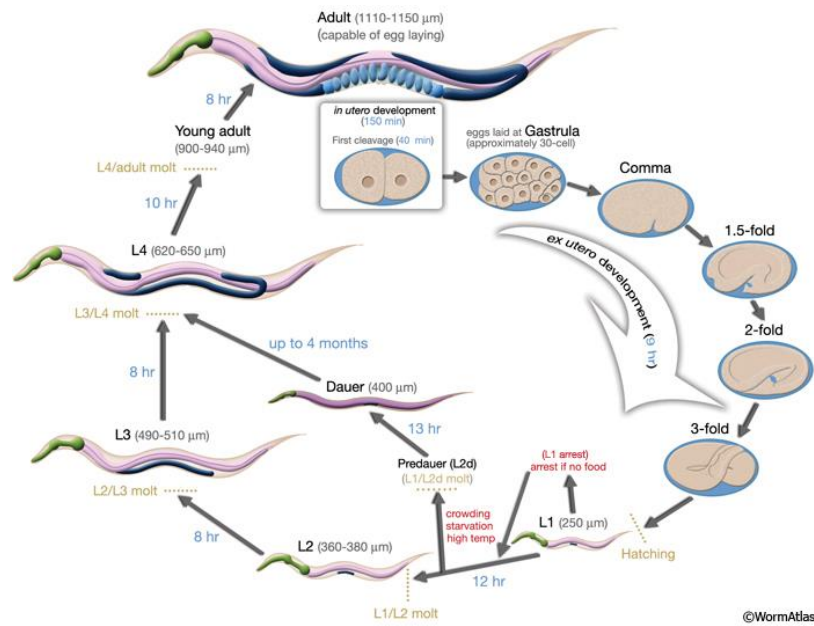


Figure 2-2 The life cycle of *C. elegans* at a temperature of 22°C is depicted, with the time of fertilization represented by 0 min. The duration of each developmental stage is indicated by blue numbers along the arrows, with the first cleavage typically occurring approximately 40 min post-fertilization. Eggs are laid outside the body at around 150 min post-fertilization during the gastrula stage. The animal's length at each stage is denoted in micrometres (μm) next to the corresponding stage name [16].

*C. elegans* has already been used to study a variety of active substances [19]. Nematodes are exposed to bacterial and fungal pathogens in their natural habitat, and many human disease-causing pathogens are known to infect *C. elegans* [20]. As a result, worms can help identify anti-infective drugs in a high-throughput manner. Such screenings allow harmful chemicals to be ruled out early in the medication development process. *C. elegans* is a helpful model for discovering anthelmintic chemicals [21].

Worms are also crucial in studying the molecular causes of ageing and longevity and finding pro-longevity chemicals due to their short lifetime [22], [23]. For example, transgenic worms have been utilized in studies for modelling Alzheimer's disease (AD), Parkinson's disease (PD), and Huntington's disease (HD) and for finding drugs to treat these neurodegenerative disorders [24], [25]. By feeding worms bacteria producing double-stranded RNA, *C. elegans* mutants may be created via the RNA interference (RNAi) approach [26]. By introducing specific RNAi molecules, scientists can target and suppress genes associated with neurodegenerative diseases in *C. elegans*. This manipulation helps researchers understand the effects of these genes on neurodegeneration and provides a valuable platform for studying potential treatments and therapies.

## 2.2 Example of *C. elegans* used for PD Studies

Neurodegeneration studies in *C. elegans* involve inducing neurotoxic insults or genetic mutations associated with PD, leading to the degeneration of DA neurons and the emergence of PD-like symptoms. These combined approaches have significantly contributed to unravelling the molecular intricacies of PD and provided valuable insights into potential therapeutic avenues for treating this devastating neurodegenerative disorder [25].

PD is the second-most prevalent aging-related neurodegenerative disorder and the most prevalent movement disorder [27]. Monogenic parkinsonism is linked to more than 20 genes, including the autosomal dominant SNCA gene. Since  $\alpha$ -Syn is a protein encoded by the SNCA gene, abnormal accumulation and aggregation of  $\alpha$ -Syn is frequently associated with dysfunctionality and degeneration of neurons in PD [28]. Given the role of  $\alpha$ -Syn in the pathology of PD, animal models focusing on dopaminergic (DA) neuronal loss and aggregation of  $\alpha$ -Syn in the brain are deemed invaluable tools for understanding the molecular mechanisms of PD and validating new therapies.

There are available PD model transgenic *C. elegans* strains that specifically target  $\alpha$ -Syn. For instance, the A53T worms exhibit non-progressive neurodegeneration, abnormalities in locomotion, and DA neurodegeneration (Figure 2-3A). Nevertheless, this model has little experimental support in the literature and does not show increased DA neurodegeneration or difficulties in locomotion with age [29]. The NL5901 model exhibits observable inclusions of  $\alpha$ -Syn that grow with age and facilitate biochemical investigation and fluorescent protein interaction studies, including  $\alpha$ -Syn misfolding in body-wall muscle cells (Figure 2-3B). Although reported modulators of  $\alpha$ -Syn misfolding in this model have shown to be discordant with *Drosophila* and mammalian models of PD, it is possible that the usage of  $\alpha$ -Syn fusion protein with yellow fluorescent protein (YFP) may not accurately mimic native structural dynamics [30]. In this thesis, we employed the ERS100 model, a new transgenic *C. elegans* PD model. Figure 2-3C illustrates ERS100 expressing green fluorescent protein- (GFP-) based reporter of human  $\alpha$ -Syn in DA neurons [31]. As such, ERS100 has the potential to validate therapeutic relevance in PD drug discovery projects through monitoring of human  $\alpha$ -Syn expression in DA neurons.

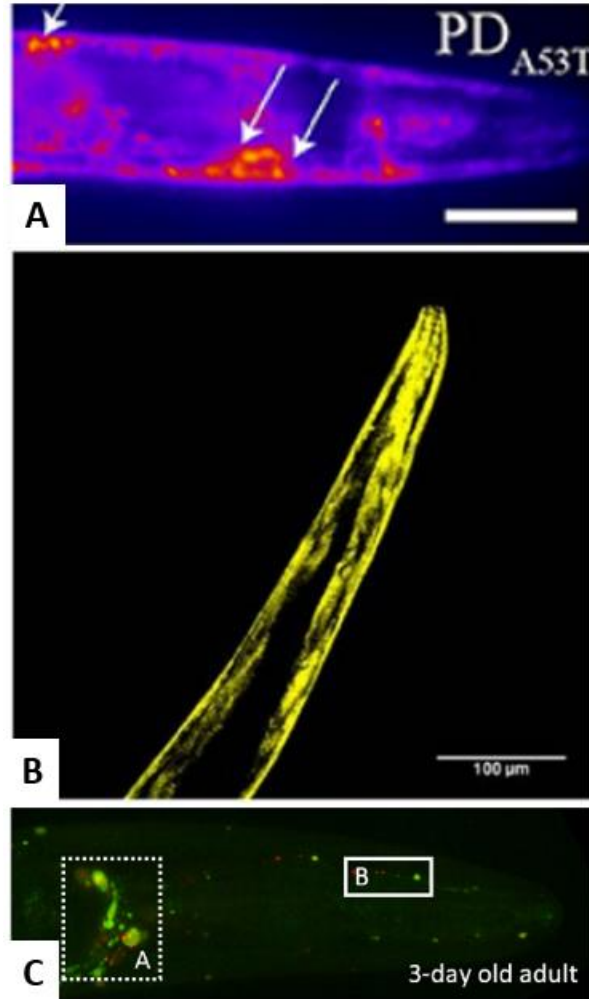


Figure 2-3 Images of PD model *C. elegans* heads. A) 6-day-old A53T PD model *C. elegans* expression. Creative Commons CC-BY license. B) 6-day adult showing intense and merged YFP-labelled granules in the head region. Permission acquired from CNS & neurological disorders drug targets. C) Representative fluorescent image of the head of 3-day-old ERS100. The dotted square line in Panel C highlights the area used for quantifying phenotype A, which refers to aSyn: Venus inclusions. Additionally, the solid square line emphasizes the region used for quantifying phenotype B, relating to cephalic (CEP) dendrite blebbing. Creative Commons CC-BY license

### 2.3 *C. elegans* Assays

The abovementioned PD model *C. elegans* has proven instrumental in advancing the understanding of the disease via behavioural and neural assays. Behavioural assays are employed to assess motor impairments in these worms, such as reduced locomotion, thrashing and altered response to environmental cues [32]. Additionally, neuronal imaging techniques, including calcium imaging, enable the monitoring of dopaminergic neurons and their functional changes in response to  $\alpha$ -Syn aggregation. Moving on to life span assays, *C. elegans* longevity studies have

revealed potential therapeutic targets for PD, as genetic manipulations and drug interventions that extend the worm's lifespan often exhibit neuroprotective effects [33]–[35].

*C. elegans* has also offered extraordinary insights into the biology of ageing since finding single-gene mutations that double its lifetime [36]. Worms' lifespan assays have shown to be an effective instrument for evaluating the effects of numerous genetic, physiological, and environmental variables on organismal ageing [37]. Such assays will be in synchronized groups at periodic times (e.g., every 1 or 2 days), and the data is then analytically examined. This discussion explores various techniques for conducting *C. elegans* assays utilizing liquid, solid, or microfluidic media.

### **2.3.1 Liquid Media Methods**

Figure 2-4 illustrates liquid culture-based media S-basal buffer and concentrated *E. coli* that are commonly used in *C. elegans* lifespan tests. These assays are excellent for assessing the impact of food components and chemical agents on worms due to the uniform nature of the liquid medium. By diluting dietary microorganisms in liquid, these experiments may also be used to investigate the effects of dietary limitations on lifespan. Nonetheless, liquid culture-based lifespan tests have several drawbacks. In liquid environments, manipulating worms with a platinum wire is challenging, and growing worms in liquid media necessitates additional equipment, such as a platform shaker for aeration [38].

### **2.3.2 Solid Media Methods**

The most frequent *C. elegans* lifespan assay method is agar-based solid media methods. Typical solid media methods include nematode growth media (NGM) agar plates inoculated with bacterial food. The advantage is that it permits determining whether worms are alive or dead quite simply. On the other hand, worms commonly crawl off plates or burrow into agar, resulting in accidental worm loss for examination. Furthermore, during lifetime experiments, NGM plates can be desiccated; however, this problem can be avoided by frequently shifting worms to fresh plates, as seen in Figure 2-4 [38].

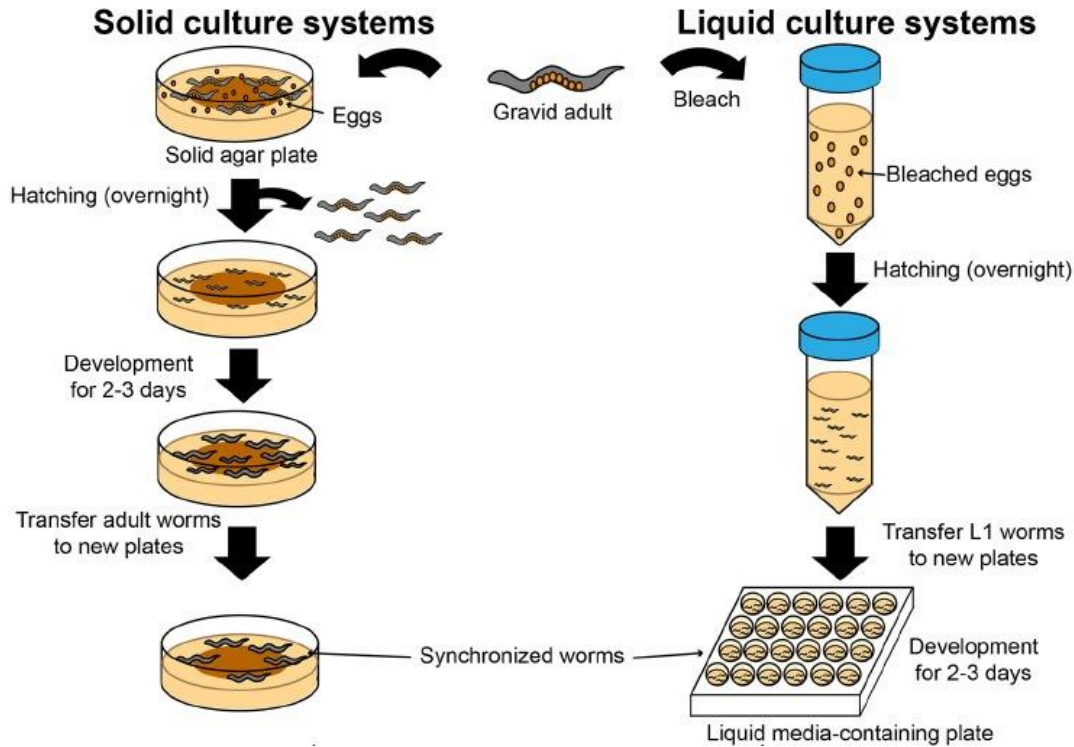


Figure 2-4 Assays can be conducted using either solid or liquid media, with the former being the predominant method employing agar-based media. The latter, which employs S-media, is commonly utilized for evaluating the impact of chemicals on various factors [38]. This image is used under a Creative Commons Attribution 4.0 International (CCBY) License.

### 2.3.3 Microfluidic Methods

Microfluidics has found several applications in the field of *C. elegans* research, primarily due to the organism's small size and transparent nature, which make it amenable to manipulation and observation at the microscale. Microfluidics allows for automated worm isolation, chemical delivery with easy microscale manipulations, and parallel or serial worm observation, allowing for a degree of control not feasible in liquid containers or agar plates. In addition to boosting throughput, the compact size and decreased need for reagents make microfluidic chips a cost-effective choice for various assays. Because of their great sensitivity and potential for test downsizing, fluorescence-based readouts using microfluidic devices are among the most widely employed in biochemical experiments [20]. Here are some common categories of microfluidics applications in *C. elegans* research:

**Phenotypic Analysis and Behavior Studies:** Microfluidic platforms can facilitate the precise manipulation and immobilization of *C. elegans* for detailed phenotypic analysis. They enable the

investigation of various behaviours, such as locomotion [39], feeding [40], response to stimuli [41], and mating [42], by providing controlled environments and imaging capabilities.

Hulme *et al.* [39] developed a microfluidic device designed for culturing numerous individual nematode worms in separate chambers. (Figure 2-5A) illustrates how each chamber provides a controlled environment for a single worm, starting from the fourth larval stage until its natural death, allowing for continuous observation of individual worms throughout their adult lifespan. Additionally, the device incorporates microfluidic worm clamps situated alongside the chambers, which facilitate temporary immobilization of each worm at regular intervals, as seen in Figure 2-5B. By utilizing this device, it became possible to monitor changes in body size and locomotion of individual worms over their entire lifespans. This longitudinal approach within the device enabled the identification of age-related phenotypic alterations that correspond to the lifespan of *C. elegans*.

The development of microfabricated platforms holds immense potential for advancing physiological and genetic research by enabling automated cultivation and behavioural observation of animals. Kim *et al.* [40] introduced an automated microfluidic system, a compact disc (CD), specifically designed for cultivating, feeding and monitoring *C. elegans*. Figure 2-5C illustrates how this CD-based platform incorporates automated feeding, waste removal, and live-animal microscopy features. The system comprises cultivation chambers, nutrient chambers, waste chambers, interconnected channels, and venting holes. The CD platform achieves automatic feeding and waste removal processes by utilizing centrifugal force-driven fluidics. Unlike other microfluidic technologies that primarily focus on fluid or particle transportation, this centrifuge-based system is particularly well-suited for flow sequencing, mixing, capillary measuring, and switching tasks. These functionalities are realized through the combined utilization of centrifugal, Coriolis, and capillary forces within a dedicated microfluidic network. As a result, the CD cultivation system possesses the ability to incorporate diverse molecular, biochemical, and pharmacological assays, facilitating real-time physiological and behavioural assessments of live animals.

To study neuronal behaviour in *C. elegans*, Chronis *et al.* [41] encountered challenges in delivering stimuli and monitoring neuronal activity within a controlled environment. They developed two

microfluidic chips to overcome these obstacles: the "behaviour" chip and the "olfactory" chip. The behaviour chip (Figure 2-5E) allowed them to examine the correlation between the locomotion pattern of *C. elegans* and the activity of AVA command interneurons. On the other hand, the olfactory chip-enabled them to record responses from ASH sensory neurons when exposed to a high-osmotic-strength stimulus. Through the observation of neuronal responses in these microfluidic devices, they uncovered previously unknown properties of AVA and ASH neurons. These chips have the potential to further explore the relationship between sensory neurons, interneurons, motor neurons, and the behavioural patterns of *C. elegans*.

*C. elegans* is highly valued in genetic research and drug screening due to its simplicity, ease of maintenance, genetic manipulability, and relevance to human biology. However, the challenges associated with handling these tiny and mobile organisms with precision in both space and time have posed limitations. To address this, Chung *et al.* [42] have developed a microfluidic device that enables rapid behaviour-based chemical screening in *C. elegans*, as depicted in Figure 2-5E. Figure 2-5F displays this user-friendly device's key components, allowing efficient loading and housing of the nematodes in a chamber array for chemical screening. A simple two-step loading process enables simultaneous loading of many animals within a few minutes without requiring expensive or active off-chip components. Moreover, precise delivery and exchange of chemicals with high temporal accuracy can be achieved. To showcase these capabilities and demonstrate the device's ability to measure time-dependent responses to chemicals, they conducted experiments characterizing the transient response of worms exposed to various concentrations of anesthetics. Furthermore, they utilized the device to investigate the impact of chemical signals from hermaphrodite worms on male behaviour. By maintaining a large population of freely moving worms within a single field of view for an extended duration, they observed an increase in a specific behaviour in males exposed to a worm-conditioned medium.

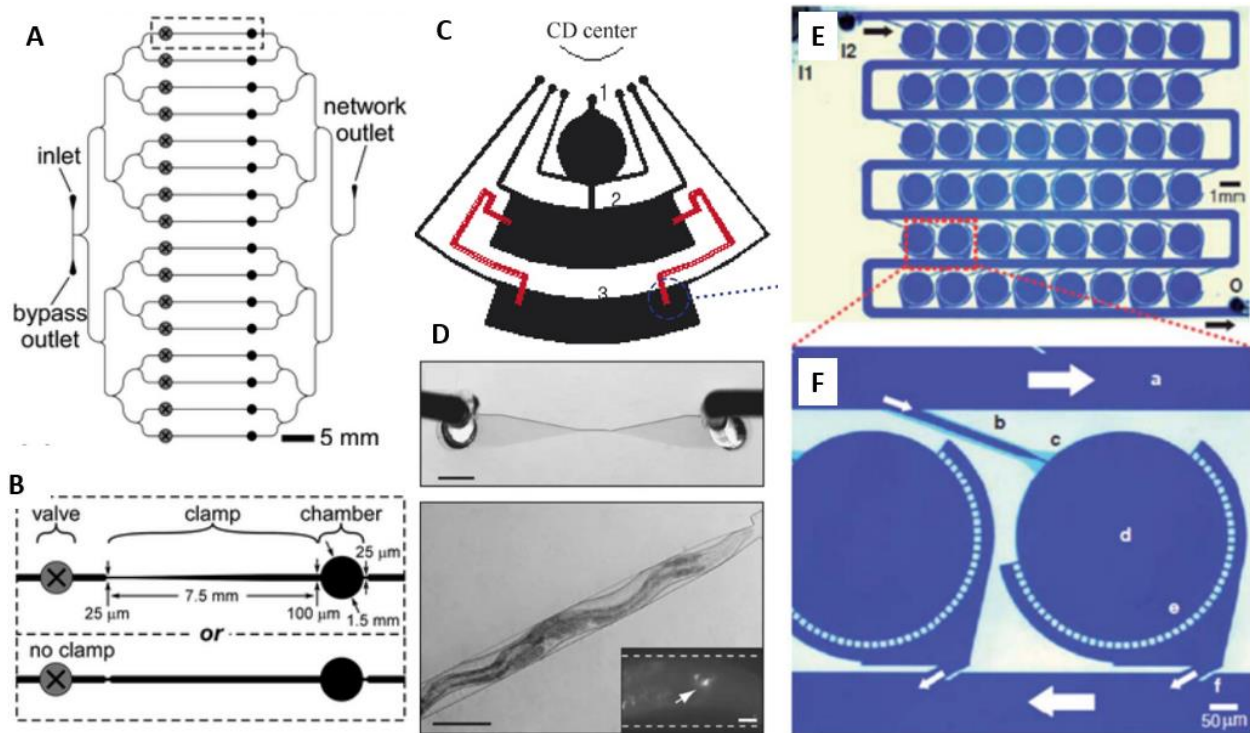


Figure 2-5 The phenotypic analysis and behaviour of microfluidics studies schematics and designs A) An array of 16 chambers was designed, with branching distribution channels delivering *E. coli* suspension from the inlet to the outlet. B) A single circular chamber with an adjoining clamp was designed, specifying dimensions. Images used with permission from the Royal Society of Chemistry. C) The microfluidic structure used in CD cultivation consists of a nutrient reservoir (1), a cultivation chamber (2), and a waste reservoir (3). Image is used with permission from Elsevier. D) The behaviour chip is depicted at the top, while the image at the bottom showcases the trapping of individual worms. An inset displays a fluorescence image of an AVA interneuron expressing G-CaMP. The image is used with permission from Springer Nature. E) The image shows the device filled with dye, revealing a pattern of 48 circular chambers interconnected by a serpentine channel. Black arrows indicate flow direction. F) Components of each chamber are labelled as follows: a (serpentine channel), b (single worm loading channel), c (stopper), d (circular chamber), e (diverging channels), and f (chamber outlet). White arrows indicate flow direction. Images used with permission from the Royal Society of Chemistry.

**Developmental Biology and Embryogenesis:** Microfluidics can be utilized to investigate the embryonic development of *C. elegans*. The devices allow the precise control of environmental conditions, such as temperature, oxygen concentration, and nutrient gradients, enabling the study of developmental processes and the effects of environmental cues on embryogenesis [43].

*C. elegans* resides within a diverse habitat characterized by temperature fluctuations, varied physical obstacles, and the presence of other nematodes, both beneficial and harmful bacteria and nematode-trapping fungi. Considering these conditions, *C. elegans* has developed the ability to detect and differentiate among a range of environmental cues. Their laboratory-based quantifiable behaviours, evoked by sensory stimuli, offer a high-resolution means of studying their sensory capabilities. Remarkably, this is accomplished by a compact sensory nervous system consisting of

fewer than 100 sensory neurons. Researchers have successfully linked specific sensory responses to individual neuron types by leveraging powerful molecular genetic tools. Goodman *et al.* [43] explored the sensory neurons and molecules responsible for *C. elegans* perception and response to physical stimuli. Novel methods utilizing microfluidics-based devices are on the rise, providing a supplementary approach to administering mechanical stimuli to either freely moving or immobilized *C. elegans* nematodes. Emphasis is placed on the pathways that enable the detection of mechanical and thermal cues while briefly touching upon the nematode's ability to sense magnetic and electrical fields, light, and humidity levels. Additionally, they summarized the knowledge derived from in vivo calcium imaging and whole-cell patch-clamp electrophysiology studies, highlighting the sensitivity and response dynamics of specific classes of mechano- and thermosensory neurons in *C. elegans*. Furthermore, they examine the roles of conserved molecules and signalling pathways that contribute to the nematodes' highly sensitive responses to mechanical and thermal stimuli.

**Genetic Manipulation and Single-Cell Analysis:** Microfluidics platforms can aid in genetic studies and single-cell analysis of *C. elegans*. They enable the sorting and isolating of individual worms [44], facilitating downstream genetic analysis and gene expression profiling [40]. *C. elegans* is a valuable model organism for investigating various human diseases and aging aspects. To conduct specific bio-assays with worms at different developmental stages, it is essential to have synchronized populations. This ensures accurate observations and prevents the interference of overlapping stage-specific responses. Dong *et al.* [44] introduced a microfluidic method for sorting *C. elegans* based on their size. Their approach capitalizes on the deformable nature of polydimethylsiloxane (PDMS) transfer channels, which connect two worm chambers on the chip, as shown in Figure 2-6A. By applying external pressure, they can adjust the effective cross-section of these channels, creating customizable filter structures for worm sorting experiments. Importantly, this adjustment can be achieved without altering the device's design parameters. Through optimization of pressure control, they achieved highly efficient extraction of larvae at a specific developmental stage from a mixed worm culture with nearly 100% accuracy. The sorting process operates at high throughput, enabling the sorting of up to 3.5 worms per second. Additionally, our method allows for generating mixed populations of larvae at adjacent stages or adjusting their ratio within the microfluidic chamber. Furthermore, their device facilitates the

extraction of embryos from adult worm populations, facilitating the subsequent culture of precisely age-synchronized nematode populations or embryo-based assays. Notably, the sorting device relies solely on geometrical parameters and can be controlled through simple fluidic and pressure manipulation.

**Neurobiology and Neuronal Imaging:** Microfluidics can immobilize *C. elegans* while maintaining their neuronal activity. This allows researchers to perform high-resolution imaging of neuronal structures and activity in vivo [13]. Selective plane illumination microscopy (SPIM) is an emerging fluorescence imaging technique that allows noninvasive volumetric imaging of *C. elegans*. However, the adoption of SPIM systems in academic and research institutions has been limited due to their high cost and technical complexities. To promote the widespread use of SPIM for studying neuronal expressions in *C. elegans*, there is a need for simple and affordable solutions that can convert standard wide-field (WF) microscopes into rapid SPIM platforms. Our lab developed a straightforward and cost-effective optofluidic add-on device that enables rapid and immobilization-free volumetric SPIM imaging of *C. elegans* nervous systems using conventional fluorescent microscopes. We adopted an approach where we designed a polydimethylsiloxane (PDMS)-based device with integrated optical and fluidic components. This optofluidic chip, which can be attached to a standard WF microscope, featured an integrated PDMS cylindrical lens that generated a light-sheet across a microchannel. *C. elegans* samples continuously flowed through the L-shaped microchannel, and the native objective of the microscope captured cross-sectional SPIM images as the worms passed through the light sheet, as depicted in Figure 2-6B. The results of our study demonstrated successful on-chip SPIM imaging of different *C. elegans* strains. This approach allowed for the visualization of the entire neuronal system within seconds, achieving single-neuron resolution and high contrast without the need for worm immobilization. We also demonstrated the ability to reconstruct three-dimensional fluorescent images of *C. elegans* by combining the acquired cross-sectional two-dimensional images. The point spread function measurements indicated a full-width at half-maximum width of 1.1  $\mu\text{m}$  and 2.4  $\mu\text{m}$  in the lateral and axial directions, respectively.

**Drug Screening and Toxicology:** Microfluidic devices can expose *C. elegans* to drugs or chemical compounds in controlled environments. The devices allow precise control over exposure concentration, timing, and duration, enabling high-throughput drug screening and toxicology

studies [45]. Implementing microfluidic technologies for high-throughput and high-resolution imaging of *C. elegans* models presents significant challenges. These systems need to address multiple requirements: compatibility with automated platforms, simplified interfaces, accommodating many samples in limited space, and immobilizing the animals optimally for high-resolution imaging. Existing complex channel geometries with multiple fluid inputs are unsuitable for scaling up and simultaneously testing multiple samples on a single chip. To overcome these challenges, Ben Yakar [45] developed a hybrid microfluidic device that bridges the gap between the macro- and microworld of microfluidics. The device features a standard multiwell format on the exterior for seamless integration with existing automated platforms. Internally, microfabricated channels are directly connected to the multiple wells, allowing the handling of many animals per test. This parallel sample preparation capability enables the efficient use of multi-channel sample loader equipment. Figure 2-6C displays the platform's simplified single-input and single-output fluid interface, eliminating complex interfaces for easier connectivity and flow control. Furthermore, the microfluidic immobilization channels are designed with tapered geometry and varying heights to maintain the animals in their natural lateral orientation. This orientation optimizes optical imaging of cellular processes, such as neuronal processes, along the ventral cord of the animals. By combining these innovative features, their microfluidic technology enables high-throughput and high-content screening of *C. elegans* disease models with subtle fluorescence phenotypes.

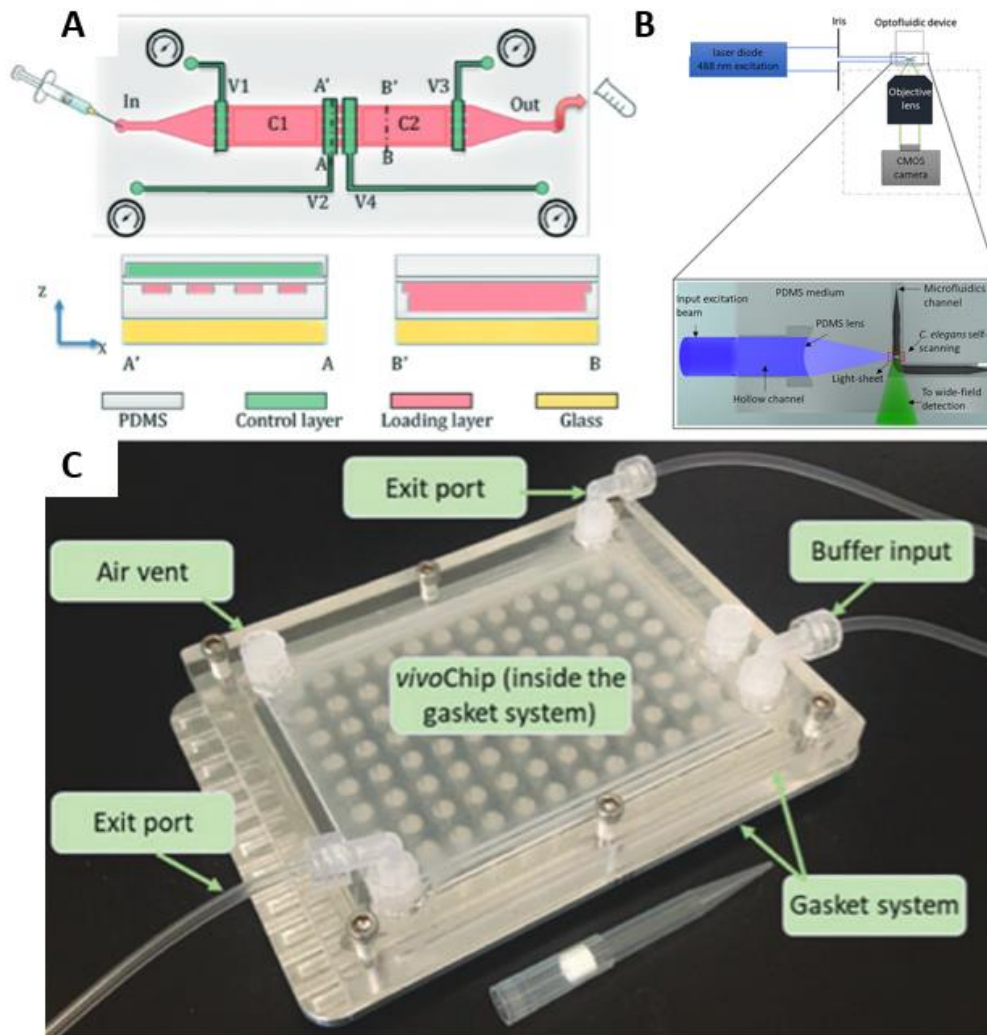


Figure 2-6 Schematic and actual platforms for *C. elegans* manipulation A) The diagram illustrates the worm sorting device illustrating various layers. B) (Top) Replacement of epi-illumination with a generated light-sheet in the host microscope. (Bottom) The working principle of the optofluidic device involves focusing a collimated input beam using the integrated PDMS lens, resulting in the generation of a light-sheet inside the microfluidic channel. Copyright 2021 Society of Photo-Optical Instrumentation Engineers (SPIE). C) The photograph shows the gasket system that holds a 96-well vivoChip in place. This image is used with permission from Mary Ann Liebert, Inc..

## 2.4 Fluorescence Imaging of *C. elegans*

Because of the worm's simplicity of genetic manipulation and optical transparency, fluorescence microscopy can conveniently be used to see the worm's internal cells and organs without dissecting and sacrificing the worm. In addition, biologists can explore various biological problems *in vivo* by producing fluorescent markers. Fluorescence is a phenomenon in which certain substances, called fluorophores, absorb light and emit light at specific wavelengths. In biology, fluorescence has diverse applications. It is used to label specific molecules or cells,

allowing researchers to visualize and track their location and interactions within cells or tissues [1].

Fluorescence microscopy enables high-resolution imaging of fluorescently labelled samples, revealing subcellular structures and dynamic processes. Epi-fluorescence WF microscopes make up a large portion of current fluorescence microscopes. These microscopes are commonly used in biology and provide a basis for more advanced designs, such as confocal (CM) and light sheet microscopy. An inverted microscope is generally preferred to an upright one as high-magnification immersion objectives require a small working distance, and having connection pins and tubing facing up is more practical [46].

While widely used in biological imaging, WF microscopy has certain limitations that can affect image quality and resolution. In WF microscopy, as depicted in Figure 2-7A [31], excitation light (blue arrows) passes through the objective lens and illuminates the sample. Fluorescence emitted by the sample (green arrows) is collected by the same objective lens and passes through the dichroic mirror (DM). However, several issues arise with this configuration.

**Out-of-focus light:** When using epi WF, light emitted from above and below the focal plane of the objective lens contributes to the final image. This out-of-focus light can reduce image contrast and degrade resolution, resulting in a loss of fine details.

**Background noise:** Epi WF captures both signal (desired fluorescence) and background noise (unwanted autofluorescence and scattered light). This noise can reduce image clarity and obscure important features.

Confocal microscopy (CM) is often employed to obtain high-resolution images. CM rejects out-of-plane light, resulting in improved image quality and resolution. In CM, a confocal pinhole is placed in front of the detector (depicted in Figure 2-7B). This pinhole eliminates out-of-focus light by allowing only the fluorescence emitted from the focal plane to reach the detector. As a result, the image primarily contains in-focus light, leading to sharper and more detailed images.

By rejecting out-of-plane light, CM minimizes the contribution of out-of-focus fluorescence from above and below the focal plane. This rejection helps enhance the contrast, resolution, and overall image quality by eliminating the blur caused by out-of-focus light.

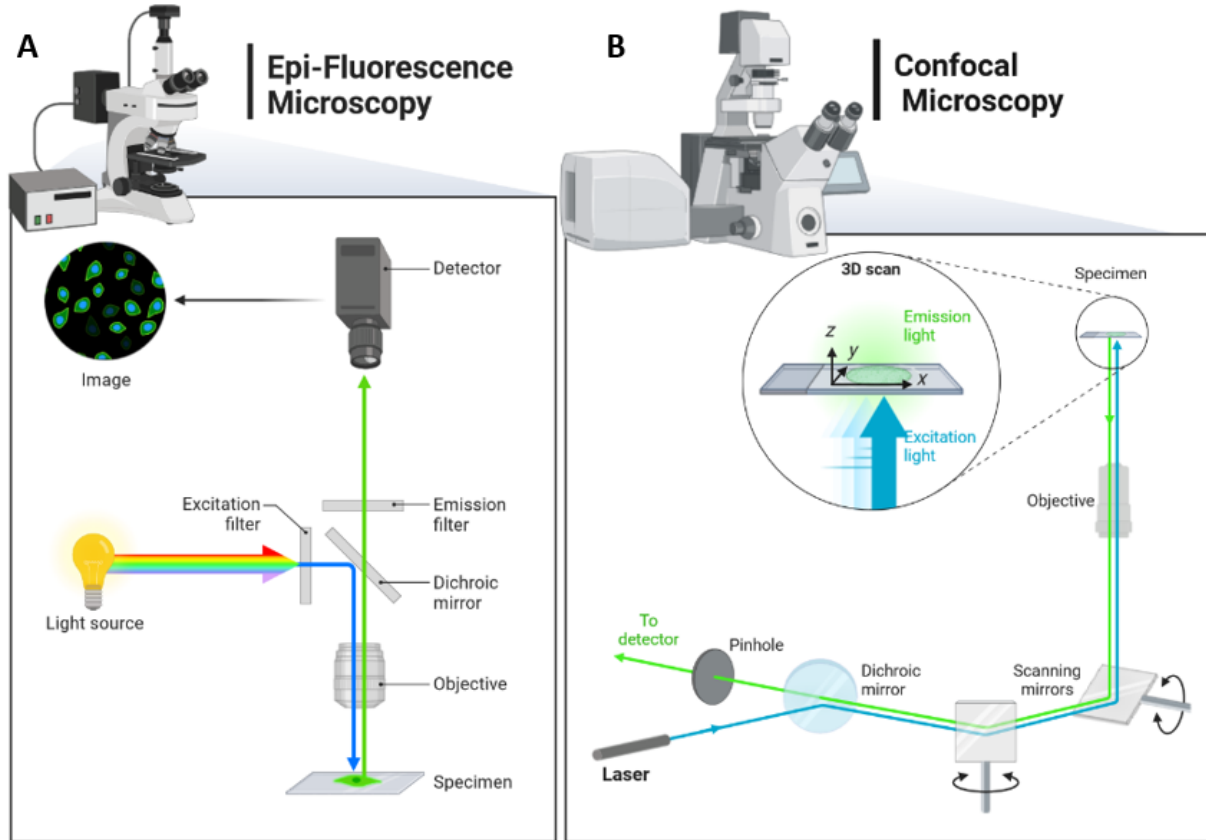


Figure 2-7 Schematic figure of epi-WF and confocal laser scanning microscopy A) Epi-WF microscopy setup, illustrating the excitation light path (blue arrow) and emitted fluorescence detection (green arrow). The excitation light illuminates the entire field of view, while the emitted fluorescence is captured by the objective lens and directed to the detector. B) The setup of confocal laser scanning microscopy showcases the laser excitation beam (blue arrow) focused on a single point within the specimen. The emitted fluorescence (green arrow) is selectively collected by a pinhole before reaching the detector, enabling optical sectioning and improved resolution compared to WF microscopy. (Made by BioRender.com)

Similar to other fields of biology, WF microscopy is frequently used for studies involving *C. elegans* PD models. For example, Tsai *et al.* [47] used the inverted fluorescence microscope to explore the influence of Betulin as a possible medicine in *C. elegans* PD models. The Betulin's effectiveness was determined by monitoring and measuring neuronal responses in 6-OHDA-treated worms. Figure 2-8 is created by the sample's focal plane with a superimposed out-of-focus signal in a conventional WF microscope, illustrating the weak spatial resolution [31]. Epi-fluorescence microscopy with a high-magnification objective is the most common approach since

it provides adequate resolution for most situations and is quick (compared to CM), although the picture quality might place a higher demand on image processing [48].

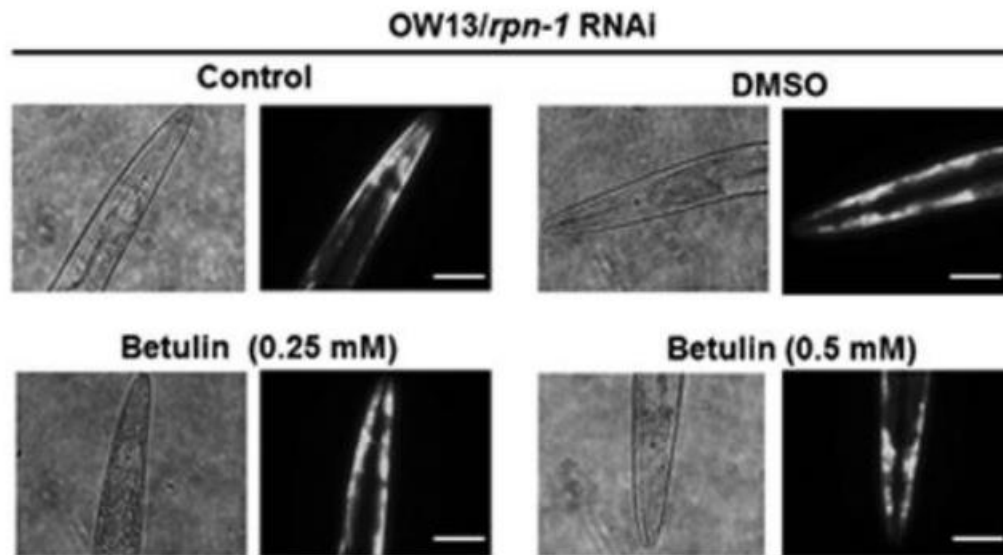


Figure 2-8 Representative fluorescence images of  $\alpha$ -syn accumulation in the head region are depicted to demonstrate the YFP expression pattern in the muscles of OW13 worms subjected to rpn-1 RNA interference treatment [47]. Images are used under a Creative Commons Attribution 4.0 International (CCBY) License.

Ham *et al.* [30] utilized CM to investigate genome-wide RNA interference, aiming to identify processes associated with inclusion formation. Through this approach, they pinpointed 80 genes, the knockdown of which led to a premature surge in the number of inclusions. This investigation provided valuable insights into the molecular underpinnings of Parkinson's disease. The relocation of YFP fused to human alpha-synuclein to inclusions, illustrated in Figure 2-9, becomes apparent as early as day 2 post-hatching, intensifying in number and size as the animals age until late adulthood. In contrast, YFP alone remains diffusely distributed throughout the aging process.

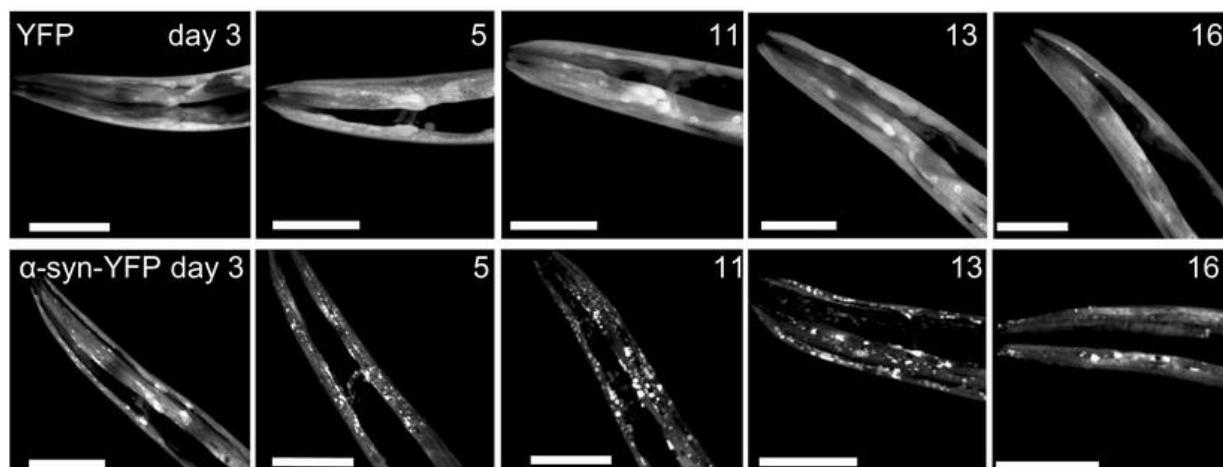


Figure 2-9 The expression of  $\alpha$ -synuclein-YFP in the head region of aging transgenic *C. elegans* is illustrated using confocal laser scanning images [30]. This image is used under a Creative Commons Attribution License. Copyright © 2008 [van Ham *et al.*].

Comparing Figures 2-8 and 2-9, CM is preferred over WF when more resolution and contrast are needed to identify smaller details. CM lights a single point in the focal plane that is swept in the lateral direction to create a complete image, unlike traditional epi-fluorescence microscopy, which exposes the whole field simultaneously and stimulates fluorescence throughout the sample's depth [31]. On the one hand, CM produces high-quality images of *C. elegans* neuronal activity, but like WF, because of the prolonged scanning procedure, it is vulnerable to photodamage and photobleaching [4], [49]. Light sheet microscopy has been suggested to address these limitations. It illuminates only the detection objective's focal plane to capture high-contrast images with minimal photodamage [50]–[53]. Compared to CM, it also offers faster imaging speed as it captures images in a WF manner [54].

## 2.5 Light Sheet Microscopy

The theory of light sheet microscopy was first established in 1903 when a German chemist named Richard Zsigmondy and a physicist named Henry Siedentopf partnered to perceive colloidal gold. However, at the time, it needed the technical capability to become a viable and widely used imaging device for *in vivo* biological research. The revival of light sheet microscopy as a functional imaging platform was presented to the biological sciences in 2004 and was named selective plane illumination microscopy (SPIM) [35].

In recent years, SPIM has emerged as a powerful technique for visualizing biological specimens with exceptional clarity and minimal photodamage. This section aims to provide an in-depth understanding of the working principle behind light sheet imaging, highlighting its advantages, limitations, and applications.

### 2.5.1 Fundamentals of Light Sheet Imaging

The working principle of a basic light-sheet microscope is depicted in Figure 2-10. Unlike conventional WF and CM, which utilize a single optical path for illumination and detection, light-sheet microscopy decouples the illumination and detection paths. SPIM consists of two orthogonally oriented optical arms in its conventional configuration: an illumination arm that generates a thin light sheet for excitation and a detection arm that collects the emitted fluorescence.

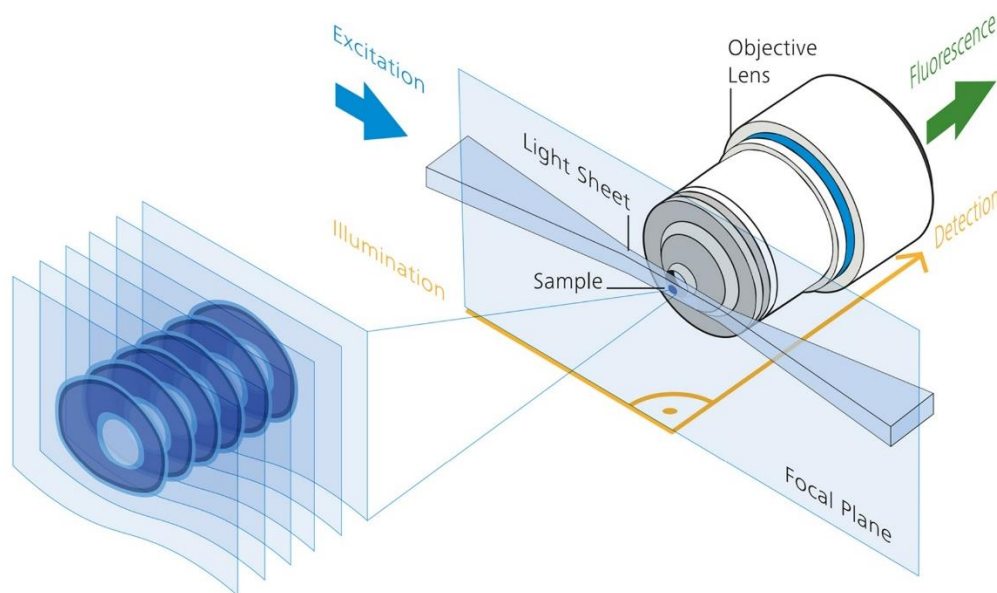


Figure 2-10 The fundamental configuration of a light-sheet microscope (LSFM) involves the independent arrangement of the illumination or excitation path and the detection or emission path. Within this setup, a thin sheet of light is generated to specifically illuminate and excite the region of interest within the sample, aligning precisely with the focal plane of the detection objective [55].

In this orthogonal configuration, the light sheet coincides with the focal plane of the detection objective. As a result, only the portion of the sample within the focal plane is illuminated by the light sheet. This selective illumination eliminates out-of-focus fluorescence, enhancing contrast compared to WF microscopy. Additionally, it prevents unnecessary exposure of fluorophores outside the thin volume of the light sheet, minimizing the risk of phototoxicity and photobleaching.

Having covered the fundamental principles of light sheet microscopy, let us now delve into the generation of the light sheet via the illumination arm and other components involved.

## 2.5.2 Light Sheet Generation

Essentially, the purpose of the illumination arm in a light-sheet microscope is to generate the excitation light sheet. It is created using a cylindrical lens or a combination of a cylindrical lens and an objective lens within the illumination arm. In a basic setup, a cylindrical lens is positioned at a specific distance from the imaging plane, where the collimated laser beam is transformed into a thin light sheet (as shown in Figure 2-11A). Advanced SPIM setups employ a combination of an objective lens and a cylindrical lens to minimize aberrations that can occur when using a single cylindrical lens to achieve a diffraction-limited light sheet. In this arrangement, a cylindrical lens is placed in the rear focal plane of the objective lens, and the objective lens is positioned in such a way that its focal plane aligns with the detection axis [56]. (as depicted in Figure 2-11B)

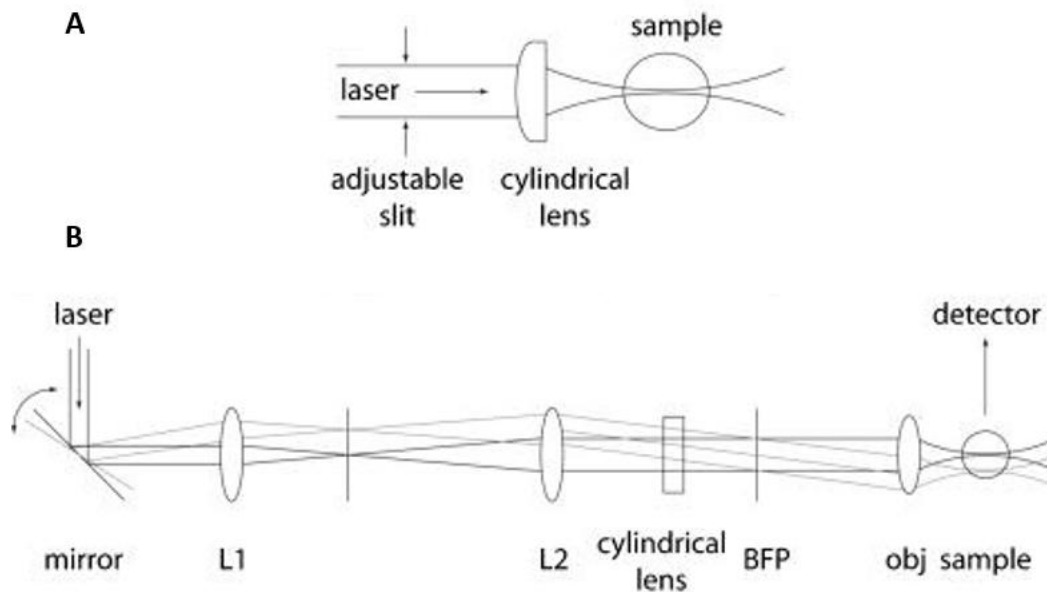


Figure 2-11 The diagram illustrates the optical arrangement of the illumination unit. A) In its simplest form, a single cylindrical lens is employed to focus a collimated beam onto the sample, creating a light sheet. The thickness of the light sheet is adjustable using a slit, which also allows for control of the numerical aperture (NA) of the illumination lens. B) To achieve a diffraction-limited light sheet in selective plane illumination microscopy (SPIM), an improved setup is employed. This configuration, illustrated with optical components and ray traces in planes perpendicular to the light sheet, includes an adjustable gimbal-mounted mirror that enables precise alignment of the light sheet with the detection unit's focal plane (not depicted). A relay telescope formed by lenses L1 and L2 facilitates the generation of the light sheet by combining a cylindrical lens with an objective (obj). The diagram also indicates the position of the back focal plane (BFP) [56]. This image is used under a Creative Commons CC BY License.

Two commonly used types of light sheets are Bessel beams and Gaussian beams. Bessel beams are non-diffracting, self-reconstructing beams that maintain their shape over long propagation distances. Gaussian beams, on the other hand, are more widely used and provide a tighter focus, but they diffract and spread out as they propagate.

In conventional light-sheet microscopes, utilizing a Gaussian beam to form the light sheet is typical, as illustrated in Figure 2-12A. The properties that significantly impact the microscope's performance are the thickness and length of the Gaussian light-sheet, which are carefully chosen according to the characteristics of the sample under investigation. Twice the beam waist determines the thickness of the light sheet ( $w_0$ ) at the focal plane, and its value can be calculated using Equation 2-1.

$$\text{Equation 2-1} \quad 2w_0 = \frac{2\lambda}{\pi NA_{illumination}}$$

In this equation  $\lambda$  is the wavelength of the illumination light and  $NA_{illumination}$  is the NA of the illumination lens. The length of the light sheet, which is twice the Rayleigh length ( $Z_r$ ), refers to the distance the light sheet does not spread beyond twice its thickness. This length is a measure of the region where the light sheet maintains reasonable uniformity, which translates to the field of view of the light sheet microscope. This length can be calculated using Equation 2-2.

$$\text{Equation 2-2} \quad Z_r = \frac{\pi w_0^2}{\lambda}$$

The thickness of the light sheet in a light-sheet microscope is directly related to the system's ability to achieve optical sectioning and, consequently, its axial resolution. Thinner light sheets tend to provide better axial resolution. However, thinner light sheets also diverge more quickly from the focal point, resulting in a smaller usable field of view. This creates an inherent trade-off between the axial resolving power and the extent of the usable field of view in light-sheet fluorescence microscopy (LSFM), as depicted in Figure 2-12B [57].

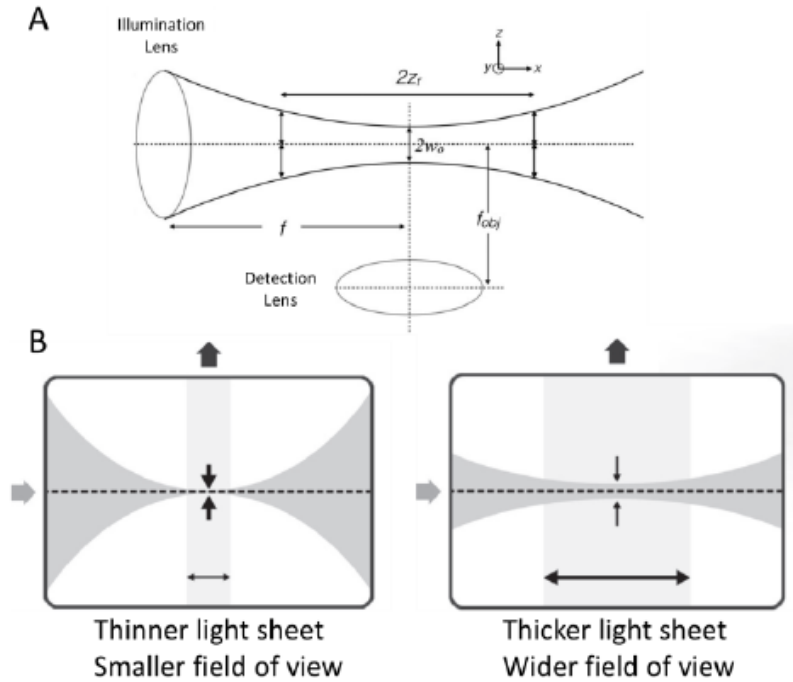


Figure 2-12 Gaussian beam characteristics A) Schematic of SPIM illumination and detection arm with axial ( $2w_0$ ) and lateral resolution ( $Z_r$ ) displayed. [54] B) A thin light sheet provides uniform illumination, but this is limited to a small field of view. On the other hand, a wider field of view can only be achieved by using a thicker light sheet. This trade-off between light sheet thickness and field of view is illustrated, highlighting the relationship between the two aspects [57]. Image used with permission from Elsevier.

The detection unit in an SPIM is akin to the epi-fluorescent configuration commonly found in conventional WF microscopes. It typically comprises a detection objective lens, an emission filter, a tube lens, and a WF 2D detector such as a camera. Consequently, the lateral resolution of a light-sheet microscope is equivalent to that of a WF system and can be calculated using Equation 2-3:

$$\text{Equation 2-3} \quad R_{Lateral} = \frac{\lambda_{emission}}{2NA_{detection}}$$

The lateral resolution ( $R_{Lateral}$ ) of a light-sheet microscope, as determined by Equation 2-3, is dependent on the NA of the detection lens ( $NA_{detection}$ ) and the wavelength of the emitted fluorescent light ( $\lambda_{emission}$ ). However, when utilizing a 2D detector such as a CCD or CMOS camera, the camera's characteristics, including pixel density and frame rate, also play a crucial role in determining the final imaging performance. These camera-specific parameters must be considered alongside the optical factors to accurately assess the overall resolution achieved in light-sheet microscopy. Having discussed the resolution aspects of light sheet microscopy, we now focus on the critical issue of sample manipulation and shadowing artifacts.

### 2.5.3 Sample Manipulation

Given the unprecedented optical sectioning ability of LSFM, these systems have the intrinsic ability to visualize the fluorescence expression of samples in 3-D and with high contrast. To do so, however, the sample is typically embedded in a gel-like medium, such as agarose or polyacrylamide, and immobilized to ensure its stability during imaging. The immobilized sample is then moved along the axial direction relative to the light sheet to capture three-dimensional information. The axial movement, in this case, is achieved via automatic translation stages that allow for precise axial movement of the sample. Alternatively, axial scanning can be achieved by translating the excitation and detection objectives along a stationary sample. In either scanning scenario, efficient 3-D scanning of a population of *C. elegans* poses significant challenges, particularly when high-resolution imaging is required. Microfluidic-based solutions have emerged as viable options for the automated and rapid loading of *C. elegans* in light sheet imaging platforms to address these challenges. As mentioned earlier, microfluidic approaches are great candidates to facilitate high throughput and low-cost assays. In this case, the excitation and detection arms of the system are stationary, and samples are rapidly translated through the stationary light sheet in micro channels. Such systems offer faster and more convenient sample loading while enabling continuous imaging of *C. elegans* without disrupting the normal functioning of the platform.

Additionally, microfluidic solutions have the capability to regulate the flow of *C. elegans* through the imaging plane of microscopy systems. The ability to control the flow speed of *C. elegans* in microfluidic systems allows for continuous high-resolution imaging. This control takes into account various factors such as the specimen's characteristics (e.g., shape, size, mass, and fluorophore's emission properties) as well as the specifications of the sensor/camera (e.g., quantum efficiency, sensitivity, and frame rate). By optimizing the flow speed, continuous and detailed imaging of *C. elegans* can be achieved while mitigating motion-related artifacts.

### 2.5.4 Shadowing Artifacts

In light sheet fluorescence microscopy, one common challenge is the occurrence of shadowing artifacts. Shadowing refers to the obstruction or attenuation of the excitation light by the sample or structures within the sample. This can result in incomplete illumination of the specimen, leading

to uneven or distorted fluorescence signals. To overcome the shadowing issue in light sheet microscopy, a technique called multiple excitation paths or multi-view imaging is often employed. In this approach, multiple excitation beams are used to illuminate the sample from different angles or directions. By introducing multiple excitation paths, the likelihood of shadowing is reduced as the sample is illuminated from various viewpoints. The use of multiple excitation paths helps to ensure more uniform illumination throughout the sample, leading to improved image quality and accurate fluorescence measurements.

### **2.5.5 Light Sheet Microscopy Applications**

Three options are normally available for researchers interested in using the light sheet microscopy technology: collaborating with a “light sheet” facility, developing their own microscope, or buying a commercial system. OpenSPIM[58] and OpenSPINMicroscopy[59] are two open-access and do-it-yourself (DIY) platforms with extensive guidelines for constructing and administering basic SPIM systems [58][59]. As opposed to building the platform from scratch, the open-access systems allow the technique to be highly transparent and simply repeatable. Equipment for a single-sided (Figure 2-13A) or dual-sided light sheet configuration (iSPIM or diSPIM, respectively) on an inverted microscope is supplied by Applied Scientific Instrumentation [60]. On the other hand, due to customization or addressing a specific need, some labs must fabricate their own light sheet setup, which can be offered to other scientists to employ in their experiments. (Figure 2-13B)

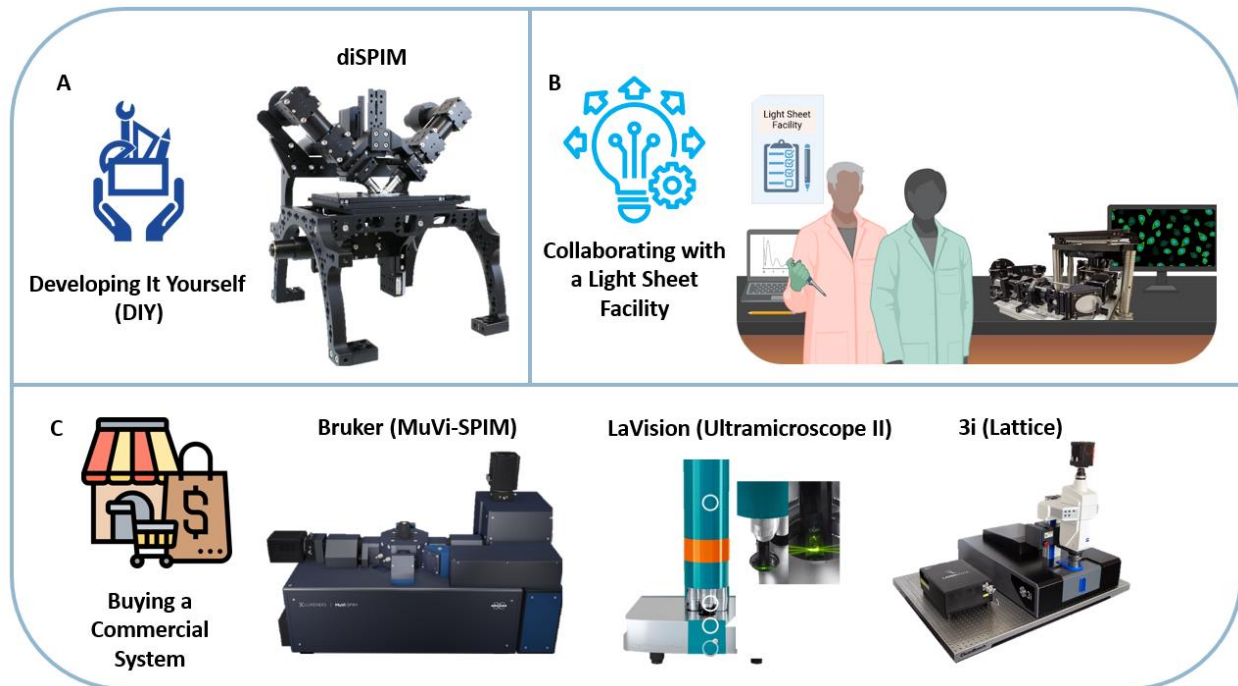


Figure 2-13 Available approaches for scientists to use light sheet microscopy. A) Developing the light sheet from scratch. diSPIM offers manuals and the components to be purchased for scientists to build their own light sheet microscope. Or they can build their own customized platforms. CC Attribution-Share Alike 4.0 International B) Collaborating with the existing light sheet facilities to use their platforms. (Created with BioRender.com using an image from Kennedy Institute of Rheumatology © 2023 University of Oxford) C) The most convenient yet expensive approach is to purchase a commercialized product from well know microscope manufacturers such as Bruker (MuVi-SPIM) © Copyright Bruker 2023, LaVision (Ultramicroscope 2) Copyright © 2023 Miltenyi Biotec and/or its affiliates, and 3i (Lattice) ©2023 Intelligent Imaging Innovations.

The final solution would be the commercially available options, which is the most straightforward approach, but their downside is their cost exceeding \$500k. Zeiss pioneered commercial light sheet systems named Z.1 based on Huisken’s SPIM [61]. Z.1 enabled scientists to image large, live samples from multi-views. This approach is ideal for developmental biology research because it allows researchers to monitor cell dynamics in miniature model organisms or tissues. A light sheet positioned vertically into the chamber from above illuminates both facets of the specimen. The specimen is rotated to obtain photos from various angles, which helps to improve shadowing artifacts. Bruker introduced the MuVi-SPIM microscope, as depicted in Figure 2-13C, a promising option that offers enhanced sample stability and increased image acquisition rates. This microscope is based on Krzic *et al.* [62], which delivers four orthogonal views of the specimen, so there is no need to rotate the sample. While the MuVi-SPIM is designed for fast collection, the InV-SPIM is suited for applications that need continuous imaging. Monitoring cellular and subcellular locations is commonly employed in tiny model organisms and cell cultures. Figure 2-13C illustrates LaVisionBioTech’s Ultramicroscope II, which might be viable for sizable,

transparent, and fluorescently tagged specimens. This technology relies on Hans Ulrich Dodt's ultramicroscope [63] operating idea, with a specific program for addressing the refractive indices disparities caused by transparent tissues. Ultramicroscope II has been effectively used for neurobiology operations such as lymph node exploration and developmental modes in animal models. Based on Chen and coworkers' discovery [51], the Lattice Light Sheet microscope from 3i (Intelligent Imaging Innovations) is available on the market that offers a homogenous light sheet with a sub-micrometre thickness, as seen in Figure 2-13C. A Bessel beam may be used to generate a 0.4  $\mu\text{m}$  light sheet that can be prolonged for 50  $\mu\text{m}$ , making the approach perfect for imaging at the sub-cellular level [54].

### **2.5.6 Advantages and Limitations of Light Sheet Microscopy**

Light sheet imaging offers several advantages over traditional imaging techniques. It provides high-resolution, three-dimensional imaging with minimal photobleaching and phototoxicity. The orthogonal arrangement of illumination and detection reduces out-of-focus background noise, leading to an improved signal-to-noise ratio and image contrast. Light sheet imaging is also well-suited for time-lapse imaging, as it enables rapid imaging of large specimens over extended periods without inducing significant damage. On the other hand, light sheet imaging does have certain limitations. Light scattering and absorption in large, dense specimens can limit imaging depth and resolution. This issue can be addressed via optical clearing of tissue, but the clearing process can alter the sample's native properties and also becomes time-consuming when imaging populations of samples. Additionally, generating a thin light sheet requires precise alignment and calibration, which can be challenging. Finally, the high cost and complexity of light sheet microscopy setups significantly restrict their widespread adoption.

### **2.5.7 *C. elegans* Light Sheet Microscopy**

This section discusses the light sheet microscopy approaches used to study the model organism *C. elegans*. Earlier studies have unveiled the crucial signalling molecules that direct the neurodevelopment of *C. elegans* [64]. Nevertheless, thorough research into the processes that contribute to neural circuit formation during embryonic neurulation has been restricted by phototoxicity and the poor imaging speed of standard imaging methods. Inverted SPIM (iSPIM), a high-speed and less invasive imaging approach, was suggested by Wu *et al.* [7] and allowed the exploration of dynamic neurodevelopmental processes that were previously inaccessible. Figure

2-14A illustrates the structure of the iSPIM, which consists of two optical arms placed on an inverted microscope body and outfitted with excitation and detection objectives. With no detectable phototoxicity, this technical development made it possible to image nematode embryos at a rate of one volume every two seconds during the whole period of embryogenesis (Figure 2-14B).

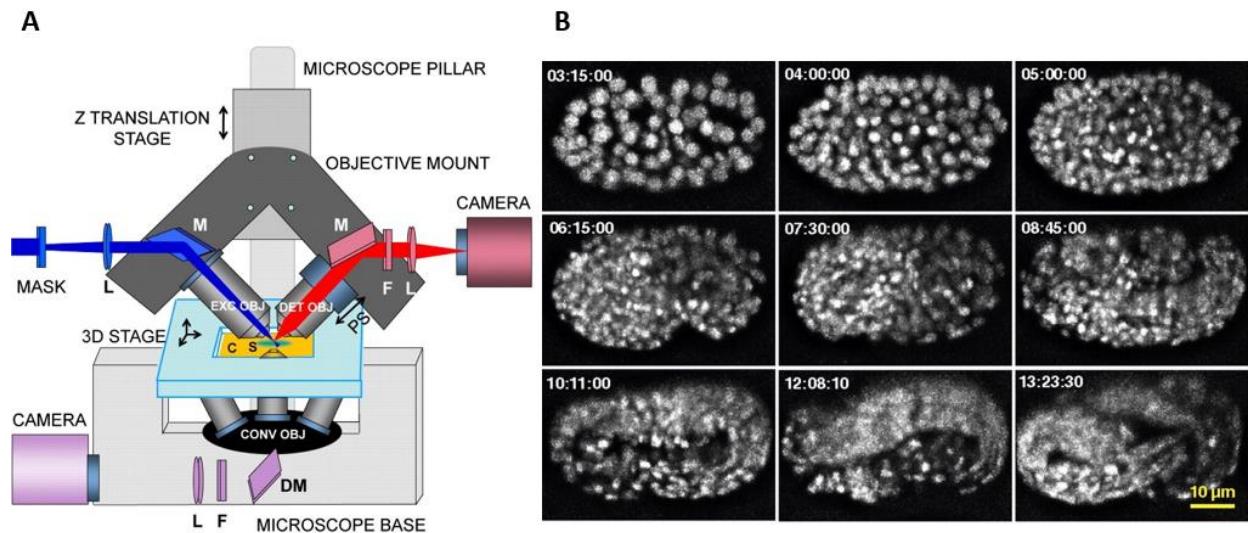


Figure 2-14 iSPIM setup schematic and neural imaging of larvae development A) A Z translation stage is directly bolted onto the illumination pillar of an inverted microscope, onto which two water-immersion objectives are mounted. B) Several maximum-intensity projections have been chosen from a typical embryo to emphasize various stages of its development[7]. Images are used under a Creative Commons License

The same group also made progress when they created diSPIM, which offers an isotropic spatial resolution. The orthogonal orientation of the objectives prevented employing the maximum NA, which reduced the axial resolution in iSPIM. By using the same two objectives in excitation and illumination modes interchangeably, diSPIM made isotropic resolution possible. As a result, compared to iSPIM, diSPIM provided more thorough and extensive information on the evolution of the neuron's wiring throughout embryogenesis (Figure 2-15B). Nevertheless, the instrumentation for this device is more complex, necessitating the addition of substantial imaging electronics to the inverted microscope, as seen in Figure 2-15A [65].

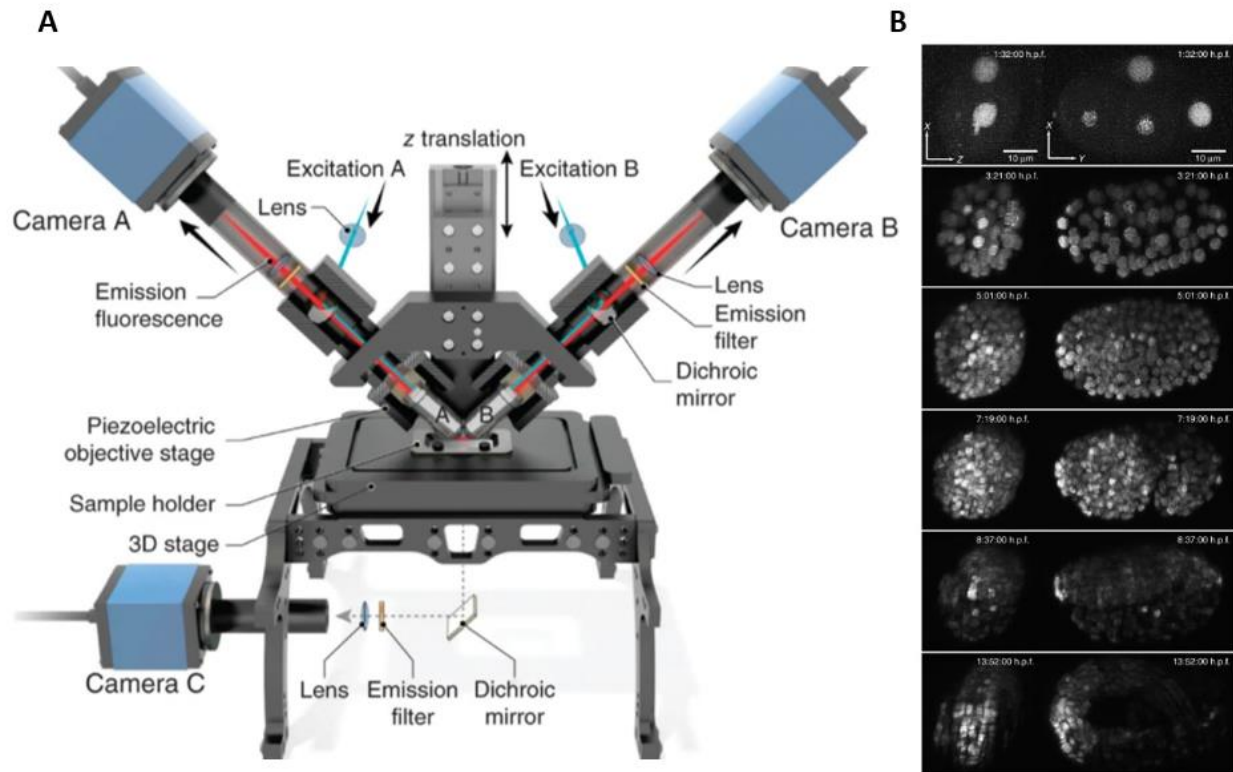


Figure 2-15 A schematic of the assembled diSPIM system is presented. 0.8 NA water-immersion objectives, labelled as A and B, are positioned at right angles on a z-axis translation stage, securely attached to an inverted microscope's illumination pillar. Along with additional optical components, these objectives generate a thin sheet of light that illuminates the sample. Objective A (or B) is used for excitation, while the fluorescence produced is collected through objective B (or A) positioned perpendicular to it. The collected fluorescence is then directed toward camera B (or A) using dichroic mirrors, emission filters, and lenses. B) Using diSPIM, tagged histones were imaged in a *C. elegans* embryo. A live *C. elegans* embryo is shown with nuclear histones in a selection of maximum-intensity projections from a 14-hour imaging experiment [65]. Images used with permission from Springer Nature.

Another technical innovation was Gao's high-resolution light sheet microscopy [66]. This was accomplished by tiling the thin light sheet in the propagation channel, which expanded the effective field of view without sacrificing the axial resolution. Figure 2-16A illustrates the configuration of the abovementioned system containing a binary phase spatial light modulator (SLM) in its illumination arm to alter the excitation beam. The achievement of a 500-nm thick light sheet in a broad field of view made it possible to collect images with a sharper axial resolution than in earlier research, as seen in Figure 2-16B. Due to the requirement for numerous images to be produced in a single imaging plane, this method's imaging speed was slower than non-tiling approaches [66].

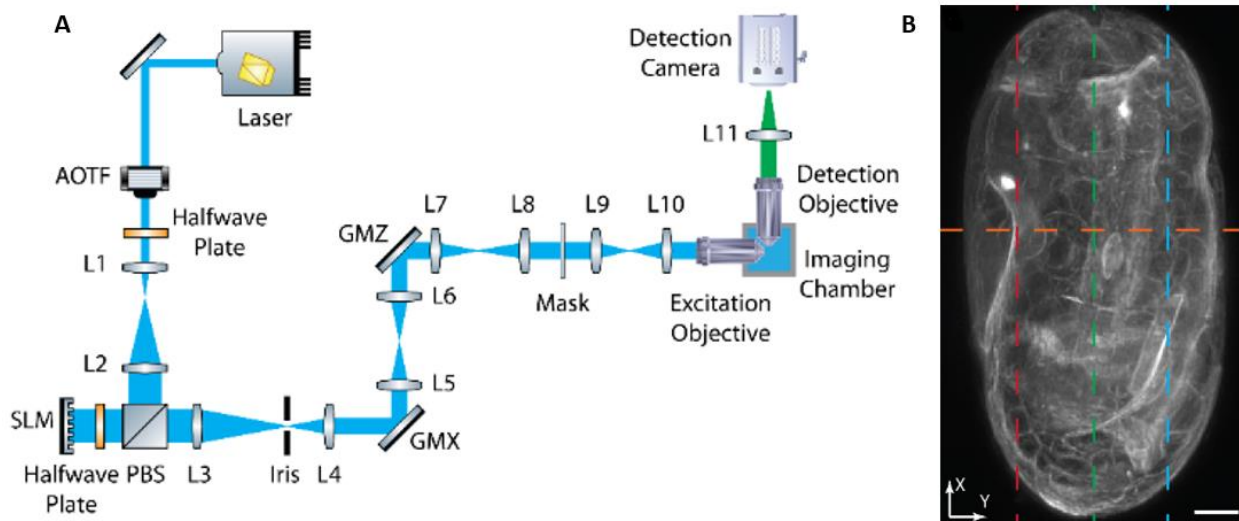


Figure 2-16 Experimental setup and the representative image acquired A) Schematic of the experimental system B) Using the suggested technique, a 3D visualization of a *C. elegans* embryo at a three-stage development has been captured by SPIM [66]. © 2015 Optica Publishing Group.

A customized LSFM device was developed by Riecker *et al.* [6] to observe the dynamics of proteins in adult *C. elegans*. The system was configured to take high-speed time laps images of adult *C. elegans* during ageing with minimal photobleaching. The imaging platform contains two complex illumination and detection arms, an indexed-match stage that enables the mobility and spinning of immobilized *C. elegans* and other components, as shown in Figure 2-17A and B. Various volumetric reconstructions of an adult *C. elegans* expressing GFP in its body wall muscles are shown in Figure 2-17C.

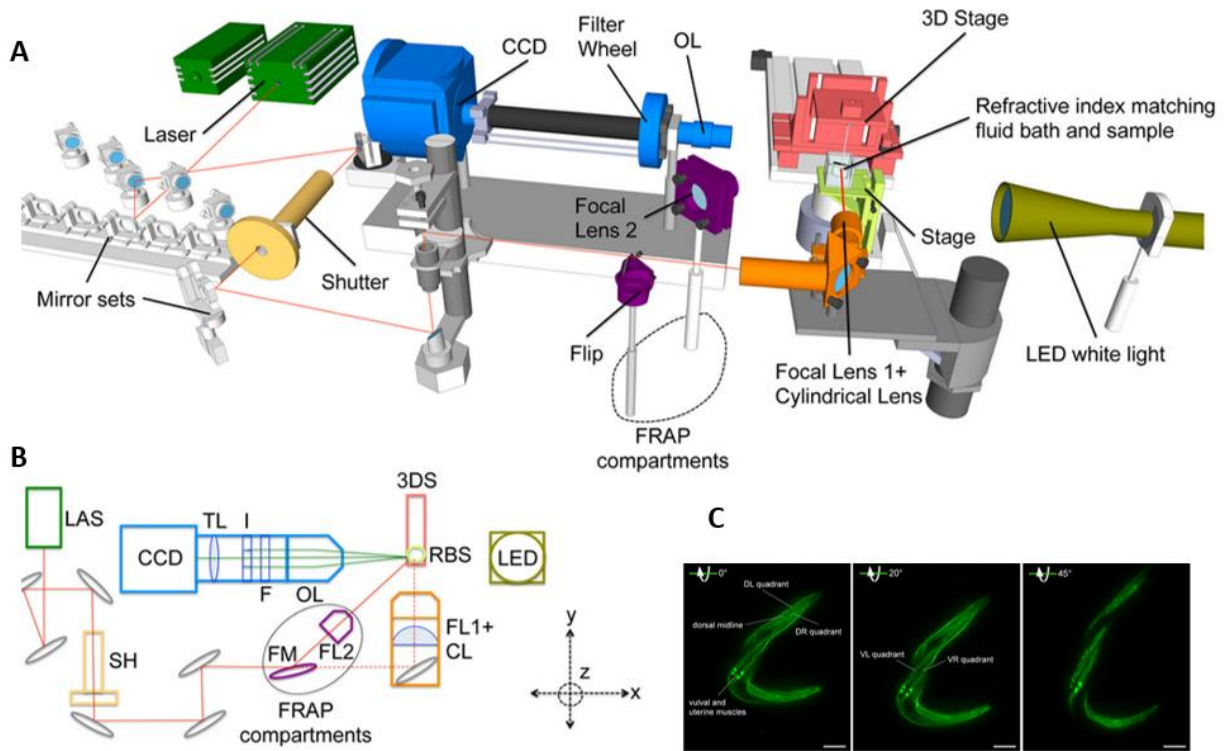


Figure 2-17 Experimental setup schematic and representative volumetric images of *C. elegans*. A) presents a three-dimensional illustration of the LSM system and its constituent parts. The path of the laser beam is depicted in red, which is directed via a flexible mirror and focused onto the sample using a cylindrical lens that generates a laser light sheet. The sample is immersed in an index-matching fluid bath and positioned in 3D space through an x, y, z-axis movable stage, allowing imaging with a CCD camera and tube lens attachment that is orthogonal to the light sheet (B) Basic two-dimensional scheme of the system's fundamental components. C) Representative images of an organism expressing muscle-specific GFP collected at various angles (0°, 20°, and 45°). (pmyo-3GFP). The photos show that there are muscular structures in the ventral-left (VL), ventral-right (VR), and dorsal-left (DL) areas. The scale bars that are shown in the images are 100  $\mu\text{m}$  [6]. Images are used under a Creative Commons Attribution 4.0 International (CCBY) License.

A modified version of SPIM with a high-NA detection goal was created by Krugten *et al.* [67] for live 3D imaging of young adult *C. elegans*. A tailor-made sample controller held the immobilized *C. elegans* before being immersed in an agar-based solution. A cylindrical lens is placed in the illumination direction to produce a 2  $\mu\text{m}$ -thick light sheet, as illustrated in Figure 2-18A. Data were collected using a 0.6 NA water immersion objective. Due to the platform's ability to eliminate out-of-focus light, Figure 2-18B, C shows that it enhanced picture quality in comprehensive brain imaging of *C. elegans* contrasted with epi-fluorescence microscopy.

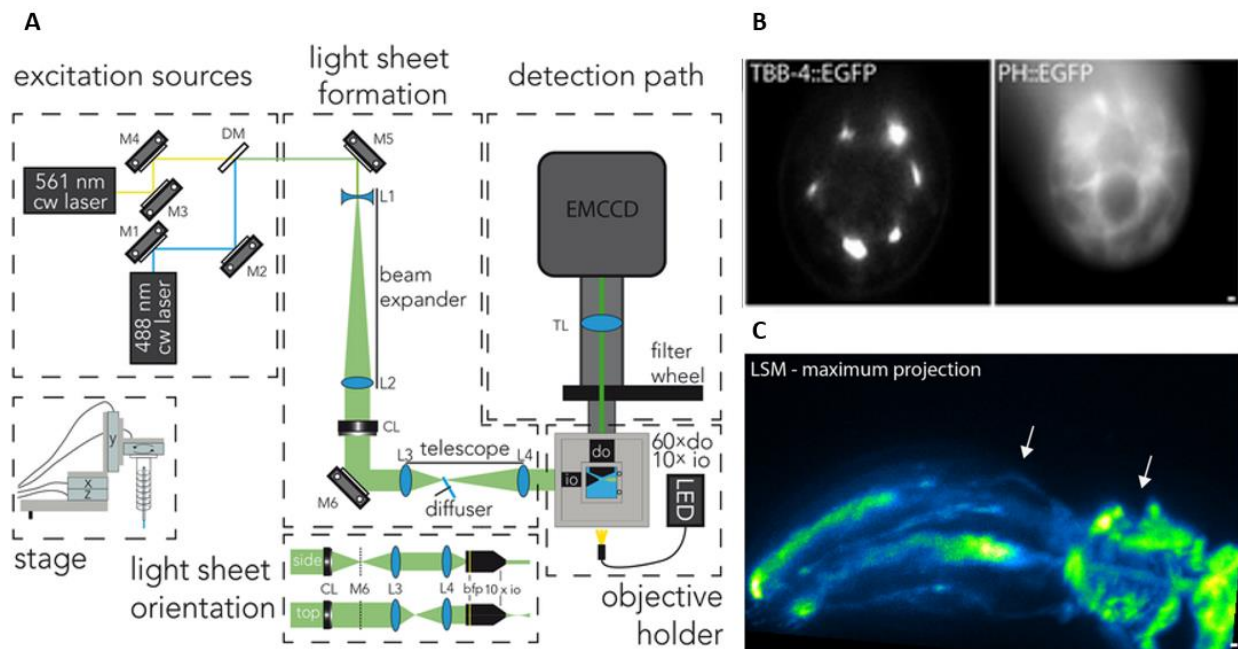


Figure 2-18 Schematic of the experimental setup and representative of collected images A) The diagram depicting the light-sheet microscope is exhibited. B) A cross-sectional view is provided to showcase the worms that express TBB-4::EGFP and PH::GFP. C) A maximum projection of 115 slices, each measuring  $0.75 \mu\text{m}$ , is utilized to demonstrate the head region of *C. elegans* expressing TBB-4::EGFP from anterior to posterior [67]. Images are used under a Creative Commons Attribution 4.0 International (CCBY) License.

The aforementioned platforms provide diverse approaches to attain high-resolution imaging of biological specimens. However, their elevated expenses and restricted throughput can render them inaccessible to several biological laboratories. In the upcoming section, we will investigate alternative measures to accomplish high throughput light sheet imaging in a comprehensive manner.

### 2.5.8 High throughput Light Sheet Imaging of *C. elegans*

As outlined in section 2.5.3, the manipulation of samples presents a critical bottleneck in enhancing the throughput of light sheet platforms. Conventional light sheet systems require the individual placement of samples between glass slides. The recent progress in the integration of microfluidics technology with light sheet fluorescence microscopy has provided unprecedented opportunities for the comprehensive analysis and efficient investigation of disease models in *C. elegans*, enabling high-throughput screening and extensive characterization of various disease-related parameters [68], [69].

In early attempts, the lack of throughput was still tangible. For instance, McGorty *et al.* [5] developed the open-top SPIM, a standalone platform with all the optical hardware positioned beneath the sample stage, as shown in Figure 2-19A. The open-top SPIM has a constant 6- $\mu\text{m}$ -thick light sheet for the sample to travel through using motorized mechanical parts. The most distinguishing feature of the setup is a water prism that corrects the aberrations brought on by imaging through a 45-degree cover glass. In order to highlight the diverse applications of their platform, they employed multiple configurations and model organisms. They employed conventional mounting techniques for *C. elegans* and utilized microfluidics sample mounting in conjunction with *Drosophila* to effectively demonstrate the seamless integration of their microscope into existing high-throughput workflows.

Figure 2-19B depicts a volumetric picture of an adult *C. elegans* that has been fluorescently labelled in PVD neurons. They demonstrated their platform's resolution by imaging a single *C. elegans* confined between a glass slide and coverslip. Subsequently, they transitioned to *Drosophila* to illustrate their throughput capabilities. They managed to acquire a volumetric image of a data set of 32 *Drosophila* embryos in as short as 2.3 minutes, with the stage scanned at a speed of 100  $\mu\text{m}/\text{sec}$  and a 100-frame rate, thanks to the arena-shaped microfluidics chips.

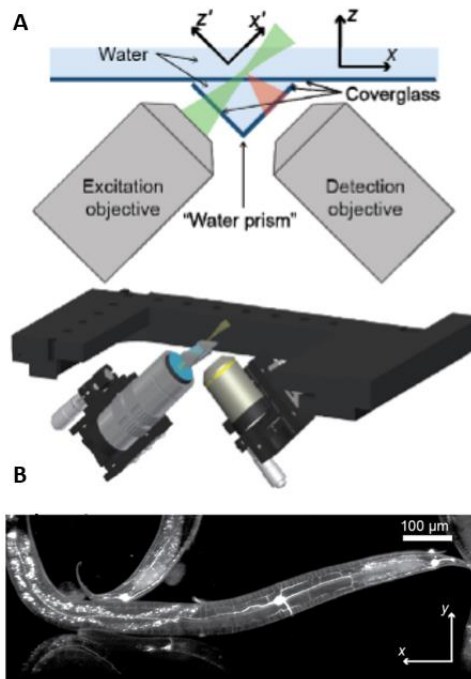


Figure 2-19 The first generation of high throughput experimental setup, along with the intricately acquired volumetric image. A) A diagram is presented depicting an open-top Selective Plane Illumination Microscopy (SPIM) setup, where two objectives are

positioned below the sample stage. Additionally, a three-dimensional representation of the microscope is included below the two-dimensional drawing. B) The data displayed represents a z-projection [5]. © 2015 Optica Publishing Group.

Another work showing a promising result is the work of Rasmi *et al.* [12], who combined light sheet microscopy and microfluidics. Figure 2-20A illustrates the system equipment, including two orthogonal illumination and detection arms and a microfluidics device for flow-based translation of worms through the fixed 4.5  $\mu\text{m}$ -thick light sheet. By continuously imaging the worms, there is no reason to immobilize worms upfront, and the device's throughput is higher than the conventional methods. The authors did not disclose the throughput. However, they did provide information on various aspects of the device, including the practical minimum exposure time (specified as 400 $\mu\text{s}$ ) and a corresponding frame rate of 565 frames per second (achieved at a reduced frame size) for a field of view (FOV) measuring 500 $\times$ 400 pixels. The system was configured to collect consecutive frames with a 35 $\mu\text{m}$  distance of a worm moving at a 6  $\mu\text{m}/\text{min}$  flow rate to collect 60 frames from each worm in total, as depicted in Figure 2-20B.

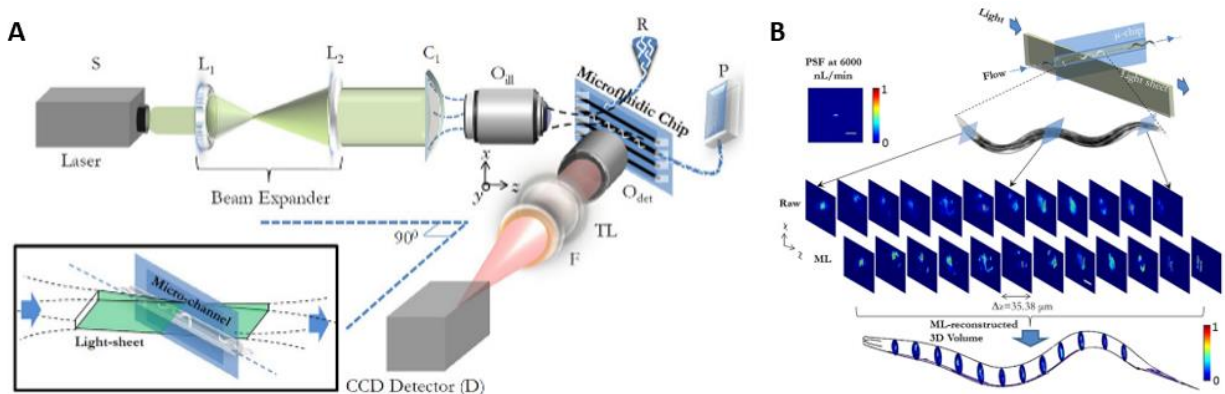


Figure 2-20 Next generation of high throughput light sheet platforms experimental setup schematics. A) A diagram illustrates the flow imaging system utilized in the study. The system employs light-sheet illumination, orthogonal detection, and a microfluidic imaging platform. A magnified image is provided as an inset, showcasing the light sheet entering the microfluidic channel. B) A schematic diagram portrays the intersection of the light sheet with the channel. The 2D cross-sectional images in raw and ML reconstructed form are presented in two rows. The PSF employed for the ML reconstruction is displayed in the upper left corner of the image. [12] Images were used with permission from AIP Publishing.

Martin *et al.* [70] also developed a complex SPIM, line excitation array detection (LEAD) fluorescence microscopy, for 3D high-speed flow cytometry of *C. elegans*. LEAD is an intricate optical system containing an illumination arm for generating a virtual 3- $\mu\text{m}$  light sheet, a detection arm with a photomultiplier array (PMT), and a speed detection arm to measure the speed as worms pass through the light sheet (Figure 2-21A). The proposed system could acquire 800k frames per second of a worm moving at 1 m/s speed through a microfluidic channel. A comprehensive image of the polyglutamine aggregation model *C. elegans* in  $\sim 1\text{ms}$  per animal demonstrated the system's

high-speed functionality, as shown in Figure 2-21B. The performance of LEAD is invincible, and no other high-content platform can resemble its throughput to date. It is worth noting that the limited number of pixels in the x-y plane significantly limits the lateral resolution. Furthermore, a drawback of any sophisticated setup is its initial cost, preventing it from becoming widespread. To address this issue, other studies have focused on making the light sheet platforms more affordable and compact.

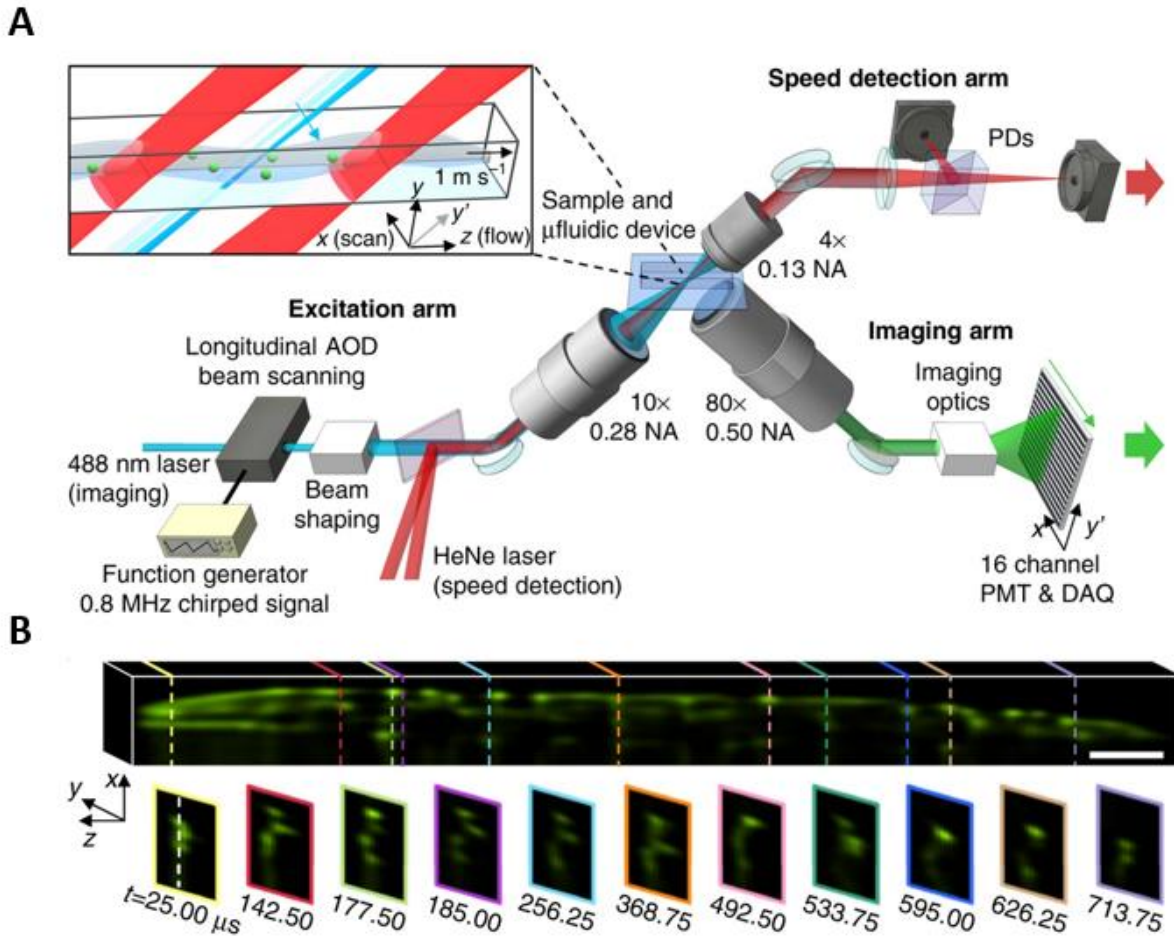


Figure 2-21 Overview of a high-speed fluorescence microscopy system, called Line Excitation Array Detection (LEAD), used as a 3D whole-animal flow cytometer. A) The system includes a schematic of the imaging system, which employs a longitudinal TeO<sub>2</sub> acousto-optic deflector (AOD) with a chirped frequency to scan a laser excitation beam across an angled plane on the sample. The excited plane is then imaged onto a photomultiplier tube (PMT) array, which captures a full frame of each scan cycle. In addition, a microfluidic device is employed to deliver populations of hundreds of *C. elegans*. Two light sheets generated by a HeNe laser and two photodiodes (PDs) are used to detect the velocity of the animals as they move through the imaging region. B) The volumetric image is composed of 631 x-y frames, each 66 x 14 pixels in size and captured every 1.25 microseconds. The image includes a scale bar of 50 micrometres [70]. Images are used under a Creative Commons Attribution 4.0 International (CCBY) License.

### 2.5.9 Compact Light Sheet Microscopy

Introducing a compact and affordable alternative, a low-cost light sheet microscopy platform, opens new possibilities for researchers seeking efficient and cost-effective imaging solutions. For instance, Hsieh *et al.* [10] developed an affordable LSFM platform using the volume holographic optical element (VHLSFM) as an alternative for the complex illumination optics of LSFM, as illustrated in Figure 2-22A. VHLSFM's performance was validated by imaging the oocytes inside the immobilized *C. elegans* and comparing them to the same cross-sectional images acquired with the epi-fluorescence microscope. The proposed system enabled resolving finer details inside the nematode compared to WF, as seen in Figure 2-22B. The light sheet quality was the same as conventional LSFM systems.

Figure 2-22C shows another affordable platform developed by Zhao *et al.* [9], who developed a light sheet add-on to a WF inverted microscope. A fibre-coupled laser is focused with a cylindrical lens and coincides with the focal plane of the inverted microscope's objective. This platform was employed for continuous volumetric imaging of *C. elegans* larvae, expressing GCaMP in its body wall muscles, as shown in Figure 2-22D. Variations in the fluorescence tagged to the muscles were further quantified by analyzing the GcaMP6 intensity. This plugin associated the sub-voxel-resolving algorithm with a 10-fold resolution enhancement compared to the host inverted microscope. However, mechanical translational components for the sample alignment and scanning hinder their application for high-throughput and large-scale studies.

In another attempt, an affordable light sheet add-on to a WF inverted microscope was developed by our laboratory. We introduced a low-cost, high-resolution light sheet add-on for monitoring the neural activity of pan-neuronal and DA-labelled adult worms [13]. The affordability of the platform was ensured by incorporating an excitation add-on arm on a WF microscope, as well as microfluidic chips instead of robotic systems for sample handling, as seen in Figure 2-22F. Instrumental limitations prevented the platform from reliably imaging the continuous flow of worms.

Essentially, the reviewed LSFM platforms for *C. elegans* demand either dedicated/costly light sheet instruments or sample immobilization in gel-based media, which is not suitable for large-scale, high-content, high-throughput studies.

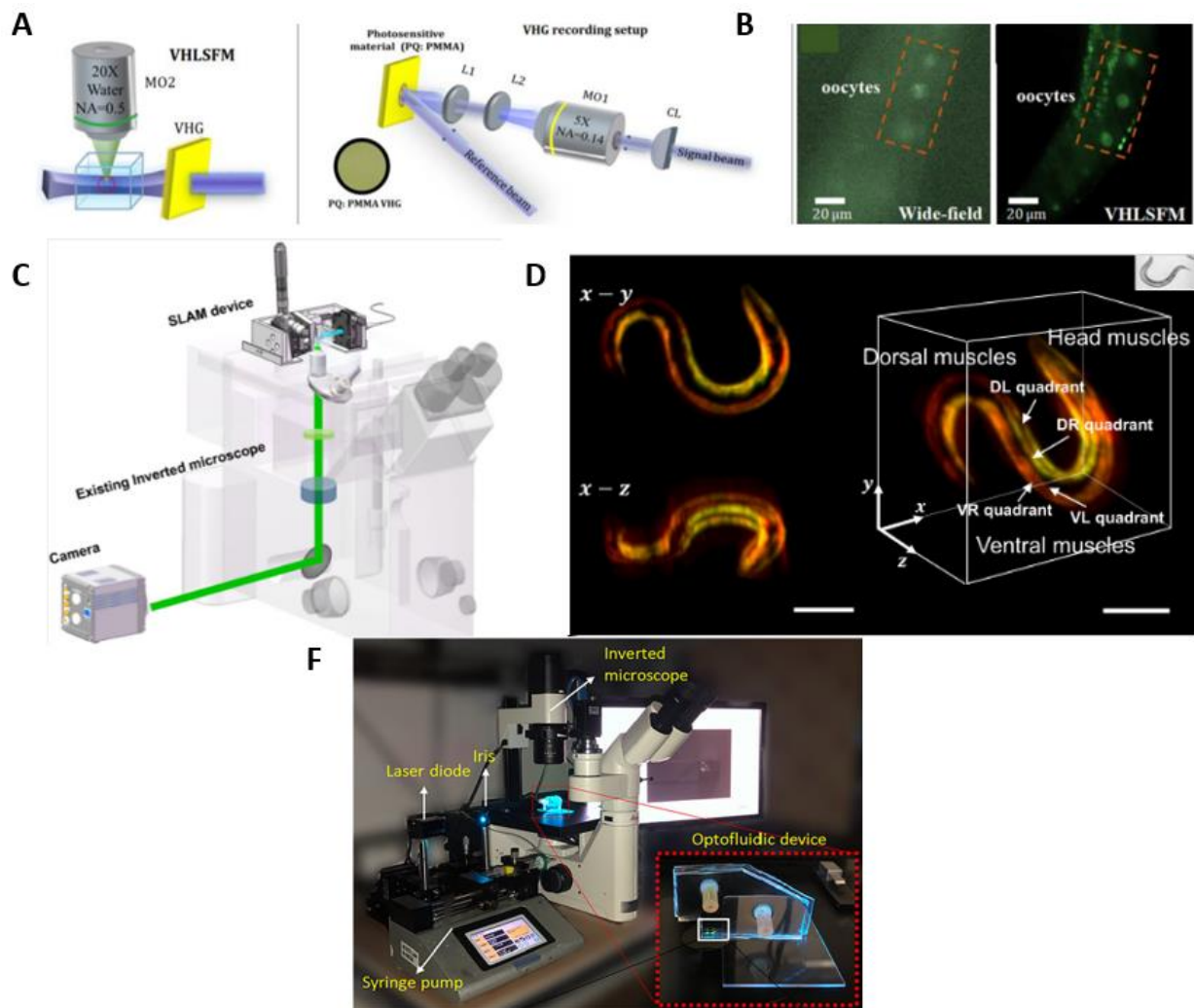


Figure 2-22 Low-cost and compact LFSM platforms A) VHLFSM (Volumetric High-Speed Light-Sheet Fluorescence Microscopy) system, with various components and add-ons that enable high-speed imaging and volumetric data acquisition. A schematic is presented, depicting the VHLFSM system. The VHG (Volume Holographic Grating) setup consists of an objective lens (MO1), relay lens (L), and cylindrical lens (CL). B) Images of oocytes inside *C. elegans* are shown, acquired using the VHLFSM (right) and a WF microscope (left) [10]. © 2020 Optica Publishing Group. C) Schematic of an add-on device, which is composed of multiple compact mechanical components and optical elements. D) Volumetric images of muscular activities of behaving *C. elegans* larva [9]. Images were used with permission from John Wiley and Sons. F) The experimental configuration comprised a low-cost laser diode and an iris, both situated in a free-space setup, which together generated the input excitation beam for the optofluidic device. The optofluidic add-on device, located on top of the inverted WF fluorescent microscope, is depicted in the inset of (a) [13]. This image is used under a Creative Commons CC BY License.

## 2.6 Research Gaps

Here, we discuss a few of the existing *C. elegans* light sheet imaging platforms to compare the performance metrics of our low-cost light sheet add-on device with the other reported systems. Inverted SPIM (iSPIM) (Figure 2-14), a high-speed (one volume every two seconds) imaging approach, was suggested by Wu *et al.* [7], which allowed the exploration of dynamic

neurodevelopmental processes in *C. elegans* that were previously inaccessible due to the phototoxicity and poor imaging speed of conventional imaging methods. Yet the conventional sample mounting restricted the platform's throughput to one worm imaging at a time.

Addressing that limitation, McGorty *et al.* developed the open-top SPIM [5]. It was utilized in multiple imaging applications, including the Histon's disease model *C. elegans* with PVD sensory neurons and nuclei in the intestinal cells and *Drosophila* embryos, as depicted in Figure 2-19B. Although the *C. elegans* images were acquired via the conventional sample mounting, they demonstrated their platform compatibility with a high throughput workflow via a microfluidic chip. The motorized stage scanned through 32 *Drosophila* embryos trapped in a straight microchannel for as short as 2.3 minutes, with a 100  $\mu\text{m}/\text{sec}$  scanning speed and a 100-frame rate.

The Ben-Yakar group shifted their high throughput imaging of *C. elegans* from a large-scale microfluidic chip in 96-well format to the line excitation array detection (LEAD) fluorescence microscopy to increase their throughput by 50 times [70]–[72]. LEAD was a complex SPIM for 3D high-speed flow cytometry of *C. elegans*. It could acquire 800k frames per second of a worm moving at 1 m/s speed through a microfluidic channel. Figure 2-21B illustrates a comprehensive image of polyglutamine aggregation model *C. elegans* in  $\sim 1\text{ms}$  per animal, demonstrating the system's high-speed functionality. It is an intricate optical system containing an illumination arm for generating a virtual 3- $\mu\text{m}$  light sheet, a detection arm with a photomultiplier array (PMT), and a speed detection arm to measure the speed as worms pass through the light sheet. Its' imaging speed is invincible, and no other high-content platform can resemble its throughput to date.

A drawback of any sophisticated setup is its initial cost, preventing it from becoming widespread. To address this issue, other studies have focused on making the light sheet platforms more affordable and compact.

In our initial low-cost work [13], we demonstrated the capability to image entire worms; however, the system had limitations. It was unable to image worm populations continuously, lacked adaptability to capture worms at different developmental stages, and lacked imaging consistency to enable quantitative fluorescent expression studies.

The main objective is to increase the throughput of Behrouzi's study [13] (Figure 2-22F) while keeping the cost of fabrication similar. We utilize a similar cost-effective method for the

fabrication of our light-sheet optofluidic system. The optimized system incorporates an optofluidic chip that features an embedded lens and a channel size designed for light sheet generation and the partial immobilization of nematodes. This system is tailored for continuous imaging of *C. elegans* and is complemented by a high frame rate sCMOS camera, as well as a pressure-based flow delivery sub-system. The performance of the optimized system is validated via continuous flow-based imaging of NW1229 populations. The reliability of the system is demonstrated through the analysis of 6-OHDA and  $MnCl_2$ -treated NW1229. Further, two different microfluidic designs with different channel sizes were fabricated and used for imaging different *C. elegans* strains in different stages of development (i.e., ERS100 and NW1229 at both L3 and YA). The proposed system facilitated the in-depth analysis of protein aggregation of nematodes in different development stages, showing the adaptability of the proposed high-throughput system for imaging nematodes with different sizes. Qualitative and quantitative analysis of results demonstrates the effectiveness and versatility of the optimized, low-cost imaging platform in capturing the developmental dynamics and detecting protein expressions of PD model *C. elegans* with high temporal resolution.

## **2.7 Thesis Objectives**

The pursued objectives listed below focused on addressing the cost, throughput, continuous monitoring, and worm age limitations of the abovementioned light sheet microscopy technologies, especially the one developed recently in our lab (Figure 2-22F).

1. Optimization of an affordable add-on optofluidic device to perform continuous light sheet imaging of young adult (YA) worm populations.
2. Expansion of technology to image population of an earlier stage of development (L3) continuously.
3. Utilization of advanced technology for the qualitative and quantitative investigation of protein aggregation and neurodegeneration in *C. elegans*.

### **3 Chapter Three: Methodologies**

The initial experimental setup shown in Figure 2-22F was a low-cost light sheet add-on that operated with conventional microscopes to solve the technical complexity and cost of conventional light sheet systems while making the imaging system accessible to researchers. We used an optofluidic chip with a low-cost PDMS-integrated lens for light sheet formation with lateral and axial resolutions of 1.1  $\mu\text{m}$  and 2.4  $\mu\text{m}$  full-width at half-maximum (FWHM), respectively [13]. While in this preliminary work, we showed the ability to image an entire worm, the system suffered from key limitations such as the ability to continuously image worms' populations, image worms at different developmental stages, and produce consistent image datasets enabling quantitative fluorescent expression studies.

This chapter presents a comprehensive overview of the current experimental setup, optofluidic chip specification, optical characterization, and fabrication process. The fabrication process of the chip is then described in detail. Moving on, the section reviews the methods utilized for worm preparation, the imaging procedure, and the chemical exposure recipe. Subsequently, it delves into the post-processing procedures applied to the collected data and elaborates on the statistical analysis methods used to interpret the experimental results.

#### **3.1 Experimental Setup**

Figure 3-1A illustrates the experimental configuration of the cost-effective yet high-throughput light sheet imaging platform designed for this thesis. This system consists of three primary sub-systems: a flow delivery system, an image acquisition system, and an optofluidic chip. The first two components are described below, and the optofluidic device is discussed in the next section.

The flow delivery system includes a pressure-driven pump (Flow EZ, Fluigent, France) and a microfluidic flow sensor (FLOW UNIT, Fluigent, France). The pressure pump's encapsulated inlet reservoir facilitates the uninterrupted injection of worms, irrespective of their relative size, without clogging. The flow sensor enables the platform to adapt to slight variations in worm size by controlling the pressure and flow rate within the optofluidic chip. Additionally, the pressure-driven flow delivery system can supply a continuous stream of worms without

bubbles, contamination, or requiring device refocusing, as opposed to the previously-used flow-driven approaches (syringe pump).

The image acquisition system starts with a low-cost, free-space laser diode source ( $\lambda$ : 488 nm, 3 mW, OXlasers A-B60F, China). While our platform allows for the excitation of samples at a broad spectrum of wavelengths, a 488nm excitation wavelength was selected to accommodate the excitation of a wide range of fluorophores, such as the GFP targeted in studies of this work. To obtain optimal imaging performance, the light sheet thickness must be tuned to closely match the diameter of *C. elegans* neurons. To achieve this, we employed OpticStudio Zemax simulations to define the optical specifications of our chip. An iris is utilized to ensure the illumination beam size complies with the input laser size determined by Zemax simulation. The laser and the iris are mounted in a customized 3D-printed fixture, and the entire assembly is fixed to an optical post attached to a set of linear translation stages, as shown in Figure 3-1B. The 3 degrees of freedom offered by the translation stages are used to align the collimated laser beam with the integrated cylindrical lens to generate a uniform cross-sectional light sheet in the device channel. The emitted light sheet illuminates the neurons of the animals, and this illumination is captured by a high frame rate sCMOS camera (Edge 5.5, PCO, Germany). This particular sCMOS camera can accommodate a frame rate of ~900 frames per second (FPS) within the region of interest. Furthermore, it

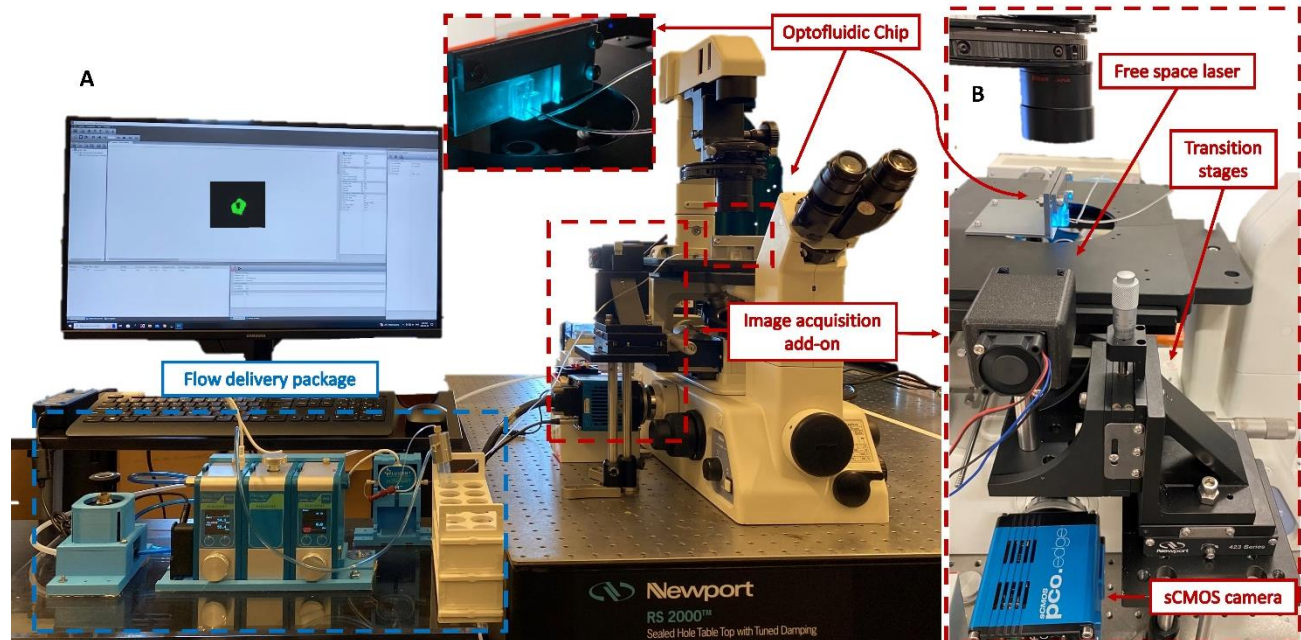


Figure 3-1 Experimental setup. A) The front view of the experimental setup contains the image acquisition add-on, flow delivery package and the optofluidic chip. B) Side view of the experimental setup, including a free-space and low-cost laser source and an iris that was used to generate the input excitation beam of the optofluidic device. The optofluidic add-on device is placed on the inverted WD fluorescent microscope. The generated light sheet replaced the epi-illumination of the host microscope. The emitted fluorescent was collected by the native objective lens of the microscope and recorded using an sCMOS camera.

maintains a high detection sensitivity, enabling the acquisition of weak fluorescent expressions from the sample.

### 3.1.1 Optofluidic Add-on Device

The optofluidic chip has a U-shape design (Figure 3-2A) and is comprised of three main components: 1) inlet and outlet reservoirs (Figure 3-2B) for introducing the worms suspended in M9 buffer into the device and their removal after imaging; 2) a microchannel with a 90-degree bend to facilitate cross-sectional light sheet excitation and collection of the fluorescence emissions of the worms via the microscope's native objective lens (Plan Fluor 10X/0.3NA; TE300 Inverted Fluorescence Microscope, Nikon, Japan) with minimal light interactions with the device (Figure 3-2C); and 3) an integrated PDMS microlens specifically designed and optimized (via OpticStudio Zemax software) to focus the collimated excitation laser beam into a 2.3  $\mu\text{m}$  thick light sheet at the center of the microchannel and just above the channel bend, as illustrated in Figure 3-2C. A gradual reduction of the microchannel width allows the train of worms to be slowed while limiting their lateral motion as they continuously pass through the light sheet. Given that ERS100 PD model worms display phenotypes after the L2 stage, two similar device designs are employed, one with

a 50  $\mu\text{m}$  wide microchannel at the light sheet to image YA worms and another with a 30  $\mu\text{m}$  necking region to image L3 *C. elegans* (Figure 3-2C).

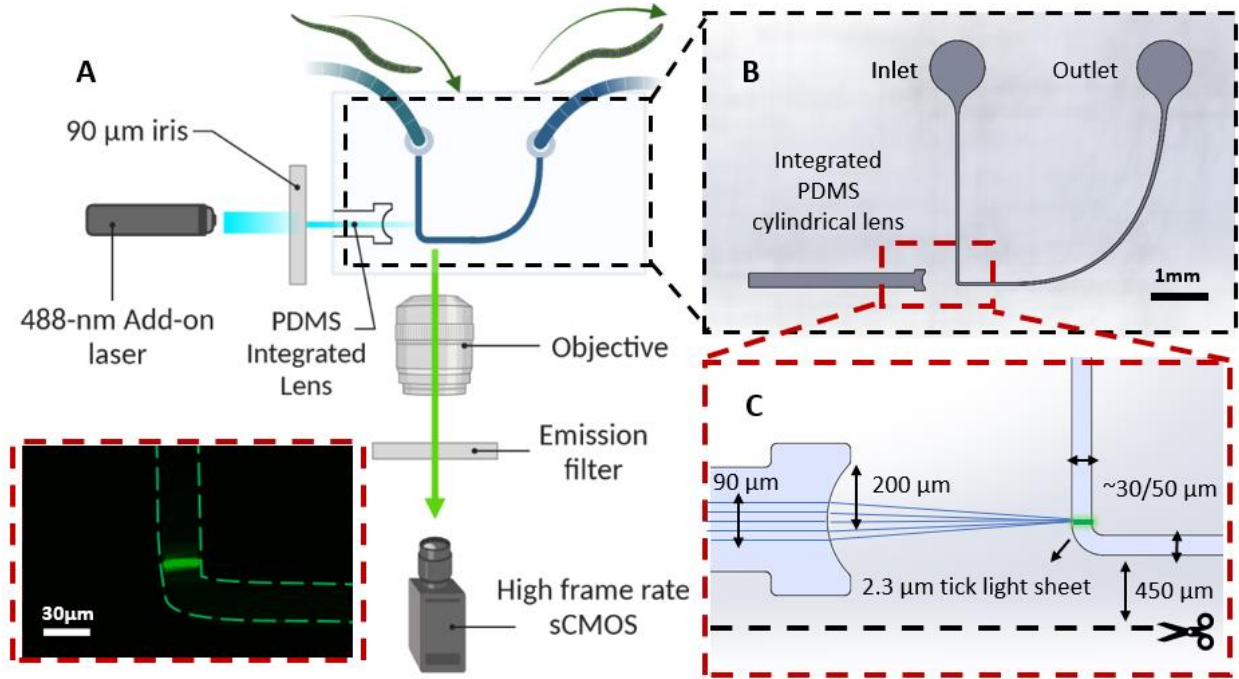


Figure 3-2 Schematics of the mechanical and optical design of the optofluidic chip. A) Schematic of excitation (blue) and emission (green) beams with respect to host microscope objective lens, high frame rate camera and the optofluidic chip. The front view of the actual light sheet at the bend in the darkfield is displayed within the inset of Figure (A). (Created with BioRender.com) B) Schematic of the front view of the chip's design displaying the inlet and outlet with respect to the PDMS-integrated micro lens. C) Zoom view of the bend illustrating dimensions of microchannels for L3 and YA stages and radius of the micro lens in addition to the light sheet thickness and beam diameter.

Silicon (Si) wafers with 4 inches diameter and a 500-550  $\mu\text{m}$  thickness were purchased from Wafer World Inc., USA, to create the devices. Although the designs are identical, there are differences in the channel dimensions for imaging L3 and YA worms, which require using different SU-8 photoresists (MicroChem Corporation, USA) and recipes. First, the SU-8 photoresist layer is spin-coated onto the Si substrate. In the case of the device for imaging L3 worms, a layer of  $\sim 30$   $\mu\text{m}$  thick SU-8 2035 is applied via spin coating. Conversely, a layer of SU-8 2075 with a thickness of  $\sim 50$   $\mu\text{m}$  for the YA imaging device is spin-coated. This layer is then baked to remove any residual solvents and to improve adhesion to the substrate. Next, a photomask containing our pattern is aligned to the substrate and the photoresist layer is exposed to UV light through the mask. The exposed photoresist is then baked again before the development step. The development process selectively removes the unexposed regions and reveals the underlying substrate. Finally, the substrate goes through the hard bake one last time to ensure that the SU-8 properties do not change.

Figure 3-3 illustrates to replicate PDMS devices, the PDMS elastomer base and curing agents (Dow Corning, USA) are mixed at a 10:1 ratio, degasified, and poured onto Si-SU8 master moulds. After curing for 2 hours at 80°C, the cured PDMS layer is de-moulded, and through-holes are punched using a 0.5 mm diameter biopsy punch for inlet and outlet holes (WellTech). Next, the devices are cut and bonded to flat PDMS layers using oxygen plasma (PDC-001-HP Harrick Plasma, USA) at 870 mTorr pressure and 30W for 40 seconds. The bonded layers are then heated for 15 minutes at 70°C to enhance bonding.

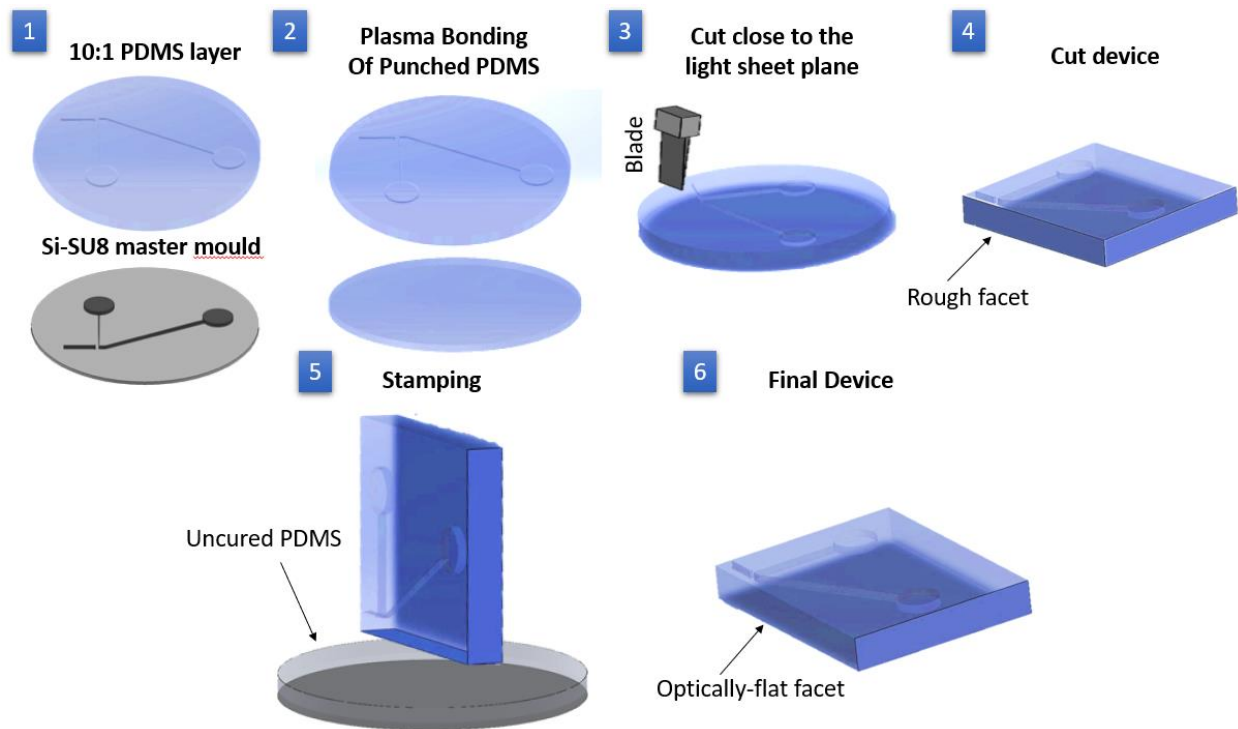


Figure 3-3 Fabrication process of optofluidic devices. (1) Design pattern transferred to PDMS layer by curing on silicon mould and peeling off. (2) A patterned PDMS layer is bonded to a flat PDMS layer via oxygen plasma treatment to seal microfluidic channels. (3) The device was cut close to the light-sheet plane to collect emission fluorescence from the side facet. (4) Additional step to create an optically flat facet: PDMS spin-coated on a glass slide, a device placed on top, and peeled off once cured (5-7) [73].

To enable light sheet imaging on an inverted microscope, the devices are cut close to the light sheet plane, leaving a 450  $\mu\text{m}$  thick PDMS wall between the light sheet plane and the edge of the device, as seen in Figure 3-2C and 3-3. However, the air-PDMS contact becomes rough after the devices are cut, which can deteriorate the quality of recorded images. To avoid this systematic issue, the devices are stamped sidewise onto thin PDMS prepolymer layers to optically smoothen the cut surfaces.

The light sheet thickness design of 2.3  $\mu\text{m}$  effectively enables the imaging of GFP biomarkers within the size range of  $\sim 5\text{-}10\ \mu\text{m}$  [74] in both L3 and YA worms. Achieving a 50  $\mu\text{m}$  wide light sheet with a 488 nm excitation wavelength necessitates a light sheet thickness of approximately 2.3  $\mu\text{m}$  (FWHM), as determined by the Gaussian beam optics of the YA (50  $\mu\text{m}$ ) device. (Equation 2-2) OpticStudio Zemax simulations determined that a 200- $\mu\text{m}$  radius of curvature of the PDMS cylindrical microlens can satisfy the required light sheet specifications from a Gaussian input beam with a diameter of about 90  $\mu\text{m}$ . The sole distinction within the 30  $\mu\text{m}$  configuration is the gap between the micro lens and the microchannel, which is once more optimized via the Zemax simulation. After the alignment, worms' cross-sectional light sheet images were continuously acquired via a monochrome high frame rate sCMOS camera.

### 3.2 Worm Preparation

All bacteria and worm maintenance procedures were performed under biosafety number 02-19 issued by York University's Biosafety Committee to PR. *C. elegans* strains that are used in this study are NW1229 [expressing green fluorescent protein (GFP) pan-neuronally; F25B3.3::GFP+dpy-20(+)] and ERS100 [a transgenic strain expressing green fluorescent protein (GFP) based reporter of human  $\alpha$ -Syn in DA neurons; dat-1p::mCherry; dat-1p::hSNCA::GFP(Venus)] [31]. These strains were acquired from the Caenorhabditis Genetics Center (USA, Saint Paul) and Eurac Research (Italy, Bolzano).

All chemicals were purchased from Sigma-Aldrich, USA. The conventional procedures listed in the Wormbook [75] were followed in preparing nematode growth medium (NGM) agar plates. All experiments were conducted on freshly produced NGM plates containing bacterial lawns and kept at room temperature (approximately 22  $^{\circ}\text{C}$ ) in a biological safety cabinet. The cabinet was pre-sterilized with UV light and cleaned with a 70% ethanol in water solution to avoid contamination.

A "lawn" of *Escherichia coli* (*E. coli*) strain OP50 was seeded onto the NGM plates at room temperature. To prepare the bacteria, a single *E. coli* OP50 colony from a source streak plate was added to LB-Broth media, and it was then cultivated overnight at 37  $^{\circ}\text{C}$  in a shaker incubator to produce the OP50 supply. Twenty-five grams of LB-Broth were combined with 1 litre of distilled water and autoclaved to create the LB-Broth medium. After centrifuging the inoculated enriched media to concentrate the bacterial culture, 200  $\mu\text{l}$  of the *E. coli* OP50 source was added to the

plates, which were then allowed to dry overnight. All experiments are conducted using YA and L3 worms that are well-fed and age-synchronized (48 and 24 hours). The standard alkaline hypochlorite treatment procedure was used to obtain synchronized worms [76]. The gravid worms were removed from the NGM plate using M9 buffer (3 g  $KH_2PO_4$ , 6 g  $Na_2HPO_4$ , 5 g  $NaCl$ , and 1 ml 1 M  $MgSO_4$  in 1 L distilled water) in a 15 ml Eppendorf tube. Then, they were treated for 10 minutes with a solution of 3.875 ml double-distilled water, 125  $\mu$ L 1 M NaOH, and 1 mL of sodium hypochlorite ~ 6%. The worm cuticle was removed during this procedure, while the worm eggs were unaffected. After the procedure, samples were centrifuged for a minute at 1500 rpm to sink eggs at the bottom for collection. The eggs were incubated overnight with M9 buffer and RotoFlex™ tube rotator (RK-04397-40, Cole-Parmer, Canada), producing L1 larvae. To conduct the test, hatched larvae are placed onto newly prepared NGM plates and allowed to grow until they reach the L3 and YA stages.

For neurodegeneration, 6-OHDA (636-00-0, Sigma-Aldrich), a known neurotoxin, was used by obtaining a 10 mM stock solution using 5 mg of 6-OHDA in 2 mL of autoclaved M9. 6-OHDA solution was prepared in a dark room and stored at  $-20$  °C. On the following day, the hatched larvae (L1 stage) were treated with 500  $\mu$ M of 6-OHDA (950  $\mu$ L M9 and 50  $\mu$ L 6-OHDA from our prepared 10 mM stock solution) in a dark room for 1 h.

To induce Manganism, a neurological disorder associated with prolonged exposure to manganese and characterized by symptomatic similarities with Parkinson's disease, we employed Manganese Chloride (7773-01-5, Sigma-Aldrich). A 20 mM stock solution was prepared using 12.5 mg of  $MnCl_2$  in 5 mL of autoclaved DI water to prevent precipitation in the M9 solution. Subsequently, on the following day, hatched larvae at the L1 stage were treated with 5 and 10 mM of  $MnCl_2$  (1 mL DI water and 1 mL  $MnCl_2$  from our prepared 20 mM and 10 mM stock solution) for a duration of 1 hour.

### **3.3 Imaging Procedure**

We introduce Rhodamine (Rhodamine 110 chloride, Sigma-Aldrich) into every fabricated chip and capture side-view images to confirm the fabricated lens's capability to achieve the intended light sheet thickness and width. Following this validation, we proceed to capture images using the

chip in its regular orientation to verify the precise alignment required for light sheet imaging. To do so, translation stages of the excitation sub-system are tuned to optimize the alignment of the collimated laser excitation beam with respect to the integrated PDMS lens while monitoring the uniformity and intensity of the light sheet fluorescent images recorded by the camera and inverted microscope.

Based on the Nyquist-Shannon sampling theorem, the image's spatial sampling rate should be at least twice as fine as the smallest detail that needs to be resolved. This criterion implies that to capture the details of the  $\sim 2\text{-}\mu\text{m}$  neurons in the direction of flow accurately and continuously, the axial sampling resolution of the imaging system should be at least 1 micron (i.e., half the size of the neuron). This means the flow rate needs to be adjusted for comprehensive imaging of entire worms such that at least  $\sim 750$  and  $\sim 1000$  frames are recorded from L3 and YA worms, respectively. To further enhance the throughput, under-sampling in the flow direction can be exercised. In our experience, the trade-off between axial sampling rate and throughput can be carefully optimized to ensure that under-sampling does not compromise the fidelity of the reconstructed images beyond an acceptable level. For worms studied in this work and for the size of the region of interest in our system ( $100\times 100$ ) *Pixel*<sup>2</sup>, with each pixel having a physical dimension of  $0.65\ \mu\text{m}$ ) we found that the worms can be reliably imaged in  $<0.5\text{s}$  while running the camera at 865 FPS and flowing the YA and L3 worms at rates of 5 and  $1.5\ \mu\text{l}/\text{min}$ , respectively.

For each experiment, all the age-synchronized worms are injected through one device under similar conditions to minimize the chances of systematic errors caused by day-to-day variations in the light intensity of the laser, which can jeopardize the validity of quantitative studies of neuronal expressions. A total of six experiments are performed to assess the throughput at various developmental stages. Specifically, three experiments are conducted for the L3 stage, and an additional three experiments are carried out for the YA stage, utilizing the aforementioned flow rates. These experiments evaluated the platform's throughput and determined the standard deviation at each respective stage.

### 3.4 Chemical Exposure

The 6-OHDA solution was prepared the day before the experiments by adding 11.8mg of 6-OHDA in powder form to 500 ml of M9 buffer. 6-OHDA powder was kept in a -20°C dark room. To expose the L1 synchronized worms to the solution, we add the desired amount of the 6-OHDA solution to the M9 buffer, including the worms, for an hour. Worms will be washed with M9 buffer after the exposure and will be centrifuged and seeded to plates with OP50 bacteria.

### 3.5 Post-Processing

Initially, a region of interest (ROI) of  $10^4$  pixels corresponding to an area of approximately  $65\mu\text{m}\times 65\mu\text{m}$  are cropped from the original image/slice sequence, as depicted in Figure 3-3A. The background is then subtracted by applying the built-in rolling-ball algorithm present in ImageJ (Figure 3-3B) [77].

Due to the continuous nature of worm imaging, an abundant amount of data is generated, which must be further processed to collect the relevant information. Figure 3-3C depicts that to extract the fluorescent-bearing frames, a thresholding algorithm was developed in MATLAB, which could eliminate blank frames from the 3D image datasets with a speed of  $503.41 \pm 95$  FPS.

Due to its biological significance, the nerve ring is a key point of interest among the frames containing signals in both transgenic worms. Six out of the eight DA neurons (anterior deirids and cephalic sensilla) are situated within the worms' heads, while a single pair is found in the posterior lateral position (PDE) [78], [79]. The anterior deirids (ADE) and cephalic sensilla (CEP) pairs exhibit lateral and dorsal entry routes to the nerve ring, respectively, thereby establishing it as a prominent site for conducting neurodegenerative studies [80].

An automatic labelling algorithm was developed to facilitate unbiased and accelerated identification of nerve ring images in datasets. The algorithm first reduced the dimensionality of the 3D image datasets by representing each image slice with a single value corresponding to slice/frame mean fluorescent intensity (MFI). (Figure 3-3D) By doing so, the 3D stack of slices was reduced to a 2D signal, as illustrated in Figure 3-3E. As the nerve ring exhibits the highest fluorescence expression throughout the worm's entire nervous system, MATLAB's signal

processing toolbox was utilized to identify the signal peak associated with a worm nerve ring. (Figure 3-3F) The start and end frames corresponding to the nerve ring region were estimated using the signal peak's Full Width at Half Maximum (FWHM). Finally, the mean intensity of the nerve ring (MINR) was defined and calculated as the average of MFI values corresponding to worms' nerve ring regions. The calculated MINR values were later used for statistical comparisons among the studied population groups.

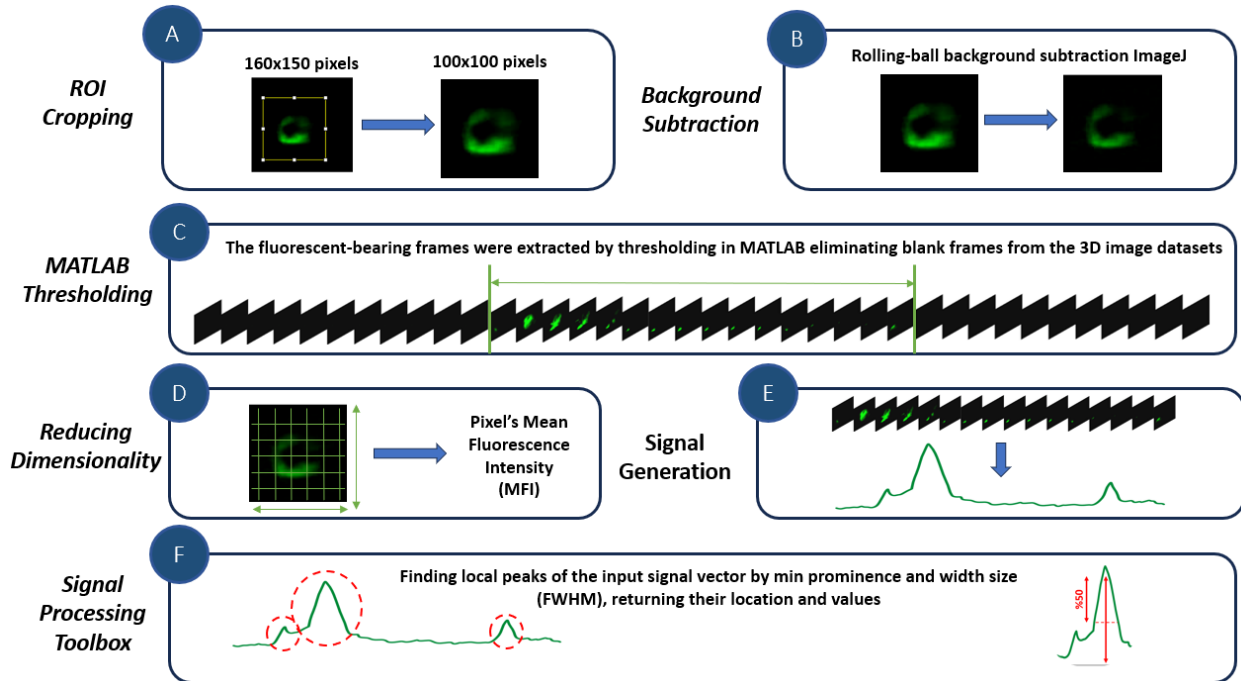


Figure 3-4 Flow chart illustrating the post-processing steps. A) Region of Interest (ROI) cropping, restricting the analysis to a 100×100 square area containing neural fluorescence expressions. B) Background subtraction performed using the built-in rolling ball algorithm in ImageJ. C) Extraction of fluorescence-bearing frames from the large dataset by applying MATLAB thresholding techniques. D) Dimensionality reduction of each frame from 2D to 1D using the Mean Fluorescence Intensity (MFI) approach. E) Conversion of the separated frames into signal format utilizing the MFIs. F) Utilization of MATLAB's signal processing toolbox to analyze fluorescence expressions, identify peak locations and determine peak values.

### 3.6 Statistical Analysis

All results are presented as mean  $\pm$  standard deviation (SD), while the differences between two populations are compared using a two-tailed Welch's t-test due to unequal variances. The assumption of unequal variances was assessed using an F-test. The groups are considered significantly different at a P-value less than 0.05. Furthermore, we employed the Brown-Forsythe one-way ANOVA to compare the control and exposed worms for three populations, given the presence of varying variances in the standard deviations across the three datasets. Subsequently,

to assess the means of the 5mM and 10mM datasets in comparison to the control dataset mean, we applied the Games-Howell post hoc test, a suitable choice for datasets with unequal variances, especially considering our sample size exceeding 50. Welch's t-test and Brown-Forsythe one-way ANOVA are performed using GraphPad Prism version 9.4.0 and graphically presented via estimation plots. We utilized the ROUT method with a 2% threshold for outlier removal. Additionally, we employed max scaling for normalization, which involved dividing the datasets by the maximum value of the control dataset.

## 4 Chapter Four: Results and Discussion

In this section, we elucidate the various modifications applied to the low-cost light sheet platform, which effectively facilitates high throughput and high-resolution imaging of YA *C. elegans*. The process begins with optical and experimental condition characterization, laying the groundwork for subsequent investigations. By advancing the platform's proficiency in imaging large populations of both YA and L3 panneural worms, it establishes a robust foundation for deploying the device in qualitative and quantitative studies concerning protein aggregation and 6-OHDA-induced neurodegeneration in this model organism. In addition, the low-cost and compact add-on module, as detailed in this study, is seamlessly integrated with a conventional fluorescent microscope. The incorporation of standard components commonly found in most laboratories, including an inverted microscope, camera, and pump, completes the setup. Notably, the system demands just two additional components—the low-cost laser diode sub-system and the optofluidic device—which, in total, incur a cost of less than one hundred USD. This cost-effective and efficient configuration simplifies accessibility and renders the platform highly practical for widespread implementation across diverse research environments.

### 4.1 External Components Modification

Light sheet resolution depends so much on the alignment of the illumination beam to the integrated lens inside the chip. Initially, it was time-consuming and vulnerable to the slightest movement with multiple degrees of freedom. It consisted of a glass fixture holding the chip perpendicular to the objective, taped to the microscope stage. Furthermore, the laser was aligned after the chip was mounted and taped on top of the objective. The laser was installed on optomechanical poles and transition stages, which enabled horizontal and vertical movements.

Subsequent to verifying the proper alignment and positioning of the light sheet, the next step involved introducing the worms into the imaging device. Initially, this was accomplished by disconnecting the tubing, introducing a small amount (4 microliters) of M9 buffer containing the worms, and reconnecting the tubing to the device inlet. However, this approach was associated with various challenges. Specifically, it frequently led to worms dripping out of the device, resulting in the loss of the specimens and necessitating the repetition of the procedure. Furthermore, this method carried a high risk of contamination during the injection process.

Additionally, it was susceptible to generating air bubbles within the tubing, which could compromise the functioning of the imaging platform, as seen in Figure 4-1.

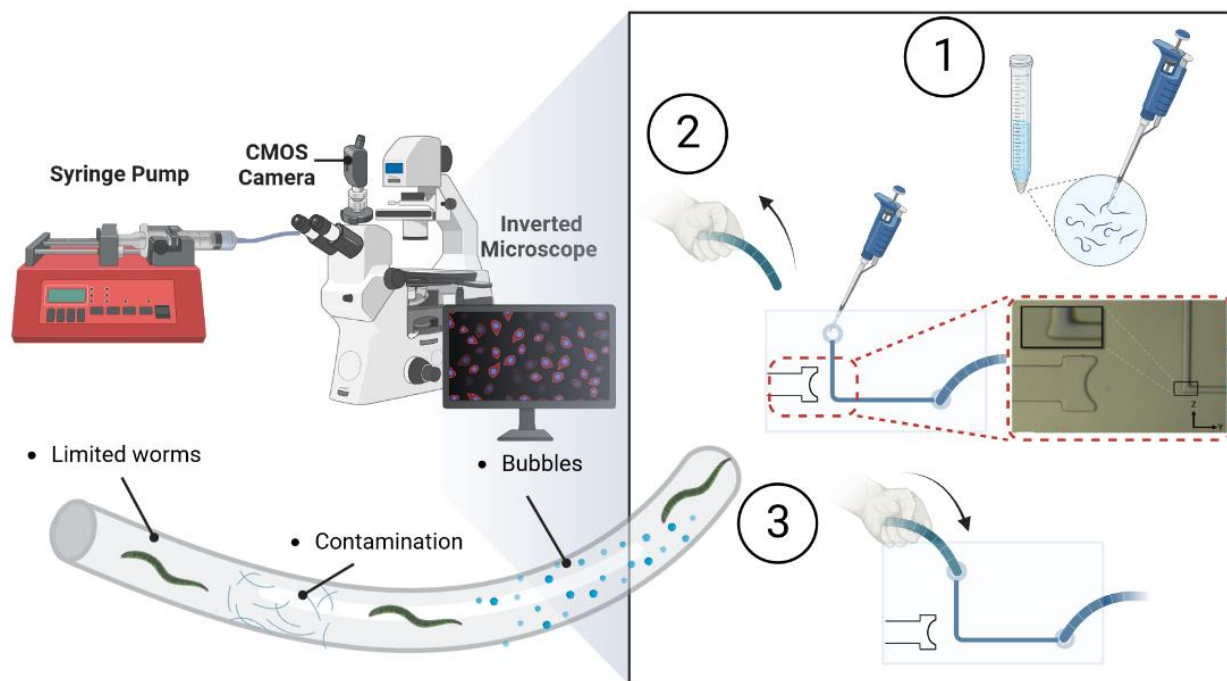


Figure 4-1 Schematic representation of challenges encountered during the process of loading worms into the imaging device. The current method of introducing worms through disconnected tubing leads to issues such as worm dripping and loss, contamination risk, and air bubble formation, potentially affecting imaging quality and data analysis. The Inset image displays the actual glass fixture.

To optimize the alignment procedure, we devised and implemented a pair of custom 3D-printed fixtures designed to conform to the dimensions of the existing microscope in the laboratory, as illustrated in Figure 4-2A. Figure 4-2B, C shows one of the fixtures was affixed to the side of the microscope stage to hold the laser and facilitate its movement in the x and y axes. The second fixture was linked to the transition stage of the microscope slide and was adjusted using the microscope adjustment stick. (Figure 4-2B, C) The implementation of this custom design yielded a substantial reduction in the alignment process duration, effectively mitigating the risk of microscope focus loss caused by minor movements. Moreover, the fabrication procedure was expedited significantly, as the previous requirement of individually gluing glasses to the chip or to each other for every experiment was entirely eliminated.

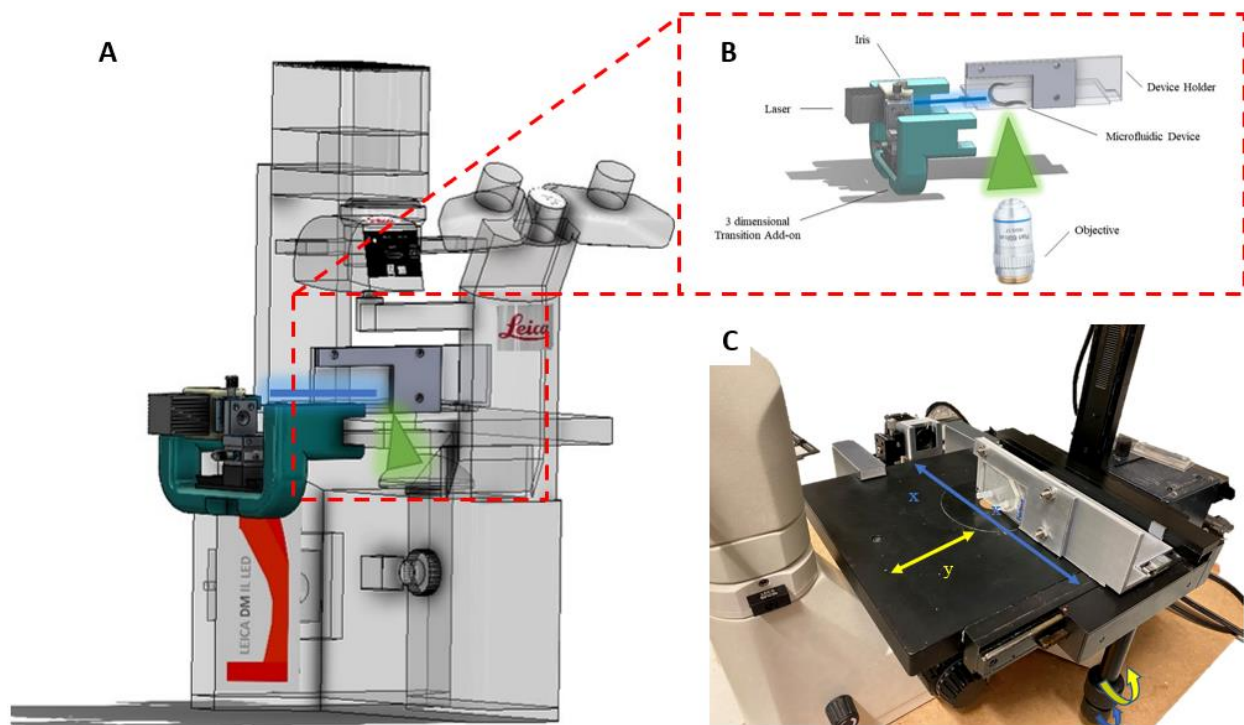


Figure 4-2 Schematic and real 3D printed fixture for alignment optimization A) Solidworks model displaying the inverted fluorescence microscope in the laboratory, featuring the attachment of two fixtures on the side and top of the microscope. B) A more detailed set of fixtures illuminates the optomechanical components and the laser on the side fixture, while the top fixture aids in precise alignment of the sample concerning the laser and the detection objective. C) Real image showcasing the implementation of the fixtures on the inverted microscope. The mounting of fixtures on the original transition stage facilitates smooth sample movement along the X and Y axes during the alignment process.

In response to the challenges encountered during the loading of worms into the imaging device, multiple attempts were made to find a viable solution. The initial stage involved a modification in the tubing system. It was noted that one of the primary reasons for the inconsistent transformation of worms was attributed to the tubing's diameter and material. In the previous study, as seen in Figure 4-3A, platinum-cured silicone tubing with an inner diameter (ID) of 1.6 mm was utilized.

Considering the sample diameter of  $\sim 50 \mu m$ , the utilization of a 1.6 mm diameter tubing left substantial space for the flow to bypass the worms, thereby facilitating worm resistance against the flow. This constituted the primary rationale behind the prior study's introduction of the worms by unplugging the inlet tubing rather than employing an upper-hand approach. The significant disparity in diameter between the tubing (1.6 mm) and the microchannel ( $50 \mu m$ ) necessitated distinctly disparate flow rates to enable the passage of the worms through the system. The rationale above directed us to use Tygon tubing with an inner diameter of 0.5 mm (Figure 4-3C).

An additional crucial consideration was the flexibility of the platinum-cured silicone tubings. In comparison to silicone-cured tubing, Tygon tubing exhibits lesser flexibility, which proves advantageous when dealing with clogging incidents within the platform. Clogging occurring at bends can lead to back pressure accumulation. The pliancy of the tubing allows it to compensate for this back pressure by expending the buildup pressure, thereby preventing it from reaching levels high enough to unclog the bend. Furthermore, the stiffness of the Tygon tubing proved beneficial in cases of clogging, as it offered stability and resilience. Additionally, handling the Tygon tubing did not cause fluctuations in the system flow, which contrasts with the behaviour observed when using silicone-cured tubings.

The ultimate advantage of implementing the new tubing was the reduction in chip size, resulting in decreased PDMS usage and contributing to the cost-effectiveness of the device, even during the prototyping phase. By carefully selecting the appropriate tubing, the tubing's inner diameter (ID) was minimized by approximately three times. Additionally, modifications were made to the inlet and outlet designs of the chip to accommodate the new tubings, which consequently led to the creation of a smaller chip, as depicted in Figure 4-3B and D.

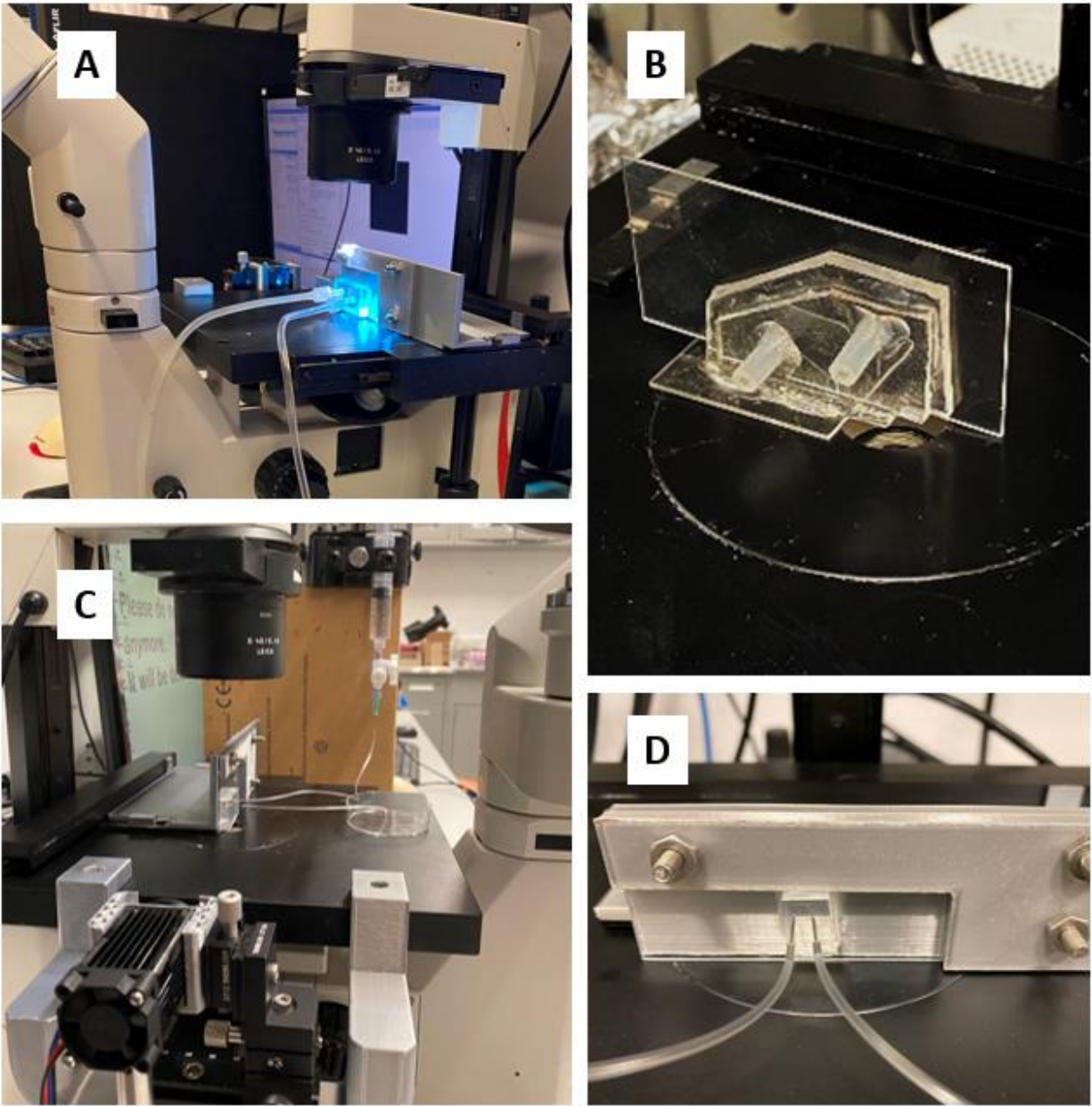


Figure 4-3 Images of the mounted platform before and after external and internal modifications. A) The previous chip configuration features the platinum-cured silicone tubing, securely mounted on the 3D printed fixture. B) The previous chip, positioned on the older glass fixture, is intended for attachment to the microscope stage using tape. C) The previous chip showcasing the Tygon tubing, mounted on the 3D printed fixture, providing the capability to load worms from the upper hand. D) The internally modified chip, significantly reduced in size, is equipped with the Tygon tubing inlet and outlet, enhancing overall compactness and functionality.

The primary objective of reducing the tubing's inner diameter to one-third of its original size was to eliminate the need for repeatedly unplugging and plugging the inlet tubings during worm injections, as explained earlier in this section. The smaller cross-sectional area of the tubing enables us to introduce worms from the top, reducing the risk of contamination and minimizing

worm loss. Most importantly, this modification allows us to introduce a larger quantity of worms in each run, optimizing experimental efficiency.

Despite the ability to introduce a larger population of samples to the device, the time each worm spent at the light sheet was not ideally consistent. Initially, a T-junction was added to the inlet as a worm inlet to merge with the M9 flow into the device, as depicted in Figure 4-4A. However, the high pressure required to force the worms into the device prevented adequate imaging of the specimens in the microchannels. To achieve better control over the samples' velocity, we introduced a centrifugal tube with a bottom hole. The inlet tubing was connected to this hole to allow worms to pass into the device. Additionally, a side hole was pierced in the tube to connect the syringe pump, which served as a reservoir to provide the required flow. (Figure 4-4B) However, this approach lacked the ability to adjust to the slight variation in sample size, as mentioned earlier in the experimental and setup section, prompting the exploration of alternative solutions such as pressure pumps.

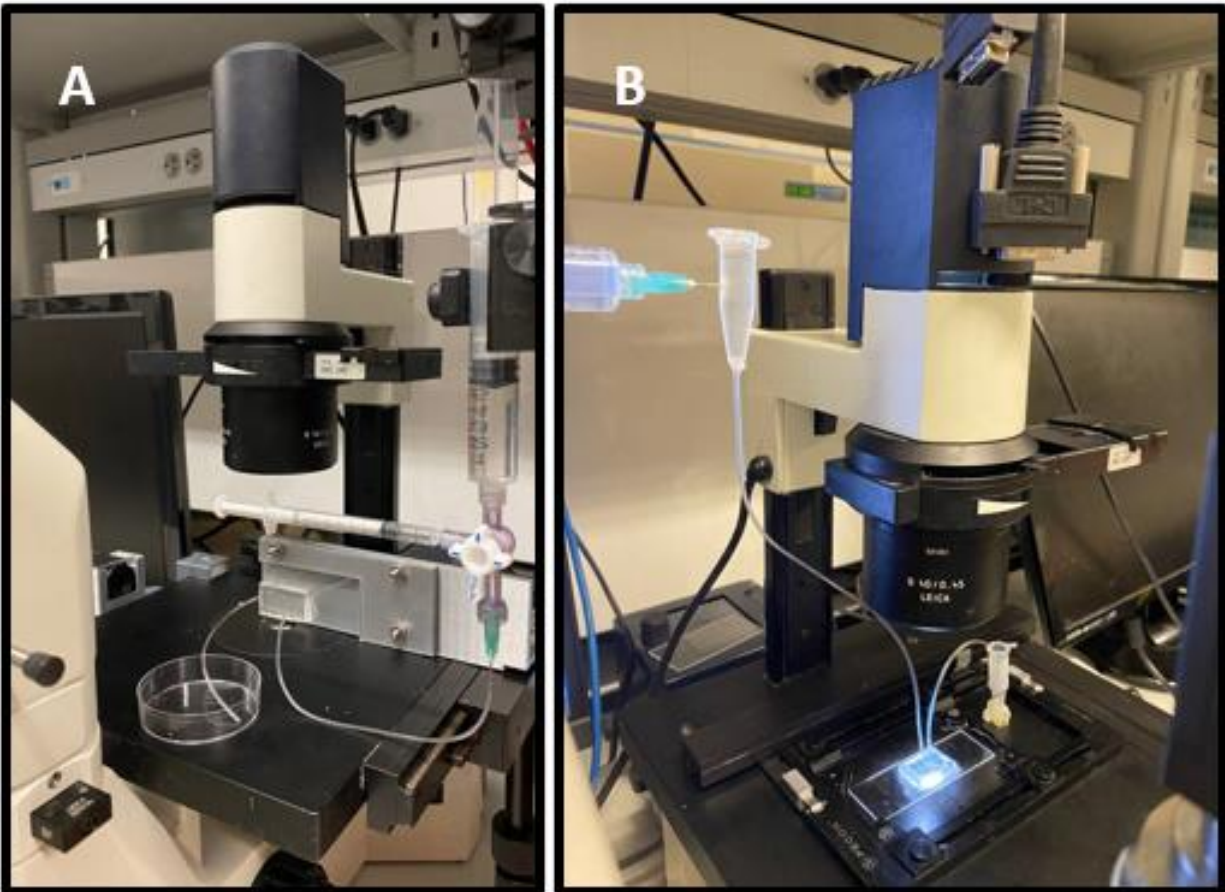


Figure 4-4 Approaches to address the challenges faced during the laser alignment and loading of worms into the imaging device. A) Schematic of the designed fixture to hold the optofluidic device on top of the host objective with respect to the laser beam. B) The actual fixture is mounted on the inverted microscope. C) Worm loading T-junction setup. D) The centrifugal tube with a hole at the bottom was introduced as the worm reservoir that prevents the sinking of worms but lacked control over the flow of specimens, leading to the exploration of alternative solutions such as pressure pumps.

#### **4.1.1 Internal Design Iterations**

In an alternative approach, we endeavoured to enhance the sample handling procedure by modifying the internal features of the optofluidic chip. The initial design incorporated an inverse tapered area within the channel to accommodate the NA of the detection lens. However, this design led to a problem where the tip of the worms became trapped in the outer bend, as shown in Figure 4-5A. To overcome this issue, we adjusted the bend angle to guide the worms in the correct direction without compromising resolution. However, this modification resulted in a slight variation in the number of frames acquired from small and large worms, as depicted in Figure 4-5B. Furthermore, the presence of large worms obstructing the bend created back pressure, causing subsequent worms to pass the light sheet swiftly. To tackle this problem, we attempted to introduce an additional microchannel above the light sheet to act as an exhaust microchannel and collect a portion of the back pressure. Unfortunately, as seen in Figure 4-5C, despite making the cross-section of the extra microchannel as small as the fabrication limits, worms were drawn into the channel, leading to system clogging.

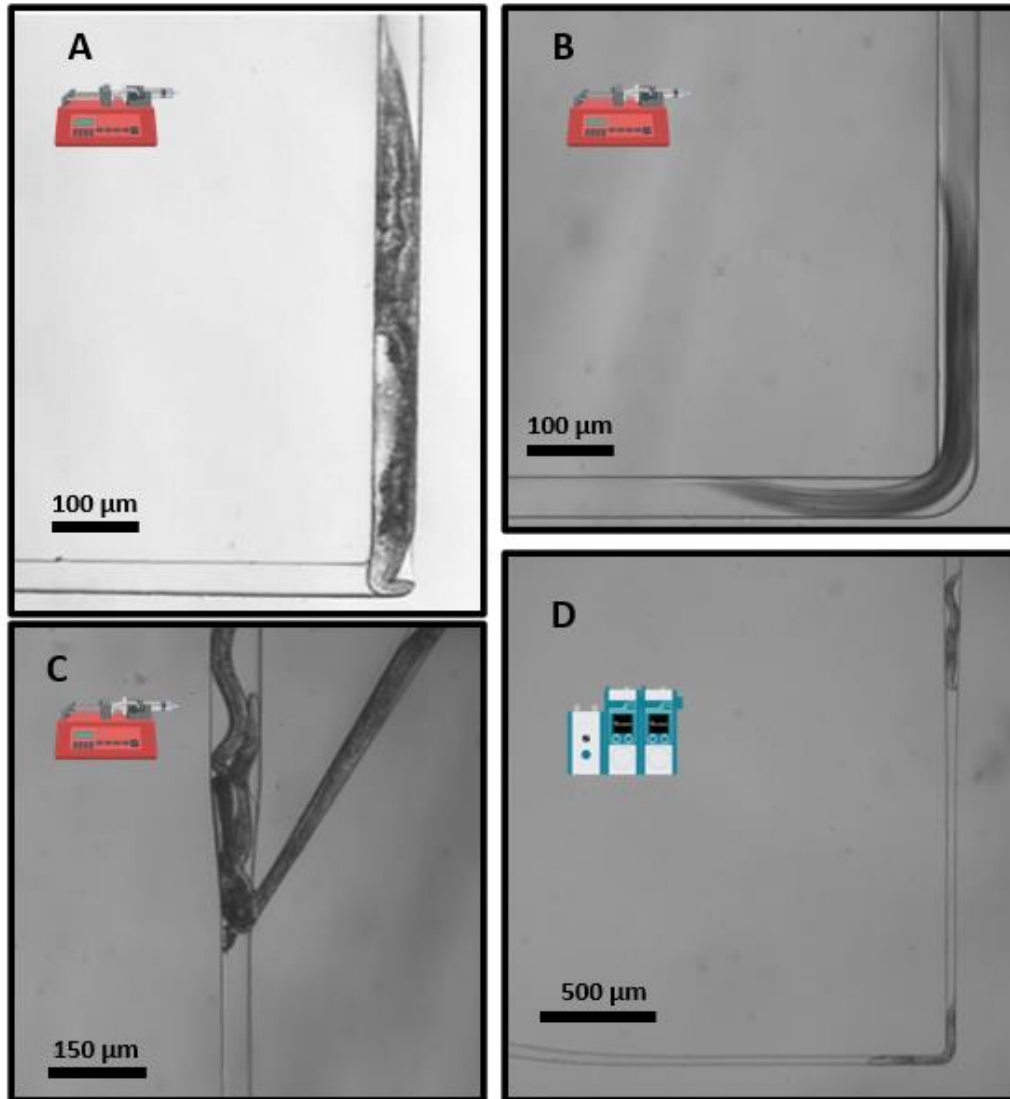


Figure 4-5 Internal design iterations A) The initial design showcases the incorporation of an inverse tapered area within the channel to accommodate the NA of the detection lens. B) Adjusted bend angle in the microchannel design, effectively guiding the worms in the desired direction while maintaining resolution. C) An additional microchannel above the light sheet was introduced, designed to alleviate back pressure by collecting and reducing the buildup of pressure above the bend within the main channel. D) Successful integration of a newly acquired pressure pump into the design, enabling the functioning of the adjusted bend design in the microchannel.

As previously discussed, the disparity in diameter between the tubing and microchannel posed challenges concerning the smooth and consistent passage of the worms. Intensive experimentation and alterations to both external and internal features of the device emphasized the necessity for a pressure pump and a flow meter as the optimal solution.

Ultimately, the incorporation of a newly acquired pressure pump allowed the previous design with the adjusted bend to function properly, enabling the acquisition of the desired number of frames

with adequate variation from each worm. (Figure 4-5D) The pressure pump's primary advantage was its encapsulated inlet reservoir, which facilitated uninterrupted injection of approximately 700 worms, irrespective of their size, 60 times more than the previous setup. The microfluidic flow sensor (FLOW UNIT, Fluigent, France) was another component of the flow delivery system that enabled the platform to adapt to slight variations in worm size by controlling the pressure and flow rate within the optofluidic chip based on the liquid type and the sensor readings (Fulfilling Objective. 1). Additionally, unlike the previous setup, the flow delivery system can supply a continuous stream of worms without bubbles, contamination, or requiring device re-focusing.

#### **4.1.2 Experimental Conditions**

Experiments were conducted to determine the optimal concentration of worms for continuous imaging studies while avoiding device clogging. Three different worm concentrations (100, 75, and 50 worms/mL) were tested. Initially, a preliminary experiment was performed using the highest concentration (100 worms/mL) at a 3  $\mu\text{L}/\text{min}$  flow rate, resulting in channel clogging due to worm accumulation in the bend section. Consequently, the highest concentration was diluted to achieve 75 and 50 worm/mL concentrations, which did not cause any clogging issues since the objective was to continuously image worms at the highest possible throughput, 75 worms/mL concentration was selected for further experiments.

A sufficient number of frames throughout the worm's length was required to capture clear, blur-free images without motion artifacts. Considering the region of interest, our camera could capture up to approximately 900 frames per second (fps). However, preliminary experiments revealed that although a flow rate of 9  $\mu\text{L}/\text{min}$  seemed appropriate, the camera couldn't acquire an adequate number of frames due to the high speed of worms under this flow condition. Consequently, an experiment was conducted to determine a suitable worm speed (or passing the time through the light sheet) at lower flow rates, allowing the camera to acquire a reasonable number of cross-sectional images.

Figure 4-6 illustrates the acquired frames of worms through the light sheet at flow rates of 3, 5, and 9  $\mu\text{L}/\text{min}$ , using the selected concentration of 75 worms/mL. As expected, the average passing time increased as the flow rate decreased, indicating that worms moved at lower velocities. The 9  $\mu\text{L}/\text{min}$  flow rate resulted in an average acquired frame of  $85.39 \pm 86$  per worm. However, preliminary experiments at this flow rate produced blurry images due to the worm's high velocity

(Figure 4-6). Therefore, the flow rate was further reduced to 5  $\mu\text{L}/\text{min}$ , resulting in an average acquired frame of  $322.9 \pm 83$ . Notably, the quality of light-sheet images improved under this configuration (Figure 4-6).

Based on the aforementioned observations and measurements, a 5  $\mu\text{L}/\text{min}$  flow rate was chosen as the operating flow rate for continuous imaging. It's important to note that the decision to reduce the flow rate was driven by the limitations of our camera setup and should not be regarded as a fundamental limitation of the developed technology. The characterization tests described above were performed in the horizontal orientation (Figure 4-5) of the device, allowing observation of worm movement within the microchannel using the inverted microscope's native optics. These findings are expected to apply to the device's final vertical orientation (Figure 4-7) for light-sheet imaging, as gravitational forces are negligible in microfluidic settings due to scaling laws.

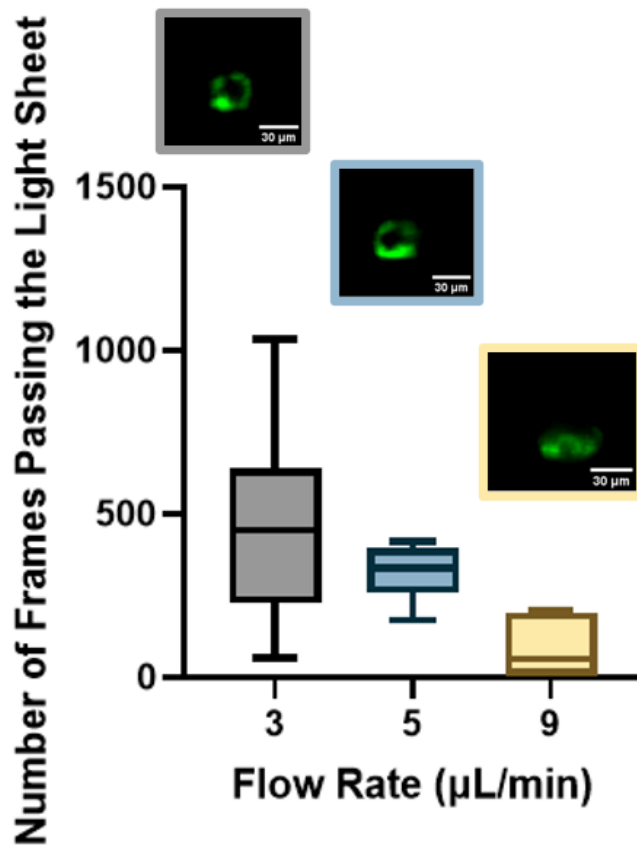


Figure 4-6 Number of frames acquired from each worm at different flow rates of 3, 5, and 9  $\mu\text{L}/\text{min}$  for  $n=10$  worms for each flow rate. Cross-sectional light sheet images of the NW1229 nerve ring at each flow rate are represented above the corresponding chart.

## 4.2 Continuous pan-neural light sheet imaging of *C. elegans* at different developmental stages

We use the setup and optofluidic device reported in Figures 3-2 and 3-1 to continuously image populations of NW1229 expressing GFP pan-neuronally at L3 and YA stages. The NW1229 strain is chosen as its pan-neural fluorescent expression enables better platform resolution and throughput testing using light sheet microscopy. Owing to the flow-based cross-sectional imaging ability of the developed system, comprehensive microscopic imaging can be done on worm populations, and any region of the nervous system can later be studied for further analysis. For example, Figure 4-7A depicts the light sheet images of DA neurons, which are of great interest in neurodegenerative disorders such as PD, for two populations of NW1229 at the L3 and YA stages. Each population involves 120 worms that are imaged within ~4.9 and ~5.8 min for the L3 and the YA worms, respectively. Figure 4-7B shows representative high-resolution light sheet images of the nerve ring for the two developmental stages. The nerve ring forms an O-shaped or U-shaped structure at both stages, depending on the distance between neurons. If they are in close proximity, they fit within a single image slice, creating an O-shape pattern. In contrast, if they are sufficiently separated when the worm is passing through the light sheet, neurons cannot be captured within the same image slice. In such cases, one pair is clearly captured in a frame while the other pair appears in the background, resulting in a U-shaped pattern. Owing to such inevitable variations, for the purpose of quantitative analyses, we partition and compare the entire DA region frames rather than comparing a single representative frame of the nerve ring. The system continuously and consistently captures similar high-resolution light sheet images of other anatomical locations of the worm. Such images can be stitched together to offer comprehensive and volumetric fluorescent expression maps of worm populations, such as the representative volumetric image depicted in Figure 4-7C for an L3 worm composed of ~1000 frames. Here, the figure insets show high-resolution light sheet images of neuronal expressions along the worm's body from head to tail at six different anatomical locations. The results depicted in Figure 3 qualitatively demonstrate the ability of the developed low-cost platform in continuous light sheet fluorescent imaging of *C. elegans* populations for studying their neuronal expressions at different developmental stages, at high speed and with high resolution, which confirms the successful accomplishment of the second research objective.

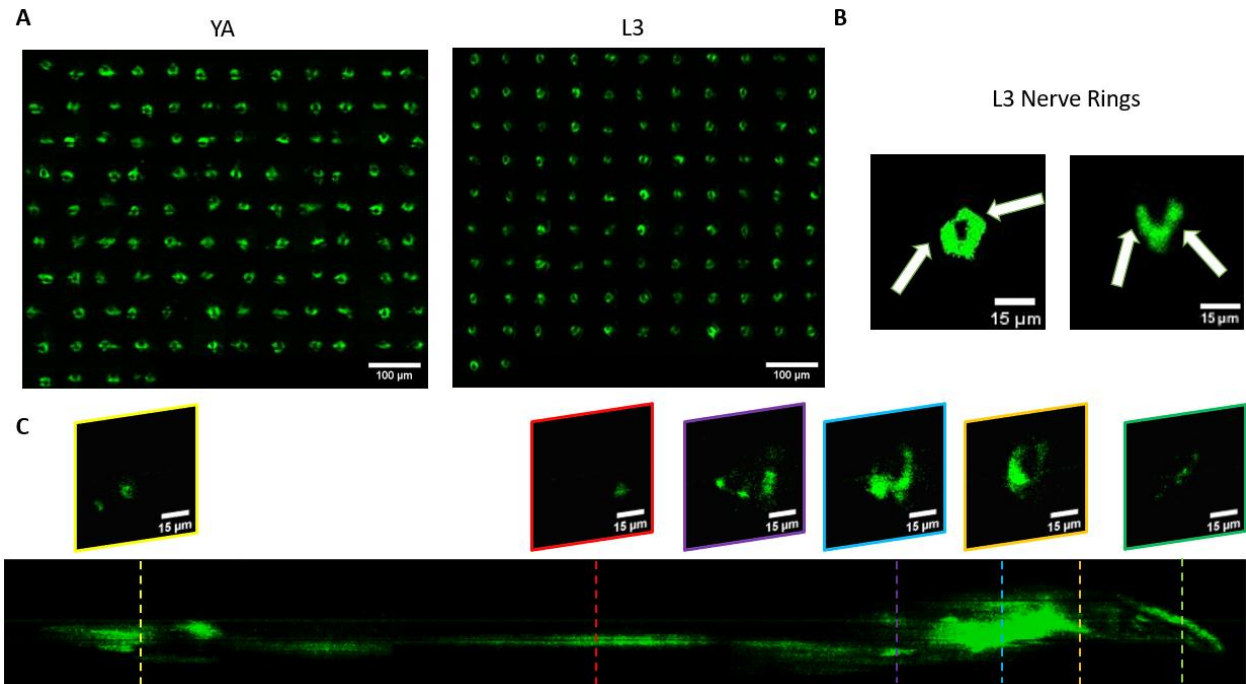


Figure 4-7 Qualitative analysis of the fluorescent expression of NW1229 worms at two developmental stages. A) Montage of cross-sectional images of fluorescence expression of the nerve ring of worms at YA (Left) for n=112 worms and L3 (Right) stages for n=101 worms. B) Representative cross-sectional images of fluorescence expression of nerve rings in L3 worms in O and U shapes indicated by white arrows. C) Comprehensive stack of images with ~1000 acquired frames of NW1229 strain with representative slices showing the nervous system in detail.

In Figure 4-8, we present the results of the fluorescence intensity analysis for two distinct developmental stages of the NW1229 strain at the YA and L3 stages. These figures showcase the normalized shaded line charts representing the intensity of fluorescence across the body of ten individual worms at each stage. The fluorescence intensities have been meticulously normalized based on the entire dataset obtained for the YA and L3 samples to facilitate the comparison of the two developmental stages. The shaded area signifies the variance in fluorescence intensity observed within the group of worms at both stages. By comparing the normalized fluorescence intensities of both stages, we can gain a deeper understanding of how the fluorescence distribution changes as *C. elegans* progresses from the L3 stage to young adulthood.

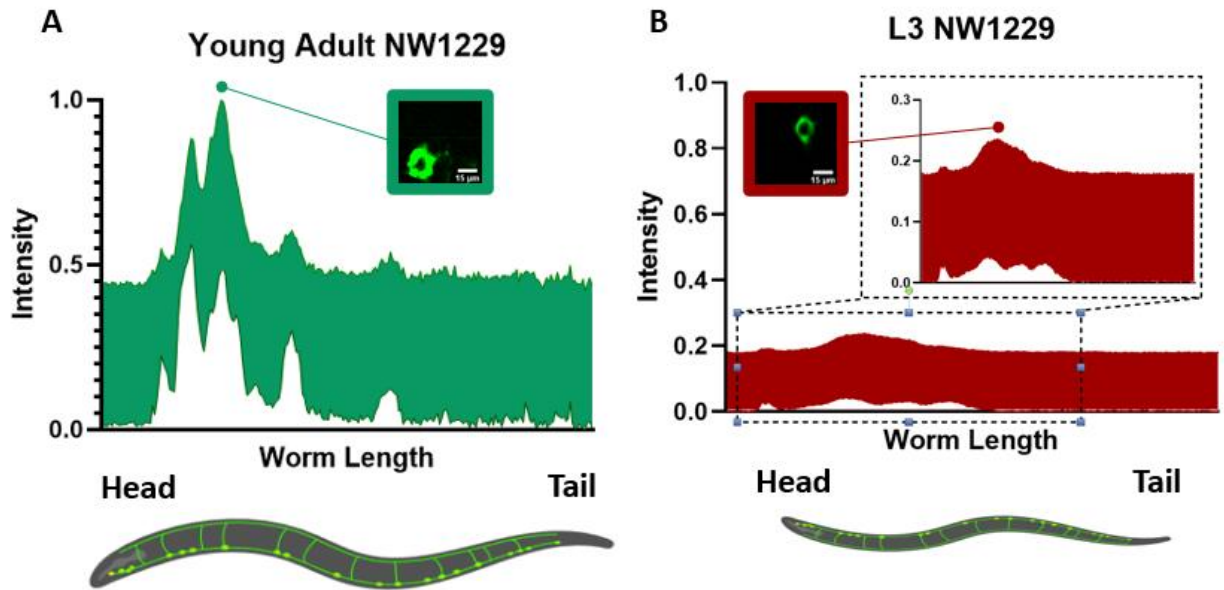


Figure 4-8 Shaded error bar graphs of normalized fluorescence expression in nerve ring (Peak) for YA and L3 NW1229 A) Shaded error bar graph representing the normalized fluorescence expression of YA NW1229 from head to tail. The analysis is based on a sample size of  $n=10$ , with error bars indicating the variability in fluorescence levels. Inset Image: A representative inset image of the nerve ring (peak) showcasing the fluorescence expression pattern for YA NW1229. B) Shaded error bar graph illustrating the normalized fluorescence expression of L3 NW1229 along the head-to-tail axis. The data is derived from  $n=10$  replicates, and the error bars indicate the degree of variation. Inset Image: A representative inset image of the nerve ring (peak) displaying the fluorescence expression pattern for L3 NW1229. Scale bars in both images are 15 microns.

Quantitative image analysis can provide insights into the molecular and cellular mechanisms underlying the development of the *C. elegans* nervous system. GFP expression histograms can be advantageous in evaluating the overall size and expression strength of neurons and proteins. The DA region of ~100 different NW1229 worms for each age was separated, and the entire stack's histogram was evaluated. As shown in Figure 4-9A, this comparative histogram displays the number of pixels corresponding to each intensity value for the L3 and YA worm populations. The x-axis represents the fluorescence intensity, while the y-axis accounts for the number of pixels, which shows the area of the expression region. To enhance the visualization of the graph, these first two intensity values were removed from the histogram, as they were deemed to be equivalent to the background. Both histograms exhibit identical shapes, featuring a peak in the lower intensities and a gradual decrease towards the higher intensity values. This observation indicates that the fluorescence expressions predominantly consist of weak signals, far from reaching saturation levels. An additional variable of interest for analysis is the distribution of the histogram, which offers insight into the prevalence of particular intensity values and provides an overview of the fluorescence expression strength of the neurons. The histogram of the YA population exhibits

a greater number of pixels compared to the larval stage (L3), indicating a larger area of fluorescence expression. Similarly, this pattern is replicated in the intensity values of the pixels, with YA pixels corresponding to higher intensity values, indicative of more robust fluorescence expression. We posit that the growth of the worm's nervous system is the underlying factor contributing to the observed augmentation in both the area and intensity of fluorescence expressions. To explore the growth in a more quantitative manner, we conducted calculations and compared the MINRs for a sample size of ~100 worms, as depicted in Figure 4-9B. Statistical analysis of quantified parameters reveals a significant difference between the YA and L3 MINR. The MINR in the L3 group is 6.83 (SD = 1.81), whereas the mean in the YA group is 13.05 (SD = 3.18). A Welch's t-test showed that the difference was statistically significant,  $t(180.5) = 17.63$ ,  $p < 0.0001$ ; where  $t(180.5)$  is a shorthand notation for a Welch t-statistic that has 180.5 degrees of freedom.

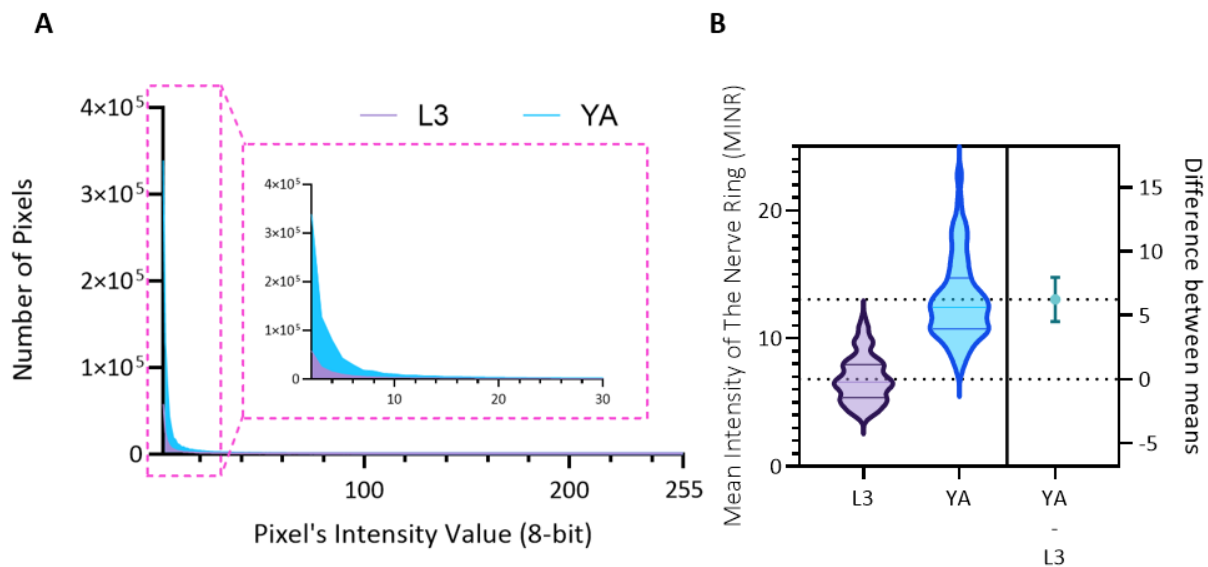


Figure 4-9 Quantitative analysis of the mean fluorescence intensity in the pan neuronal NW1229 nerve rings. A) Histograms illustrate the increase in both the spatial extent and intensity of expression due to aging. The number of pixels, serving as a representative measure of the area, consistently demonstrates an upward trend. Simultaneously, the maximum intensity value exhibits a corresponding rise, reflecting the heightened magnitude of expression. The Inset view displays the zoom view of the first 30 pixel intensity values. B) Violin plots depicting the distribution of data for L3 (left) and YA (middle) groups. The dashed lines at the top and bottom of each violin represent the first and last quarters of the data, respectively, while the middle line denotes the median. The dashed lines that cross the right y-axis correspond to the mean value for each group. The mean value of L3 is set as the origin (0), and the difference in means between L3 and YA is illustrated by a 95% confidence interval (CI) bar extending to the mean of YA.

Results of Figures 4-7 to 4-9 show the capability of the low-cost and compact platform in providing high-content light sheet images of worm populations at different developmental stages and the platform's ability to quantify neuronal expressions. The adaptability of the platform to various developmental stages is particularly advantageous in capturing the increased fluorescence expression observed in aging worms, attributed to the growth of their neurons, which can be accurately detected and statistically quantified. We anticipate that the same platform can be adapted for carrying out studies on other model organisms across various developmental stages or for cell studies.

#### **4.2.1 Protein Aggregation Analysis of Larval and Young Adult PD Model Transgenic *C. elegans***

As introduced earlier,  $\alpha$ -Syn is a protein implicated in neurodegenerative disorders such as PD, and the buildup of this protein in the brain can result in harm to neurons [81]. The ERS100 transgenic PD model is a valuable worm strain for understanding PD's pathogenesis and evaluating potential therapies. The ERS100 expresses GFP fluorescence based on  $\alpha$ -Syn accumulation in its DA. It is a great candidate for PD drug studies as the  $\alpha$ -Syn development can be monitored and measured during its life span. According to the strain's description, the most dominant phenotype is the inclusion of  $\alpha$ -Syn in CEP axons, which increases after the L2 stage and continues until adulthood. As part of the third research objective, we conducted quantitative light sheet imaging to investigate the feasibility of utilizing our technology for  $\alpha$ -Syn accumulation studies in the ERS100 strain.

Figure 4-10A illustrates the DA neurons regions of L3 and YA ERS100 worms (n=148 for L3 and n=62 for YA) with  $\alpha$ -Syn aggregation in their DA neurons. In Figure 4-10B, the presence of fluorescence clusters in the DA neurons is visible. The volumetric stack of images acquired with the low-cost light sheet from the transgenic strain shows the protein expression at the L3 stage, as illustrated in Figure 4-10C. This fluorescence intensity is not comparable quantitatively to those of the pan-neural strain in Figure 4-7 since the NW1229 and ERS100 strains demonstrate different reporter expressions representing fluorescence expression of neurons and protein aggregations, respectively.

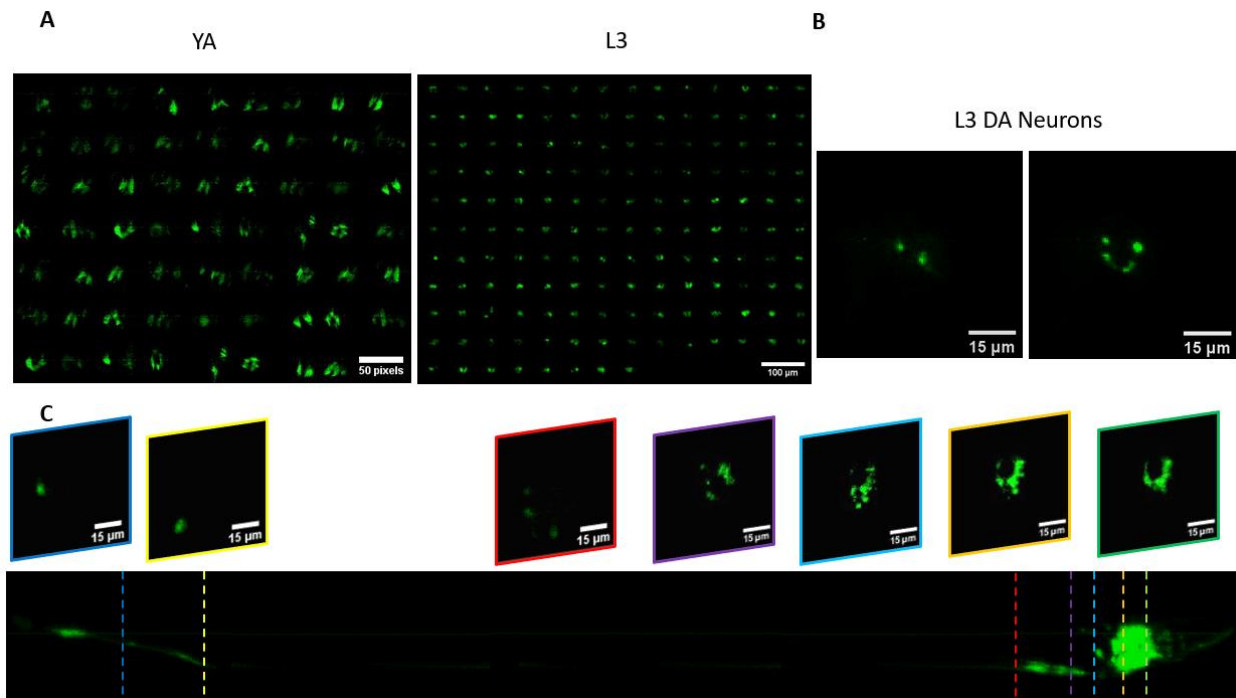


Figure 4-10 Qualitative analysis of the fluorescent expression of ERS100 worms at two developmental stages. A) Cross-sectional images of fluorescence expression of the DA neurons of worms at YA (Left) for n=62 worms and L3 (Right) for n=148 worms. B) Representative cross-sectional images of fluorescence expression of DA neurons in L3 worms. C) Comprehensive stack of images with ~1000 acquired frames of ERS100 with representative slices showing the neuronal expressions in detail.

Figures 4-11 present the comprehensive results of the fluorescence intensity analysis conducted on ERS100 transgenic worms at two distinct developmental stages: YA (Figures 4-11A) and L3 (Figures 4-11B). These figures exemplify the use of normalized shaded line charts, which effectively portray the fluorescence intensity profiles across the bodies of ten individual worms at each developmental stage. The normalization process is based on the entire dataset acquired from YA and L3 samples, ensuring a reliable basis for the comparative analysis. The shaded regions in the charts represent the inherent variance in fluorescence intensity observed within the groups of worms at both stages. Unlike the panneural strain, where fluorescence expression is more widespread, the localized nature of fluorescence expressions (specifically confined to DA neurons) results in more distinct peaks in fluorescence intensity throughout the worm's body, even during the third larval stage of development (Figures 4-11B). This phenomenon highlights the device's sensitivity in detecting differences in fluorescence expression patterns, accentuating its suitability for detailed investigations in neurobiological research.

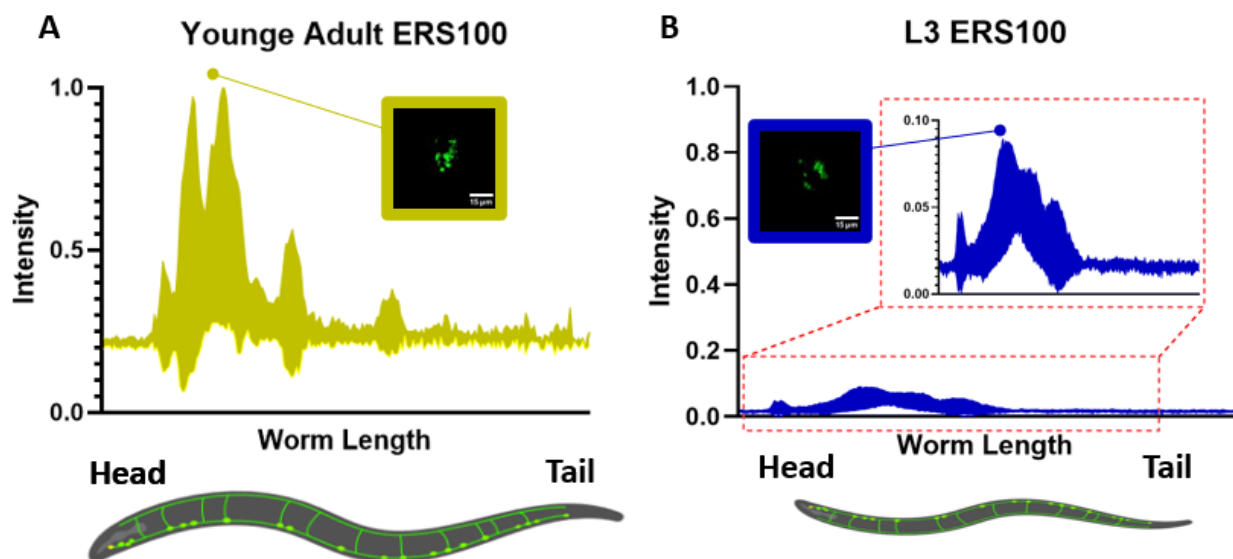


Figure 4-11 Shaded error bar graphs of normalized fluorescence expression in nerve ring (Peak) for YA and L3 ERS100 A) Shaded error bar graph representing the normalized fluorescence expression of YA ERS100 from head to tail. The examination relies on a sample size comprising of  $n=10$ , with error bars indicating the variability in fluorescence levels. Inset Image: A representative inset image of the nerve ring (peak) showcasing the fluorescence expression pattern for YA ERS100. B) Shaded error bar graph illustrating the normalized fluorescence expression of L3 ERS100 along the head-to-tail axis. The data is derived from  $n=10$  replicates, and the error bars represent the extent of variability. Inset Image: A representative inset image of the nerve ring (peak) displaying the fluorescence expression pattern for L3 ERS100. Scale bars in both images are 15 microns.

The relationship between aging and the development of  $\alpha$ -Syn is complex and involves multiple pathways and mechanisms. However, evidence indicates that aging is a significant risk factor for developing alpha-synucleinopathies [82]. Hence, by observing the changes that occur at different stages of development or in response to different treatments, researchers can gain insights into the biological processes that underlie diseases and identify potential targets for intervention. Here, we monitor and quantify the penetrance and blebbing of  $\alpha$ -Syn in the nerve ring of ERS100 worms at the L3 and YA stages. The mean fluorescence intensity (MFI) measures the level of  $\alpha$ -Syn accumulation in the specific phenotype location, providing a quantified assessment of its abundance. As shown in Figure 4-12A, the MFI and aging are positively correlated. Furthermore, Figure 4-12B indicates that the difference between MFI at L3 and YA was statistically significant (A Welch's t-test,  $t(78.17) = 9.38$ ,  $p < 0.0001$ ).

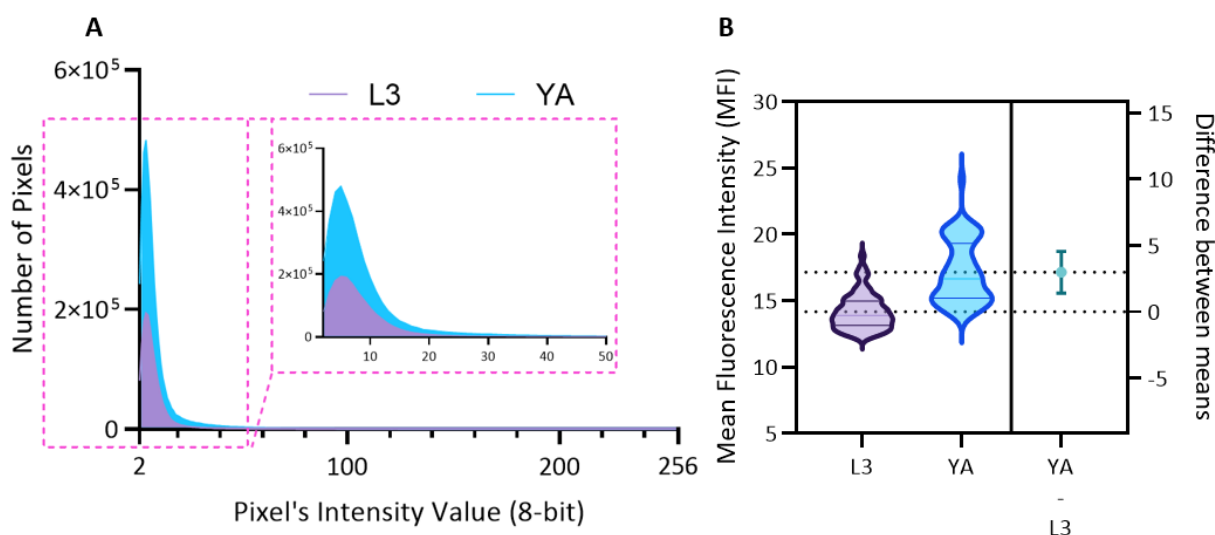


Figure 4-12 Quantitative analysis of the mean fluorescence intensity in the PD model ERS100 DA neurons. A) Histograms illustrate the increase in both the spatial extent and intensity of expression due to aging. The number of pixels, serving as a representative measure of the area, consistently demonstrates an upward trend. Simultaneously, the maximum intensity value exhibits a corresponding rise, reflecting the heightened magnitude of expression. The Inset view displays the zoom view of the first 50 pixel's intensity value. B) Violin plots depicting the distribution of data for L3 (left) and YA (middle) groups. The dashed lines at the top and bottom of each violin represent the first and last quarters of the data, respectively, while the middle line denotes the median. The dashed lines that cross the right y-axis correspond to the mean value for each group. The mean value of L3 is set as the origin (0), and the difference in means between L3 and YA is illustrated by a 95% confidence interval (CI) bar extending to the mean of YA.

The comprehensive results of Figures 4-10 to 4-12 clearly show progressive distribution and aggregation of  $\alpha$ -Syn in the nerve ring region and axons of interconnected neurons as the worms age both qualitatively and quantitatively. The obtained results from validation studies align with previous reports, demonstrating the ability to obtain crisp light sheet images from a population of worms via the simple addition of our low-cost add-on platform to a conventional microscope [30], [83].

#### 4.2.2 Throughput of the optofluidic light sheet add-on device

Our findings illustrate the practicality of employing the suggested light sheet microscopy technique for rapid imaging of larval and young adult *C. elegans* utilizing a standard fluorescent microscope. The imaging process involves acquiring approximately 400 frames from each worm in about half a second. As shown in Table 4-1, the throughput for imaging worms at the L3 stage was  $24.64 \pm 2.05$  worms/minute, while the throughput for imaging worms at the YA stage was  $20.67 \pm 2.49$  worms/minute.

In practice, the worm population movement in microchannels is random, and solely increasing the specimen concentration will not lead to higher throughput, as overcrowding in the chip will cause channel clogging and experimental failure. In a series of preliminary experiments, we landed on ~75 worms per mL to avoid clogging the device while providing enough flow of worms for imaging 20+ worms/minute. The maximum ideal throughput reported in Table 4-1 will reach over a hundred if worms pass back-to-back without blank frames between them. Such throughput optimization for reaching the ideal limit can be achieved by various means. For example, the addition of a specific concentration of ethanol can immobilize the worms and act as a surfactant within the microchannels, thereby facilitating smoother worm passage [84].

Table 4-1 Frame rate, functional (obtained) throughput and hypothetical maximum throughput of the proposed optofluidic device for YA and L3 *C. elegans* light sheet imaging.

Age	Acquired Frames	Frame Rate (FPS)	Functional Throughput (worms/min)	Ideal Limit Throughput (worms/min)
L3	~400	865	24.64±2.05	~130
YA			20.67±2.49	

The camera's frame rate also limits the device throughput as the worm transportation velocity must comply with the frame rate to avoid significant under-sampling. Another key consideration related to frame rate and, thus, throughput is the strength of fluorescence expression in the worm model. Reliable imaging of weak neuron fluorescence expressions requires increasing camera integration/exposure time, which lowers the frame rate and throughput. Choosing the smallest possible ROI will maximize the frame rate using the windowing setting of cameras to enhance the frame rate. For instance, in our system, an ROI just large enough to cover the channel cross section (65×65  $\mu\text{m}^2$ ) yields the maximum frame rate of 865 FPS while this value at full frame (16.64×14.04  $\text{mm}^2$ ) can be as small as 100 FPS.

Despite these considerations, our high-throughput light sheet imaging platform holds significant promise in the field of drug screening assays, where worm populations typically range from ~30 to 300 worms [85]–[89]. Although our throughput was moderate compared to more complex and costly setups [70], our platform excels by enabling high-resolution imaging of the desired worm population within a matter of minutes.

While it is true that our low-cost light sheet platform has a lower throughput when compared to the complex setups mentioned earlier, it provides an excellent compromise between performance and cost (Table 4-2), making it an attractive option for most researchers and biologists to advance their research endeavours.

Our cost-effective platform, equipped with a microfluidic chip and high frame rate sCMOS camera, performed a neural screening of *C. elegans*, enabling the detection of protein and neuron expressions with a throughput of >1200 worms per hour. The affordability of the platform was ensured by incorporating an excitation add-on arm on a WF microscope, as well as microfluidic chips instead of robotic systems for sample handling.

Table 4-2. Overview of Imaging Studies Utilizing *C. elegans* Light Sheet Microscopy This table provides an overview of imaging studies that employed *C. elegans* light sheet microscopy, including details on the imaging objectives, worm strain and age, resolution, and performance.

<i>C. elegans</i> light-sheet imaging	Resolution ( $\mu\text{m}$ )		<i>C. elegans</i> Strain	Age	Performance
	Lateral	Axial			
Identification of neurons expressing transcription factor and visualization of neurodevelopmental dynamics [7]	0.52	1.7	BV24, BV117	Embryo	Throughput (1/3) Affordability (2/3)
Imaging PVD sensory neurons and nuclei in the intestinal [5]	1.1	6.2	NC1686	Adult	Throughput (2/3) Affordability (2/3)
Phenotypic screening of polyglutamine aggregation in Huntington's disease model [70]	3.5	3.5	CZ10175 CZ1200 PolyQ24 PolyQ40	L4	Throughput (3/3) Affordability (1/3)
Imaging DNPs using a low-cost light sheet add-on device [13]	1.1	2.4	NW1229; BZ555	Adult	Throughput (1/3) Affordability (3/3)

Neural and $\alpha$ -Syn accumulation monitoring of wildtype and PD model (current study)	1.1	2.4	NW1229; ERS100	L3, YA	Throughput (2/3) Affordability (3/3)
---	-----	-----	-------------------	--------	---

### 4.2.3 High-Throughput Light Sheet Imaging Application in Chemical Screening

#### 4.2.3.1 6-OHDA Induced Toxicity

The application of high-throughput light sheet imaging in chemical screening holds great promise for accelerating drug discovery, understanding disease mechanisms, and identifying novel therapeutic compounds. 6-OHDA (6-hydroxydopamine) is a well-known neurotoxic agent widely used in neurodegeneration research. It selectively targets DA neurons, leading to their degeneration and subsequent motor impairments. The extensive literature on 6-OHDA-induced neurodegeneration provides a solid foundation for its use as a proof of concept in chemical screening for neurodegenerative processes [90]–[92].

Expanding on the well-established groundwork laid out by the comprehensive body of research concerning neurodegeneration induced by 6-OHDA, our research initiative involved the examination of NW1229 nematode worms at their L3 and YA developmental stages. This investigation encompassed observations made before and after subjecting the worms to 500  $\mu$ M of 6-OHDA. During this screening process, we aimed to measure the mean intensity of the nerve ring (MINR) at each stage for both control and exposed worms. Our platform enabled the detection of a decrease in MINR in response to 6-OHDA exposure in both L3 and YA stages, which aligns with the final part of the third research objective.

Figure 4-13 comprises four distinct sections, each depicting the results of a comparative study between control and exposed NW1229 to 6-OHDA at different developmental stages: L3 and YA. Within each section, a set of cross-sectional images of the nerve rings of animals is showcased. This image serves as a powerful demonstration of the device's high throughput capabilities, underscoring its ability to efficiently handle a large volume of data. Furthermore, the device's resolution and sensitivity are highlighted, as it adeptly captures and discerns subtle differences in fluorescence expression across varying developmental stages and under the influence of a small

dosage of 500  $\mu\text{M}$ . This representation underscores the device's potential as a valuable tool for investigating and understanding intricate nuances in fluorescence dynamics in the context of neurobiological research.

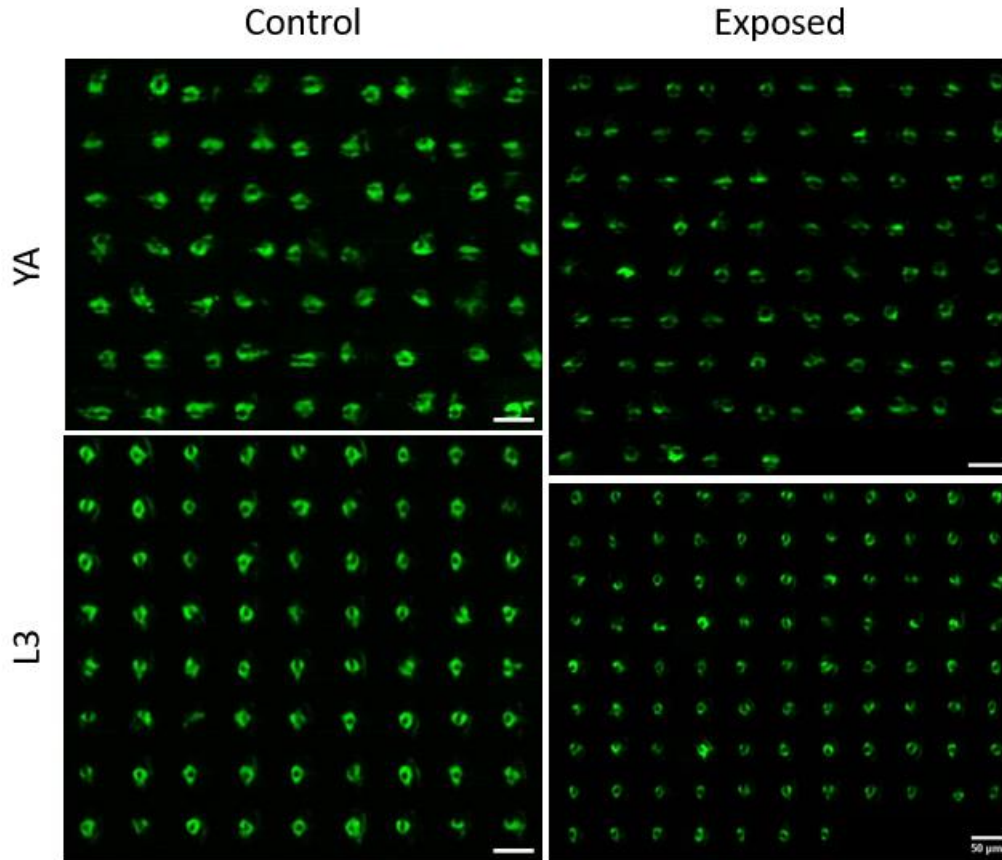


Figure 4-13 Cross-sectional images illustrating the fluorescence appearance within the nerve ring of the worms. The upper section (YA) depicts A) fluorescence expression in control worms (n=63) and B) fluorescence expression in exposed worms (n=85). The lower section (L3) illustrates C) fluorescence expression in control worms (n=72) and fluorescence expression in exposed worms (n=95). All scale bars indicate 50  $\mu\text{m}$ .

Furthermore, in the quantitative studies in L3-stage worms, we observed a significant decrease in normalized MINR for exposed worms at both developmental stages. We performed Welch's t-tests to evaluate the significance of differences between two datasets at different developmental stages. Specifically, for the third stage of development, Control (mean = 0.66) and Exposed (mean = 0.36) datasets were compared, yielding a highly significant p-value of  $<0.0001$  ( $\alpha = 0.05$ ) (Figure 4-14A). With Welch-corrected degrees of freedom at 105.4 and a t-statistic of 17.38, we confirm a significant difference between Control and Exposed worms at L3. Similarly, for the older worms at the YA stage, (Figure 4-14B) illustrates the comparison between Control

(mean = 0.73) and Exposed (mean = 0.34) datasets also produced a highly significant p-value of  $<0.0001$  ( $\alpha = 0.05$ ). Here, the Welch-corrected degrees of freedom was 95.79, and the t-statistic was 22.46, further affirming a significant difference between Control and Exposed worms at YA.

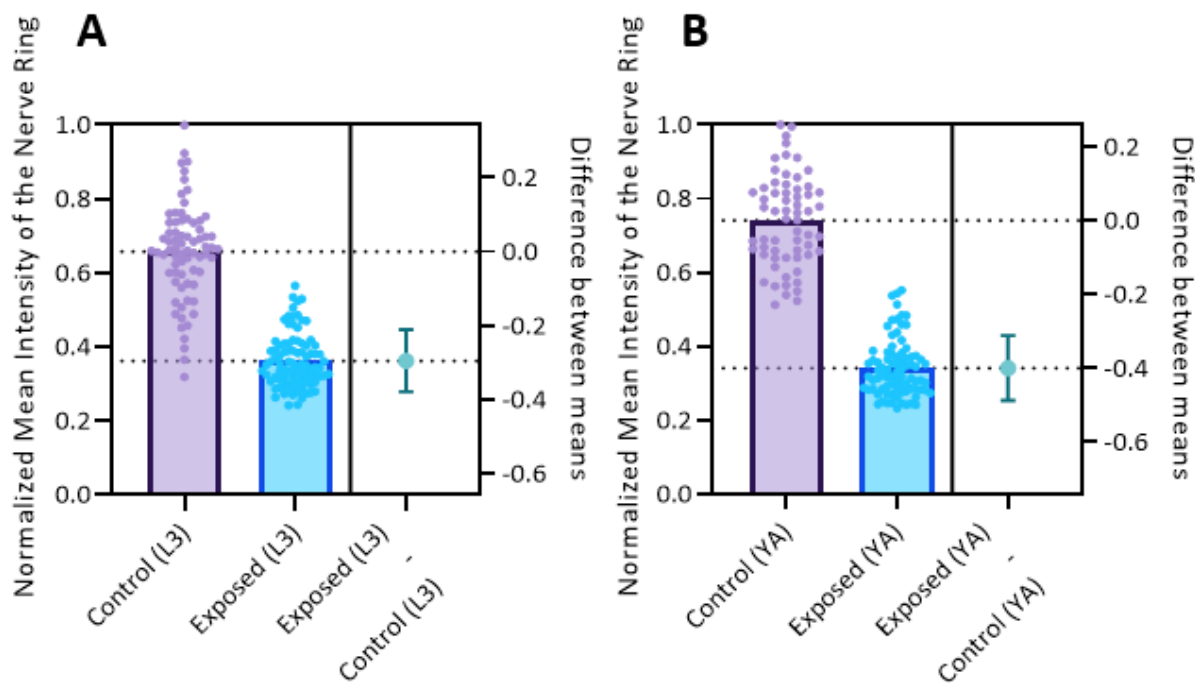


Figure 4-14 A quantitative assessment was conducted on the normalized mean intensity within the nerve ring of pan neural worms. Scatter dot plots are employed to visually represent the data distribution for the following scenarios: A) control (left) and exposed (middle) groups at the L3 stage, and B) control (left) and exposed (middle) groups at the YA stage. The dashed lines intersecting the right y-axis correspond to the respective mean values for each group. Notably, the mean value of the control group serves as the reference point (origin, 0), while the distinction in means between the control and exposed groups is graphically depicted by a 95% confidence interval (CI) bar.

#### 4.2.3.2 Manganese Induced Toxicity

Manganese (Mn) stands as the twelfth most abundant natural element within the Earth's crust [93]. It holds a crucial role as a transition metal essential for normal growth, developmental processes, and maintaining cellular balance [94]. Mn functions as an essential co-factor for several enzymes, including Mn superoxide dismutase, pyruvate carboxylase, arginase, and glutamine synthase. [95]–[98]. It can even take the place of magnesium (Mg) in several enzymatic reactions facilitated by kinases. While the body tightly regulates dietary Mn intake through the gastrointestinal tract (GIT) and its excretion via bile [99], inhaling toxic levels of Mn can result in inflammation of the nasal and pulmonary passages, impairment of kidney function, and neurodegeneration [100]–[102]. Recent research also indicates a link between elevated Mn concentrations in drinking water ( $>300$   $\mu\text{g/litre}$ ) and decreased cognitive function in children [103].

The impact on basal ganglia neurons due to Mn toxicity differs from the injury observed in Parkinson's disease, with distinct clinical and pathological characteristics setting the two conditions apart [104], [105]. Nevertheless, prolonged exposure to high levels of Mn (spanning over 20 years) has been associated with an increased risk of developing Parkinson's disease [106]. This suggests that in addition to inducing symptoms reminiscent of Parkinson's disease, Mn could also operate as an environmental factor in the progression of the disorder.

In our qualitative analysis, we presented montage images featuring hundreds of both control and exposed worms in Figure 4-15. The nerve ring fluorescence expression in L3 (Figure 4-15A to C) and YA (Figure 4-15D to F) stage worms is visually observed through arranged images. The comparison is drawn between control worms and those exposed to 5 and 10 mM  $MnCl_2$ . This visual representation provides a comprehensive overview of the qualitative variations in fluorescence expressions across different developmental stages and exposure groups, enhancing our understanding of the impact of experimental conditions on the observed outcomes.

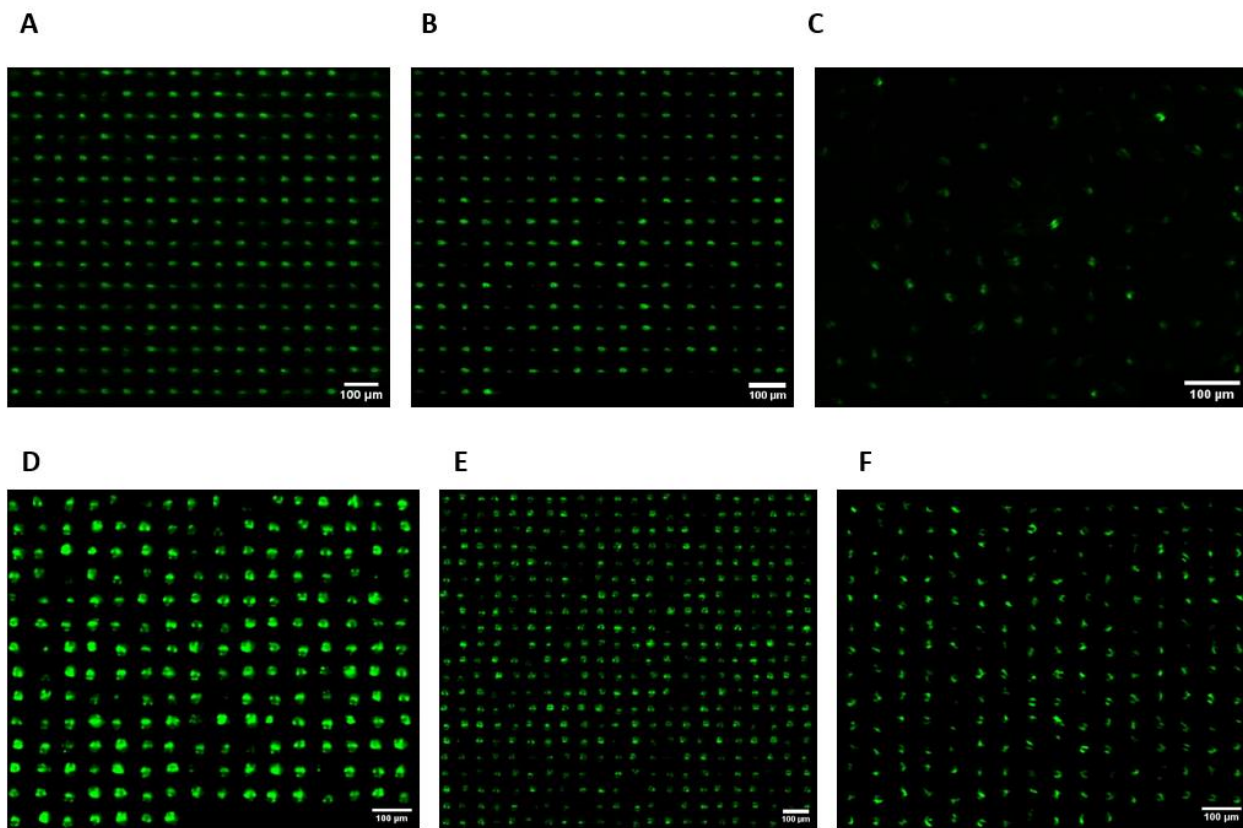


Figure 4-15 Qualitative analysis of L3 (Top of the panel) and YA (Bottom of the panel) for control and exposed worms to 5 and 10 mM  $MnCl_2$ . A) Fluorescence expression in L3 control worms (n=271) B) fluorescence expression in 5 mM exposed worms (n=257) and C) fluorescence expression in 10 mM exposed worms (n=115) D) Fluorescence expression in YA control worms

(n=215) B) fluorescence expression in 5 mM exposed worms (n=460) and C) fluorescence expression in 10 mM exposed worms (n=219).

The quantitative examination of MINR between control and exposed worms to  $MnCl_2$  at different developmental stages reveals intriguing patterns. In the experiment on mortality rates, we distinguished dead worms by observing the rigid and straightened morphology of their bodies, contrasting it with the more curved and flexible appearance of healthy *C. elegans*, as illustrated in Figure 4-16C and E. At the L1 stage, Figure 4-16A depicts our comparison of the control group with the 5mM and 10mM exposed groups that reveals a significant proportional trend of decreased survival from the control to the 5mM and 10mM exposed worms, respectively. Conveying, the toxicant demonstrated efficacy in inducing mortality among a proportion of treated worms. Additionally, the emergence of curled and coiled shapes (Figure 4-16D) in the treated worms post-exposure serves as another distinct behavioural phenotype indicative of the impact of the toxicants [32].

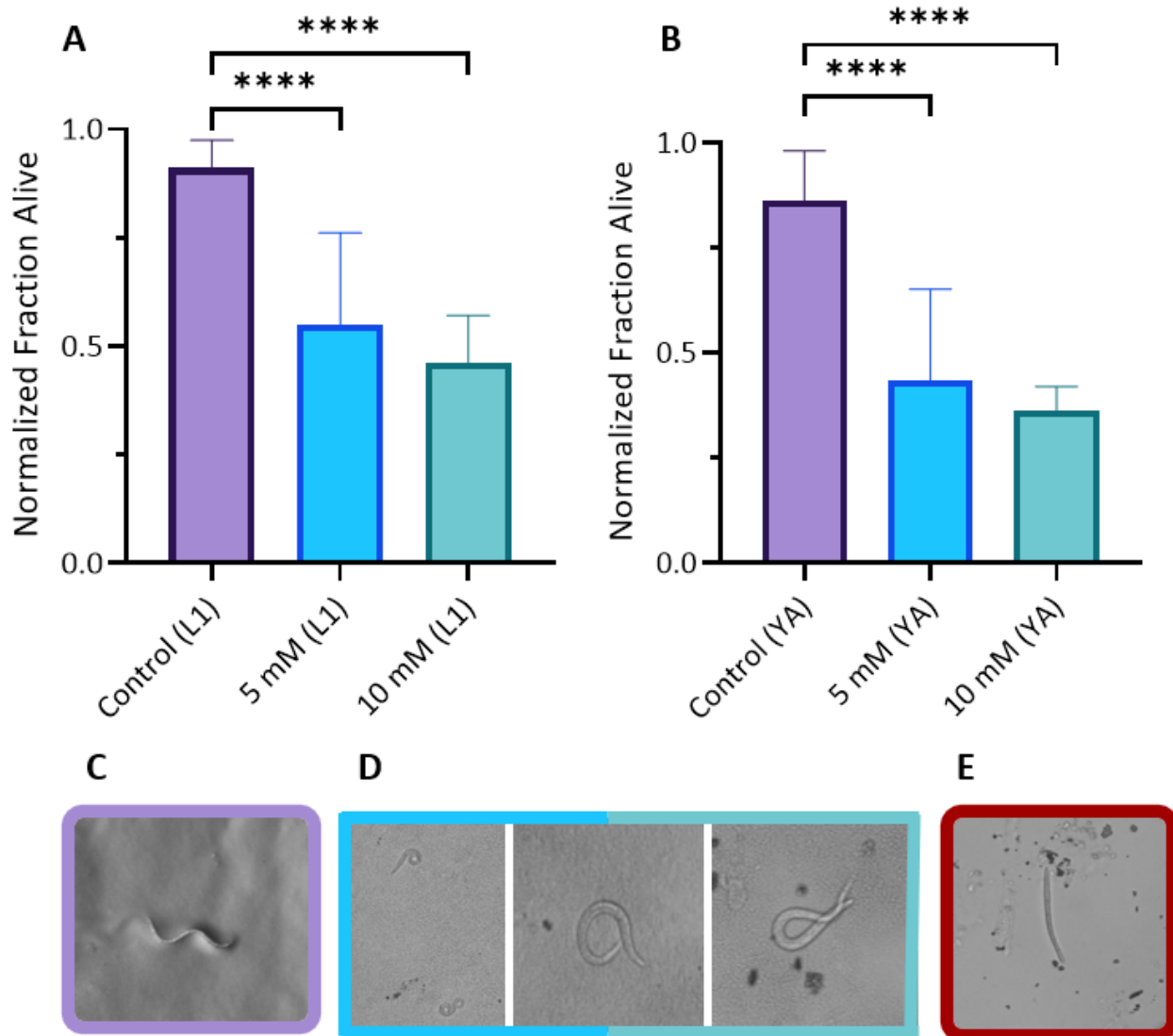


Figure 4-16 Quantitative analysis of L1 and YA control and exposed worms to 5 and 10 mM  $MnCl_2$ . A) Mortality rate of L1 worms for control (n=31) and exposed to 5 mM (n=160) and 10 mM (n=237) groups normalized using max scaling to the control group. B) Mortality rate of YA worms for control (n=21) and exposed to 5 mM (n=41) and 10 mM (n=83) groups normalized using max scaling to the control group. C) Representative image of a healthy *C. elegans*. D) Representative images of exposed worms. E) Representative image of a dead nematode.

While the 5mM exposed worms exhibited a significantly lower survival rate, those that survived did not demonstrate any significant change in their nerve ring expressions at L3, as illustrated in Figure 4-17A. Conversely, the 10mM exposed worms not only showed a higher mortality rate but also exhibited a significantly reduced fluorescence expression in their nerve rings. The Games-Howell's multiple comparisons test was applied to assess mean differences between the control group and two exposed groups (5mM and 10mM). Adjusted P values were 0.9982 for control vs. 5 mM and <0.0001 for control vs. 10 mM.

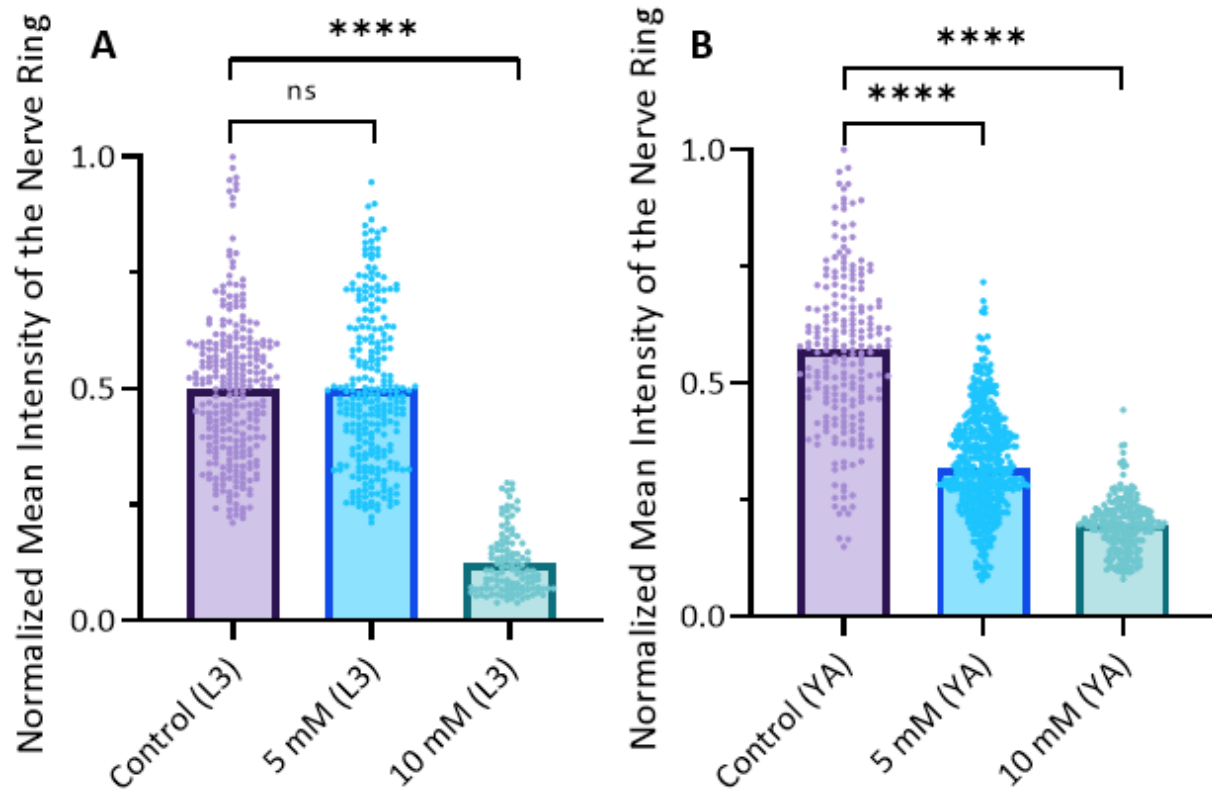


Figure 4-17 Quantitative analysis of the normalized mean intensity of the nerve rings for control and exposed groups at L3 and YA. A) Normalized mean intensity of the nerve rings for control (n=271), 5 mM (n=257) and 10 mM (n=115) exposed worms at L3. B) Normalized mean intensity of the nerve rings for control (n=215), 5 mM (n=460) and 10 mM (n=219) exposed worms at YA.

However, when we shifted our focus to the YA stage, a distinct pattern emerged. As the worms progressed in development to the YA stage, both the 5mM and 10mM exposed groups exhibited a proportional decrease in their survival rates. In contrast to the L3 stage, at the YA stage, the fluorescence expressions (Figure 4-17B) mirrored the observed survival rates (Figure 4-16B), showing a significant decrease with an increase in the exposure dosage. This divergence from the earlier stage suggests a potentially stage-specific impact of exposure on both survival and fluorescence expression in the worms. This decrease in MINR aligns with findings from prior studies, reinforcing the notion that environmental exposures or stressors may have a more pronounced impact on nutrient utilization and requirements in older developmental stages. These qualitative differences underscore the complexity of nutrient dynamics across the developmental timeline and highlight the potential susceptibility of certain life stages to external influences.

In the Games-Howell's multiple comparisons test conducted on a single family with two comparisons, assessing mean differences between the control group and two exposed groups (5

and 10), significant variations were observed. The comparison between control and 5 revealed a substantial mean difference of 0.2349, with a 95.00% confidence interval from 0.2051 to 0.2647. Similarly, the control versus 10 mM comparison showed a notable mean difference of 0.3688, with a confidence interval from 0.3401 to 0.3974. Both comparisons resulted in highly significant adjusted P values of <0.0001, denoted by '\*\*\*\*,' indicating a robust statistical difference. These findings suggest significant alterations in the measured parameters, emphasizing the impact of exposure, particularly in the 10 mM group, on the observed outcomes.

The observed pattern in the experiment suggests a dose-dependent impact of  $MnCl_2$  on the physiological responses of *C. elegans*. Firstly, increasing  $MnCl_2$  dosage correlates with a notable decrease in overall survival rates, indicating a toxic effect on the viability of the organism. Secondly, the differential sensitivity observed across developmental stages indicates a nuanced response, with the 5 mM dose not significantly affecting fluorescence expression at the L3 stage but showing a decrease in young adults. This implies a developmental stage-specific reaction to  $MnCl_2$  exposure. Thirdly, the presence of a threshold effect is suggested, as the 10 mM dose results in more pronounced adverse effects on both survival rates and neural health indicators, emphasizing the importance of precise dosage control in understanding the complex relationship between  $MnCl_2$  and *C. elegans* physiology.

## 5 Chapter Five: Thesis Summary and Future Work

This section summarizes the thesis, followed by recommendations for future research.

### 5.1 Thesis Summary

This study aimed to optimize an existing compact high-resolution device for monitoring and comparing control and exposed worms to toxicants. Modifications were made to accommodate roundworms at earlier stages (L3) in addition to YAs. Increasing the device's throughput to >20 worms per minute could produce reliable volumetric data of desired transgenic worms. After validating the platform's reliability and reproducibility, an automated neural assay was developed using MATLAB to quantify worms' neurons and protein aggregations for further analytical analysis.

The MATLAB code separated nerve rings by thresholding the highest intensity slices and identifying the maximum slices of each nerve ring stack. The desired region was then separated based on the FWHM of the signal and averaging the whole region intensity for an unbiased analysis of neural expression. The platform's feasibility was demonstrated by monitoring and analyzing each group of pan neural worms (NW1229) at the L3 and YA stages. Worms exposed to 500  $\mu$ M 6-OHDA, an established neurotoxicant, showed significant differences in both stages compared to control worms. Furthermore, imaging exposed worms to 5 and 10 mM *MnCl*<sub>2</sub> demonstrated the same trend, with an exception for 5 mM at L3. Overall, this study provides a reliable and automated platform for monitoring and comparing neurotoxicant exposure in worms.

This work has great potential to significantly contribute to drug discovery projects owing to its affordability, high throughput, and high resolution. By exposing the transgenic worms to neuroprotective compounds, their effects on the phenotypes can be studied for drug discovery purposes. Utilizing the transgenic PD model, our platform can be employed in the established neural assays to validate the potential compounds. The effect of different drug candidates can be detected and measured on the  $\alpha$ -Syn accumulation at the nerve ring where one of the phenotypes occurs. This enables researchers to study the dynamics of protein expression in populations of worms at different developmental stages and under various experimental conditions. Furthermore, the ability of this imaging system to accurately measure  $\alpha$ -Syn accumulation in *C. elegans* makes it a promising tool for studying the effect of different drugs in suppressing  $\alpha$ -Syn accumulation.

This could lead to the identification of potential therapeutic agents for PD and related disorders that involve  $\alpha$ -Syn accumulation.

## **5.2 Limitations and Recommendations for Future Work**

We successfully attained three objectives: enhancing throughput, extending technology to earlier development stages, and demonstrating diverse applications of the platform in monitoring chemical-induced neurodegeneration and protein accumulation. However, there are remaining limitations to address in future improvements, such as expanding coverage to all development stages, including the embryonic stage, L1, and L2. Another valuable feature for both gene and drug screening purposes would involve the capability to sort selected samples based on imaging output. Additionally, a beneficial enhancement would be the incorporation of multiple illumination lasers with varying wavelengths to enable imaging of multiple fluorescence reporters and seamless switching between them.

To pursue further investigations of neuroprotective drugs in PD model worms, it is necessary to establish a close collaboration with a biologist who possesses expertise in molecular docking. This collaboration is required to develop a high-throughput screening assay for neural and drug screening purposes.

Testing LOPAC1280, a collection of small compounds with recognized biological functions that may be utilized in exploring and advancing the creation of novel medications., is one strategy. The 1280 compounds in the library were chosen for the collection based on their availability, variety, and drug-like characteristics.

A variety of targets, including enzymes, receptors, ion channels, and transporters, have been discovered to be modulated by the chemicals in LOPAC1280, which have passed comprehensive testing for their biological action. These targets have been linked to several illnesses, including cancer, neurological disorders, and infectious diseases. They are involved in a wide range of cellular activities, including signal transduction, metabolism, and gene expression. The choice of a binding site on a target protein for drug development is influenced by several variables, such as the particular illness being targeted, the function of the target protein, and the intended mode of action of the medication.

On the other hand, choosing an appropriate binding site involves using structural data, such as protein crystal structures or computer simulations, to anticipate locations that are reachable and have the potential to bind drug-like compounds with high affinities, toxicity, etc. Cryo-electron microscopy (cryo-EM) analysis of the atomic structure of  $\alpha$ -Syn(1-121) fibrils has been published [107]. There are six family mutations in  $\alpha$ -Syn that have been linked to PD and other synucleinopathies (i.e., A30P, E46K, H50Q, G51D, A53E, and A53T). The fibril structure's core contains all of them, with the exception of A30P, making it possible to computationally simulate hypothetical compounds that may bind to those sites.

With the identification of compounds that are most likely to bind to recognized binding sites, computational modelling of prospective compounds can improve the hit rate. Molecular docking, molecular dynamics simulations, and virtual screening are examples of computational modelling approaches that may be used to predict and find compounds with high binding affinities to target proteins. The time and money needed for experimental validation can be greatly decreased by utilizing computational modelling to screen huge chemical libraries and exclude substances that are unlikely to bind to a target protein. It's possible that the expected interactions and binding affinities between a substance and a protein don't always correctly represent the binding behaviour in a biological system. Therefore, experimental validation is necessary to confirm the predicted binding affinities and assess the biological activity of the compounds.

As a starting point for future implementation, the low-cost and high-throughput light sheet platform may be utilized for hit compound validation from computational models or libraries of active compounds, such as LOPAC1280. Specifically, the five hit compounds Cyclosporin A, TBBz, PD173952, PD 169316, and PD-161570, which were validated through high-throughput assays of  $\alpha$ -Syn-PCA on LOPAC1280 by Moussaud *et al.*, can be used as a reference [108].

## 6 Bibliography

- [1] J. Apfeld and S. Alper, “What Can We Learn About Human Disease from the Nematode *C. elegans*?,” 2018, pp. 53–75. doi: 10.1007/978-1-4939-7471-9\_4.
- [2] T. K. Blackwell, M. J. Steinbaugh, J. M. Hourihan, C. Y. Ewald, and M. Isik, “SKN-1/Nrf, stress responses, and aging in *Caenorhabditis elegans*,” *Free Radic Biol Med*, vol. 88, pp. 290–301, Nov. 2015, doi: 10.1016/j.freeradbiomed.2015.06.008.
- [3] D. Teschendorf and C. D. Link, “What have worm models told us about the mechanisms of neuronal dysfunction in human neurodegenerative diseases?,” *Mol Neurodegener*, vol. 4, no. 1, p. 38, 2009, doi: 10.1186/1750-1326-4-38.
- [4] R. M. Power and J. Huisken, “A guide to light-sheet fluorescence microscopy for multiscale imaging,” *Nat Methods*, vol. 14, no. 4, pp. 360–373, Apr. 2017, doi: 10.1038/nmeth.4224.
- [5] R. McGorty, H. Liu, D. Kamiyama, Z. Dong, S. Guo, and B. Huang, “Open-top selective plane illumination microscope for conventionally mounted specimens,” *Opt Express*, vol. 23, no. 12, p. 16142, Jun. 2015, doi: 10.1364/oe.23.016142.
- [6] M. Rieckher *et al.*, “A Customized Light Sheet Microscope to Measure Spatio-Temporal Protein Dynamics in Small Model Organisms,” *PLoS One*, vol. 10, no. 5, p. e0127869, May 2015, doi: 10.1371/journal.pone.0127869.
- [7] Y. Wu *et al.*, “Inverted selective plane illumination microscopy (*i* SPIM) enables coupled cell identity lineaging and neurodevelopmental imaging in *Caenorhabditis elegans*,” *Proceedings of the National Academy of Sciences*, vol. 108, no. 43, pp. 17708–17713, Oct. 2011, doi: 10.1073/pnas.1108494108.
- [8] S. Rashtchian, K. Youssef, P. Rezai, and N. Tabatabaei, “High-speed label-free confocal microscopy of *Caenorhabditis elegans* with near infrared spectrally encoded confocal microscopy,” *Biomed Opt Express*, vol. 12, no. 6, p. 3607, Jun. 2021, doi: 10.1364/BOE.427685.

- [9] F. Zhao *et al.*, “Efficient and cost-effective 3D cellular imaging by sub-voxel-resolving light-sheet add-on microscopy,” *J Biophotonics*, vol. 13, no. 6, Jun. 2020, doi: 10.1002/jbio.201960243.
- [10] T.-Y. Hsieh, S. Vyas, J.-C. Wu, and Y. Luo, “Volume holographic optical element for light sheet fluorescence microscopy,” *Opt Lett*, vol. 45, no. 23, p. 6478, Dec. 2020, doi: 10.1364/OL.413204.
- [11] Z. Guan *et al.*, “Compact plane illumination plugin device to enable light sheet fluorescence imaging of multi-cellular organisms on an inverted wide-field microscope,” *Biomed Opt Express*, vol. 7, no. 1, p. 194, Jan. 2016, doi: 10.1364/boe.7.000194.
- [12] C. K. Rasmi *et al.*, “Integrated light-sheet imaging and flow-based enquiry (iLIFE) system for 3D *in-vivo* imaging of multicellular organism,” *Appl Phys Lett*, vol. 111, no. 24, p. 243702, Dec. 2017, doi: 10.1063/1.5009782.
- [13] M. Behrouzi, K. Youssef, P. Rezai, and N. Tabatabaei, “Low-cost optofluidic add-on enables rapid selective plane illumination microscopy of *C. elegans* with a conventional wide-field microscope,” *J Biomed Opt*, vol. 26, no. 12, Dec. 2021, doi: 10.1117/1.JBO.26.12.126501.
- [14] J. Lin, “Applications and Limitations of Genetically Modified Mouse Models in Drug Discovery and Development,” *Curr Drug Metab*, vol. 9, no. 5, pp. 419–438, Jun. 2008, doi: 10.2174/138920008784746355.
- [15] “The structure of the nervous system of the nematode *Caenorhabditis elegans*,” *Philosophical Transactions of the Royal Society of London. B, Biological Sciences*, vol. 314, no. 1165, pp. 1–340, Nov. 1986, doi: 10.1098/rstb.1986.0056.
- [16] Z. F. Altun and D. H. Hall, “WormAtlas Hermaphrodite Handbook - Introduction,” *WormAtlas*, Jun. 2006, doi: 10.3908/wormatlas.1.1.
- [17] R. Kerr, V. Lev-Ram, G. Baird, P. Vincent, R. Y. Tsien, and W. R. Schafer, “Optical Imaging of Calcium Transients in Neurons and Pharyngeal Muscle of *C. elegans*,” *Neuron*, vol. 26, no. 3, pp. 583–594, Jun. 2000, doi: 10.1016/S0896-6273(00)81196-4.

- [18] G. Nagel, M. Brauner, J. F. Liewald, N. Adeishvili, E. Bamberg, and A. Gottschalk, “Light Activation of Channelrhodopsin-2 in Excitable Cells of *Caenorhabditis elegans* Triggers Rapid Behavioral Responses,” *Current Biology*, vol. 15, no. 24, pp. 2279–2284, Dec. 2005, doi: 10.1016/j.cub.2005.11.032.
- [19] K. Strange, “Drug Discovery in Fish, Flies, and Worms,” *ILAR J*, vol. 57, no. 2, pp. 133–143, Dec. 2016, doi: 10.1093/ilar/ilw034.
- [20] M. Cornaglia, T. Lehnert, and M. A. M. Gijs, “Microfluidic systems for high-throughput and high-content screening using the nematode *Caenorhabditis elegans*,” *Lab Chip*, vol. 17, no. 22, pp. 3736–3759, 2017, doi: 10.1039/C7LC00509A.
- [21] A. R. Burns *et al.*, “*Caenorhabditis elegans* is a useful model for anthelmintic discovery,” *Nat Commun*, vol. 6, no. 1, p. 7485, Nov. 2015, doi: 10.1038/ncomms8485.
- [22] S. Maglioni, N. Arsalan, and N. Ventura, “*C. elegans* screening strategies to identify longevity interventions,” *Mech Ageing Dev*, vol. 157, pp. 60–69, Jul. 2016, doi: 10.1016/j.mad.2016.07.010.
- [23] M. Petrascheck, X. Ye, and L. B. Buck, “An antidepressant that extends lifespan in adult *Caenorhabditis elegans*,” *Nature*, vol. 450, no. 7169, pp. 553–556, Nov. 2007, doi: 10.1038/nature05991.
- [24] J.-A. Lepasant, “The promises of neurodegenerative disease modeling,” *C R Biol*, vol. 338, no. 8–9, pp. 584–592, Aug. 2015, doi: 10.1016/j.crv.2015.06.018.
- [25] X. Chen, J. W. Barclay, R. D. Burgoyne, and A. Morgan, “Using *C. elegans* to discover therapeutic compounds for ageing-associated neurodegenerative diseases,” *Chem Cent J*, vol. 9, no. 1, p. 65, Dec. 2015, doi: 10.1186/s13065-015-0143-y.
- [26] R. S. Kamath *et al.*, “Systematic functional analysis of the *Caenorhabditis elegans* genome using RNAi,” *Nature*, vol. 421, no. 6920, pp. 231–237, Jan. 2003, doi: 10.1038/nature01278.
- [27] T. R. Mhyre, J. T. Boyd, R. W. Hamill, and K. A. Maguire-Zeiss, “Parkinson’s Disease,” 2012, pp. 389–455. doi: 10.1007/978-94-007-5416-4\_16.

- [28] M. Gómez-Benito, N. Granado, P. García-Sanz, A. Michel, M. Dumoulin, and R. Moratalla, “Modeling Parkinson’s Disease With the Alpha-Synuclein Protein,” *Front Pharmacol*, vol. 11, Apr. 2020, doi: 10.3389/fphar.2020.00356.
- [29] M. Lakso *et al.*, “Dopaminergic neuronal loss and motor deficits in *Caenorhabditis elegans* overexpressing human  $\alpha$ -synuclein,” *J Neurochem*, vol. 86, no. 1, pp. 165–172, Feb. 2004, doi: 10.1046/j.1471-4159.2003.01809.x.
- [30] T. J. van Ham, K. L. Thijssen, R. Breitling, R. M. W. Hofstra, R. H. A. Plasterk, and E. A. A. Nollen, “*C. elegans* Model Identifies Genetic Modifiers of  $\alpha$ -Synuclein Inclusion Formation During Aging,” *PLoS Genet*, vol. 4, no. 3, p. e1000027, Mar. 2008, doi: 10.1371/journal.pgen.1000027.
- [31] R. Vozdek, P. P. Pramstaller, and A. A. Hicks, “Functional Screening of Parkinson’s Disease Susceptibility Genes to Identify Novel Modulators of  $\alpha$ -Synuclein Neurotoxicity in *Caenorhabditis elegans*,” *Front Aging Neurosci*, vol. 14, Apr. 2022, doi: 10.3389/fnagi.2022.806000.
- [32] S. Sohrabi, D. E. Mor, R. Kaletsky, W. Keyes, and C. T. Murphy, “High-throughput behavioral screen in *C. elegans* reveals Parkinson’s disease drug candidates,” *Commun Biol*, vol. 4, no. 1, p. 203, Dec. 2021, doi: 10.1038/s42003-021-01731-z.
- [33] M. Marvanova and C. D. Nichols, “Identification of neuroprotective compounds of *Caenorhabditis elegans* dopaminergic neurons against 6-OHDA,” *Journal of Molecular Neuroscience*, vol. 31, no. 2, pp. 127–137, Jun. 2007, doi: 10.1385/JMN/31:02:127.
- [34] R. Ved *et al.*, “Similar Patterns of Mitochondrial Vulnerability and Rescue Induced by Genetic Modification of  $\alpha$ -Synuclein, Parkin, and DJ-1 in *Caenorhabditis elegans*,” *Journal of Biological Chemistry*, vol. 280, no. 52, pp. 42655–42668, Dec. 2005, doi: 10.1074/jbc.M505910200.
- [35] E. Braungart, M. Gerlach, P. Riederer, R. Baumeister, and M. C. Hoener, “&lt;i&gt;Caenorhabditis elegans&lt;/i&gt; MPP&lt;sup&gt;+&lt;/sup&gt; Model of Parkinson’s Disease for High-Throughput Drug Screenings,” *Neurodegener Dis*, vol. 1, no. 4–5, pp. 175–183, 2004, doi: 10.1159/000080983.

- [36] R. J. Shmookler Reis, P. Bharill, C. Tazearslan, and S. Ayyadevara, “Extreme-longevity mutations orchestrate silencing of multiple signaling pathways,” *Biochimica et Biophysica Acta (BBA) - General Subjects*, vol. 1790, no. 10, pp. 1075–1083, Oct. 2009, doi: 10.1016/j.bbagen.2009.05.011.
- [37] F. R. G. Amrit, R. Ratnappan, S. A. Keith, and A. Ghazi, “The *C. elegans* lifespan assay toolkit,” *Methods*, vol. 68, no. 3, pp. 465–475, Aug. 2014, doi: 10.1016/j.ymeth.2014.04.002.
- [38] H.-E. H. Park, Y. Jung, and S.-J. V. Lee, “Survival assays using *Caenorhabditis elegans*,” *Mol Cells*, vol. 40, no. 2, pp. 90–99, Feb. 2017, doi: 10.14348/molcells.2017.0017.
- [39] S. E. Hulme, S. S. Shevkopyas, A. P. McGuigan, J. Apfeld, W. Fontana, and G. M. Whitesides, “Lifespan-on-a-chip: microfluidic chambers for performing lifelong observation of *C. elegans*,” *Lab Chip*, vol. 10, no. 5, pp. 589–597, 2010, doi: 10.1039/B919265D.
- [40] N. Kim, C. M. Dempsey, J. V. Zoval, J.-Y. Sze, and M. J. Madou, “Automated microfluidic compact disc (CD) cultivation system of *Caenorhabditis elegans*,” *Sens Actuators B Chem*, vol. 122, no. 2, pp. 511–518, Mar. 2007, doi: 10.1016/j.snb.2006.06.026.
- [41] N. Chronis, M. Zimmer, and C. I. Bargmann, “Microfluidics for in vivo imaging of neuronal and behavioral activity in *Caenorhabditis elegans*,” *Nat Methods*, vol. 4, no. 9, pp. 727–731, Sep. 2007, doi: 10.1038/nmeth1075.
- [42] K. Chung *et al.*, “Microfluidic chamber arrays for whole-organism behavior-based chemical screening,” *Lab Chip*, vol. 11, no. 21, p. 3689, 2011, doi: 10.1039/c1lc20400a.
- [43] M. B. Goodman and P. Sengupta, “How *Caenorhabditis elegans* Senses Mechanical Stress, Temperature, and Other Physical Stimuli,” *Genetics*, vol. 212, no. 1, pp. 25–51, May 2019, doi: 10.1534/genetics.118.300241.
- [44] L. Dong, M. Cornaglia, T. Lehnert, and M. A. M. Gijs, “Versatile size-dependent sorting of *C. elegans* nematodes and embryos using a tunable microfluidic filter structure,” *Lab Chip*, vol. 16, no. 3, pp. 574–585, 2016, doi: 10.1039/C5LC01328C.

- [45] A. Ben-Yakar, “High-Content and High-Throughput *In Vivo* Drug Screening Platforms Using Microfluidics,” *Assay Drug Dev Technol*, vol. 17, no. 1, pp. 8–13, Jan. 2019, doi: 10.1089/adt.2018.908.
- [46] H. Schneckenburger and V. Richter, “Laser scanning versus wide-field—choosing the appropriate microscope in life sciences,” *Applied Sciences (Switzerland)*, vol. 11, no. 2. MDPI AG, pp. 1–17, Jan. 02, 2021. doi: 10.3390/app11020733.
- [47] C.-W. Tsai *et al.*, “Neuroprotective Effects of Betulin in Pharmacological and Transgenic *Caenorhabditis elegans* Models of Parkinson’s Disease,” *Cell Transplant*, vol. 26, no. 12, pp. 1903–1918, Dec. 2017, doi: 10.1177/0963689717738785.
- [48] G. Aubry and H. Lu, “A perspective on optical developments in microfluidic platforms for *Caenorhabditis elegans* research,” *Biomicrofluidics*, vol. 8, no. 1, p. 011301, Jan. 2014, doi: 10.1063/1.4865167.
- [49] L. Breimann, F. Preusser, and S. Preibisch, “Light-microscopy methods in *C. elegans* research,” *Curr Opin Syst Biol*, vol. 13, pp. 82–92, Feb. 2019, doi: 10.1016/j.coisb.2018.11.004.
- [50] J. Huisken, J. Swoger, F. Del Bene, J. Wittbrodt, and E. H. K. Stelzer, “Optical Sectioning Deep Inside Live Embryos by Selective Plane Illumination Microscopy,” *Science (1979)*, vol. 305, no. 5686, pp. 1007–1009, Aug. 2004, doi: 10.1126/science.1100035.
- [51] B.-C. Chen *et al.*, “Lattice light-sheet microscopy: Imaging molecules to embryos at high spatiotemporal resolution,” *Science (1979)*, vol. 346, no. 6208, Oct. 2014, doi: 10.1126/science.1257998.
- [52] J. Huisken and D. Y. R. Stainier, “Even fluorescence excitation by multidirectional selective plane illumination microscopy (mSPIM),” *Opt Lett*, vol. 32, no. 17, p. 2608, Sep. 2007, doi: 10.1364/OL.32.002608.
- [53] P. J. Keller, A. D. Schmidt, J. Wittbrodt, and E. H. K. Stelzer, “Reconstruction of Zebrafish Early Embryonic Development by Scanned Light Sheet Microscopy,” *Science (1979)*, vol. 322, no. 5904, pp. 1065–1069, Nov. 2008, doi: 10.1126/science.1162493.

- [54] O. E. Olarte, J. Andilla, E. J. Gualda, and P. Loza-Alvarez, “Light-sheet microscopy: a tutorial,” *Adv Opt Photonics*, vol. 10, no. 1, p. 111, Mar. 2018, doi: 10.1364/aop.10.000111.
- [55] “ZEISS Lattice Lightsheet 7.” Accessed: May 18, 2023. [Online]. Available: <https://www.zeiss.com/microscopy/en/products/light-microscopes/light-sheet-microscopes/lattice-lightsheet-7.html>
- [56] K. Greger, J. Swoger, and E. H. K. Stelzer, “Basic building units and properties of a fluorescence single plane illumination microscope,” *Review of Scientific Instruments*, vol. 78, no. 2, p. 023705, Feb. 2007, doi: 10.1063/1.2428277.
- [57] M. Weber, M. Mickoleit, and J. Huiskens, “Light sheet microscopy,” 2014, pp. 193–215. doi: 10.1016/B978-0-12-420138-5.00011-2.
- [58] P. G. Pitrone *et al.*, “OpenSPIM: an open-access light-sheet microscopy platform,” *Nat Methods*, vol. 10, no. 7, pp. 598–599, Jul. 2013, doi: 10.1038/nmeth.2507.
- [59] E. J. Gualda, T. Vale, P. Almada, J. A. Feijó, G. G. Martins, and N. Moreno, “OpenSpinMicroscopy: an open-source integrated microscopy platform,” *Nat Methods*, vol. 10, no. 7, pp. 599–600, Jul. 2013, doi: 10.1038/nmeth.2508.
- [60] E. G. Reynaud, J. Peychl, J. Huiskens, and P. Tomancak, “Guide to light-sheet microscopy for adventurous biologists,” *Nat Methods*, vol. 12, no. 1, pp. 30–34, Jan. 2015, doi: 10.1038/nmeth.3222.
- [61] J. Huiskens, J. Swoger, F. del Bene, J. Wittbrodt, and E. H. K. Stelzer, “Optical Sectioning Deep Inside Live Embryos by Selective Plane Illumination Microscopy,” *Science (1979)*, vol. 305, no. 5686, pp. 1007–1009, Aug. 2004, doi: 10.1126/science.1100035.
- [62] U. Krzic, S. Gunther, T. E. Saunders, S. J. Streichan, and L. Hufnagel, “Multiview light-sheet microscope for rapid in toto imaging,” *Nat Methods*, vol. 9, no. 7, pp. 730–733, Jul. 2012, doi: 10.1038/nmeth.2064.
- [63] H.-U. Dodt *et al.*, “Ultramicroscopy: three-dimensional visualization of neuronal networks in the whole mouse brain,” *Nat Methods*, vol. 4, no. 4, pp. 331–336, Apr. 2007, doi: 10.1038/nmeth1036.

- [64] M. Silhankova and H. C. Korswagen, “Migration of neuronal cells along the anterior–posterior body axis of *C. elegans*: Wnts are in control,” *Curr Opin Genet Dev*, vol. 17, no. 4, pp. 320–325, Aug. 2007, doi: 10.1016/j.gde.2007.05.007.
- [65] Y. Wu *et al.*, “Spatially isotropic four-dimensional imaging with dual-view plane illumination microscopy,” *Nat Biotechnol*, vol. 31, no. 11, pp. 1032–1038, Nov. 2013, doi: 10.1038/nbt.2713.
- [66] L. Gao, “Extend the field of view of selective plan illumination microscopy by tiling the excitation light sheet,” *Opt Express*, vol. 23, no. 5, p. 6102, Mar. 2015, doi: 10.1364/OE.23.006102.
- [67] J. van Krugten, K. K. H. Taris, and E. J. G. Peterman, “Imaging adult *C. elegans* live using light-sheet microscopy,” *J Microsc*, vol. 281, no. 3, pp. 214–223, Mar. 2021, doi: 10.1111/jmi.12964.
- [68] I. Albert-Smet, A. Marcos-Vidal, J. J. Vaquero, M. Desco, A. Muñoz-Barrutia, and J. Ripoll, “Applications of Light-Sheet Microscopy in Microdevices,” *Front Neuroanat*, vol. 13, Jan. 2019, doi: 10.3389/fnana.2019.00001.
- [69] Y. Cho, C. L. Zhao, and H. Lu, “Trends in high-throughput and functional neuroimaging in *Caenorhabditis elegans*,” *WIREs Systems Biology and Medicine*, vol. 9, no. 3, May 2017, doi: 10.1002/wsbm.1376.
- [70] C. Martin, T. Li, E. Hegarty, P. Zhao, S. Mondal, and A. Ben-Yakar, “Line excitation array detection fluorescence microscopy at 0.8 million frames per second,” *Nat Commun*, vol. 9, no. 1, p. 4499, Oct. 2018, doi: 10.1038/s41467-018-06775-0.
- [71] S. Mondal *et al.*, “High-Content Microfluidic Screening Platform Used To Identify  $\sigma 2R/Tmem97$  Binding Ligands that Reduce Age-Dependent Neurodegeneration in *C. elegans* SC\_APP Model,” *ACS Chem Neurosci*, vol. 9, no. 5, pp. 1014–1026, May 2018, doi: 10.1021/acchemneuro.7b00428.
- [72] S. Mondal, E. Hegarty, C. Martin, S. K. Gökçe, N. Ghorashian, and A. Ben-Yakar, “Large-scale microfluidics providing high-resolution and high-throughput screening of

- Caenorhabditis elegans poly-glutamine aggregation model,” *Nat Commun*, vol. 7, no. 1, p. 13023, Oct. 2016, doi: 10.1038/ncomms13023.
- [73] “Mehran” “Behrouzi,” “OPTOFLUIDIC ADD-ON DEVICES FOR LIGHT-SHEET FLUORESCENCE MICROSCOPY OF CAENORHABDITIS ELEGANS WITH CONVENTIONAL WIDE-FIELD MICROSCOPES,” Masters, York University, Toronto, 2022.
- [74] C.-H. Chen, Y.-C. Chen, H.-C. Jiang, C.-K. Chen, and C.-L. Pan, “Neuronal aging: learning from <em>C. elegans</em>,” *J Mol Signal*, vol. 8, p. 14, Dec. 2013, doi: 10.1186/1750-2187-8-14.
- [75] T. Stiernagle, “Maintenance of *C. elegans*,” *WormBook*, 2006, doi: 10.1895/wormbook.1.101.1.
- [76] M. Porta-de-la-Riva, L. Fontrodona, A. Villanueva, and J. Cerón, “Basic <em>Caenorhabditis elegans</em> Methods: Synchronization and Observation,” *Journal of Visualized Experiments*, no. 64, Jun. 2012, doi: 10.3791/4019.
- [77] J. Schindelin *et al.*, “Fiji: an open-source platform for biological-image analysis,” *Nat Methods*, vol. 9, no. 7, pp. 676–682, Jul. 2012, doi: 10.1038/nmeth.2019.
- [78] J. Sulston, M. Dew, and S. Brenner, “Dopaminergic neurons in the nematode *Caenorhabditis elegans*,” *J Comp Neurol*, vol. 163, no. 2, pp. 215–226, Sep. 1975, doi: 10.1002/cne.901630207.
- [79] “The structure of the nervous system of the nematode *Caenorhabditis elegans*,” *Philosophical Transactions of the Royal Society of London. B, Biological Sciences*, vol. 314, no. 1165, pp. 1–340, Nov. 1986, doi: 10.1098/rstb.1986.0056.
- [80] Z. Altun, “WormAtlas Embryo Handbook - Nervous System in the Embryo - Nerve Ring Development,” *WormAtlas*, Oct. 2017, doi: 10.3908/wormatlas.4.2.
- [81] L. Stefanis, “-Synuclein in Parkinson’s Disease,” *Cold Spring Harb Perspect Med*, vol. 2, no. 2, pp. a009399–a009399, Feb. 2012, doi: 10.1101/cshperspect.a009399.

- [82] N. van den Berge *et al.*, “Ageing promotes pathological alpha-synuclein propagation and autonomic dysfunction in wild-type rats,” *Brain*, vol. 144, no. 6, pp. 1853–1868, Jul. 2021, doi: 10.1093/brain/awab061.
- [83] T. Tyson, M. Senchuk, J. F. Cooper, S. George, J. M. van Raamsdonk, and P. Brundin, “Novel animal model defines genetic contributions for neuron-to-neuron transfer of  $\alpha$ -synuclein,” *Sci Rep*, vol. 7, no. 1, p. 7506, Aug. 2017, doi: 10.1038/s41598-017-07383-6.
- [84] P. H. Mitchell, K. Bull, S. Glautier, N. A. Hopper, L. Holden-Dye, and V. O’Connor, “The concentration-dependent effects of ethanol on *Caenorhabditis elegans* behaviour,” *Pharmacogenomics J*, vol. 7, no. 6, pp. 411–417, Dec. 2007, doi: 10.1038/sj.tpj.6500440.
- [85] O. Margie, C. Palmer, and I. Chin-Sang, “&lt;em&gt;C. elegans&lt;/em&gt; Chemotaxis Assay,” *Journal of Visualized Experiments*, no. 74, Apr. 2013, doi: 10.3791/50069.
- [86] M. Di Rocco *et al.*, “*Caenorhabditis elegans* provides an efficient drug screening platform for *GNAO1* -related disorders and highlights the potential role of caffeine in controlling dyskinesia,” *Hum Mol Genet*, vol. 31, no. 6, pp. 929–941, Mar. 2022, doi: 10.1093/hmg/ddab296.
- [87] C. K. Leung *et al.*, “An Ultra High-Throughput, Whole-Animal Screen for Small Molecule Modulators of a Specific Genetic Pathway in *Caenorhabditis elegans*,” *PLoS One*, vol. 8, no. 4, p. e62166, Apr. 2013, doi: 10.1371/journal.pone.0062166.
- [88] S. J. Gosai *et al.*, “Automated High-Content Live Animal Drug Screening Using *C. elegans* Expressing the Aggregation Prone Serpin  $\alpha 1$ -antitrypsin Z,” *PLoS One*, vol. 5, no. 11, p. e15460, Nov. 2010, doi: 10.1371/journal.pone.0015460.
- [89] X. Ye, J. M. Linton, N. J. Schork, L. B. Buck, and M. Petrascheck, “A pharmacological network for lifespan extension in *C. aenorhabditis elegans*,” *Aging Cell*, vol. 13, no. 2, pp. 206–215, Apr. 2014, doi: 10.1111/accel.12163.
- [90] R. Nass, D. H. Hall, D. M. Miller III, and R. D. Blakely, “Neurotoxin-induced degeneration of dopamine neurons in *Caenorhabditis elegans*,” 2001. [Online]. Available: [www.pnas.org](http://www.pnas.org)

- [91] S.-L. Offenburger, X. Y. Ho, T. Tachie-Menson, S. Coakley, M. A. Hilliard, and A. Gartner, “6-OHDA-induced dopaminergic neurodegeneration in *Caenorhabditis elegans* is promoted by the engulfment pathway and inhibited by the transthyretin-related protein TTR-33,” *PLoS Genet*, vol. 14, no. 1, p. e1007125, Jan. 2018, doi: 10.1371/journal.pgen.1007125.
- [92] S.-L. Offenburger and A. Gartner, “6-hydroxydopamine (6-OHDA) Oxidative Stress Assay for Observing Dopaminergic Neuron Loss in *Caenorhabditis elegans*,” *Bio Protoc*, vol. 8, no. 18, 2018, doi: 10.21769/BioProtoc.3025.
- [93] J. E. Post, “Manganese oxide minerals: Crystal structures and economic and environmental significance,” *Proceedings of the National Academy of Sciences*, vol. 96, no. 7, pp. 3447–3454, Mar. 1999, doi: 10.1073/pnas.96.7.3447.
- [94] A. Takeda, N. Sotogaku, and N. Oku, “Influence of manganese on the release of neurotransmitters in rat striatum,” *Brain Res*, vol. 965, no. 1–2, pp. 279–282, Mar. 2003, doi: 10.1016/S0006-8993(02)04157-4.
- [95] D. L. Baly, C. L. Keen, and L. S. Hurley, “Pyruvate Carboxylase and Phosphoenolpyruvate Carboxykinase Activity in Developing Rats: Effect of Manganese Deficiency,” *J Nutr*, vol. 115, no. 7, pp. 872–879, Jul. 1985, doi: 10.1093/jn/115.7.872.
- [96] C. J. Brock and J. E. Walker, “Superoxide dismutase from *Bacillus stearothermophilus*. Complete amino acid sequence of a manganese enzyme,” *Biochemistry*, vol. 19, no. 13, pp. 2873–2882, Jun. 1980, doi: 10.1021/bi00554a009.
- [97] Y. Takeda and H. Avila, “Structure and gene expression of the *E. coli* Mn-superoxide dismutase gene,” *Nucleic Acids Res*, vol. 14, no. 11, pp. 4577–4589, 1986, doi: 10.1093/nar/14.11.4577.
- [98] F. C. WEDLER and R. B. DENMAN, “Glutamine Synthetase: The Major Mn(II) Enzyme in Mammalian Brain,” 1984, pp. 153–154. doi: 10.1016/B978-0-12-152824-9.50021-6.
- [99] C. Au, A. Benedetto, and M. Aschner, “Manganese transport in eukaryotes: The role of DMT1,” *Neurotoxicology*, vol. 29, no. 4, pp. 569–576, Jul. 2008, doi: 10.1016/j.neuro.2008.04.022.

- [100] M. Aschner and J. L. Aschner, "Manganese neurotoxicity: Cellular effects and blood-brain barrier transport," *Neurosci Biobehav Rev*, vol. 15, no. 3, pp. 333–340, Sep. 1991, doi: 10.1016/S0149-7634(05)80026-0.
- [101] K. Thompson, R. M. Molina, T. Donaghey, J. E. Schwob, J. D. Brain, and M. Wessling-Resnick, "Olfactory uptake of manganese requires DMT1 and is enhanced by anemia," *The FASEB Journal*, vol. 21, no. 1, pp. 223–230, Jan. 2007, doi: 10.1096/fj.06-6710com.
- [102] D. C. Dorman, B. E. McManus, C. U. Parkinson, C. A. Manuel, A. M. McElveen, and J. I. Everitt, "Nasal Toxicity of Manganese Sulfate and Manganese Phosphate in Young Male Rats Following Subchronic (13-Week) Inhalation Exposure," *Inhal Toxicol*, vol. 16, no. 6–7, pp. 481–488, Jan. 2004, doi: 10.1080/08958370490439687.
- [103] G. A. Wasserman *et al.*, "Water Manganese Exposure and Children's Intellectual Function in Araihasar, Bangladesh," *Environ Health Perspect*, vol. 114, no. 1, pp. 124–129, Jan. 2006, doi: 10.1289/ehp.8030.
- [104] J. E. Myers *et al.*, "Nervous System Effects of Occupational Manganese Exposure on South African Manganese Mineworkers," *Neurotoxicology*, vol. 24, no. 4–5, pp. 649–656, Aug. 2003, doi: 10.1016/S0161-813X(03)00035-4.
- [105] P. K. Pal, A. Samii, and D. B. Calne, "Manganese neurotoxicity: a review of clinical features, imaging and pathology.," *Neurotoxicology*, vol. 20, no. 2–3, pp. 227–38, 1999.
- [106] H. B. Ferraz, P. H. F. Bertolucci, J. S. Pereira, J. G. C. Lima, and L. A. F. Andrade, "Chronic exposure to the fungicide maneb may produce symptoms and signs of CNS manganese intoxication," *Neurology*, vol. 38, no. 4, pp. 550–550, Apr. 1988, doi: 10.1212/WNL.38.4.550.
- [107] R. Guerrero-Ferreira *et al.*, "Cryo-EM structure of alpha-synuclein fibrils," *Elife*, vol. 7, Jul. 2018, doi: 10.7554/eLife.36402.
- [108] S. Moussaud, S. Malany, A. Mehta, S. Vasile, L. H. Smith, and P. J. McLean, "Targeting  $\alpha$ -synuclein oligomers by protein-fragment complementation for drug discovery in synucleinopathies," *Expert Opin Ther Targets*, vol. 19, no. 5, pp. 589–603, May 2015, doi: 10.1517/14728222.2015.1009448.



